

Nuclear Reactions with ^{11}C and ^{14}O Radioactive Ion Beams

by

Fanqing Guo

B.S. (Fudan University) 1991
M.S. (Chinese Academy of Sciences) 1994

A dissertation submitted in partial satisfaction of the

requirements for the degree of

Doctor of Philosophy

in

Chemistry

in the

GRADUATE DIVISION

of the

UNIVERSITY OF CALIFORNIA, BERKELEY

Committee in charge:

Professor Joseph Cerny, Chair
Professor Heino Nitsche
Professor Stanley G. Prussin

Fall 2004

DISCLAIMER

This document was prepared as an account of work sponsored by the United States Government. While this document is believed to contain correct information, neither the United States Government nor any agency thereof, nor The Regents of the University of California, nor any of their employees, makes any warranty, express or implied, or assumes any legal responsibility for the accuracy, completeness, or usefulness of any information, apparatus, product, or process disclosed, or represents that its use would not infringe privately owned rights. Reference herein to any specific commercial product, process, or service by its trade name, trademark, manufacturer, or otherwise, does not necessarily constitute or imply its endorsement, recommendation, or favoring by the United States Government or any agency thereof, or The Regents of the University of California. The views and opinions of authors expressed herein do not necessarily state or reflect those of the United States Government or any agency thereof or The Regents of the University of California.

The dissertation of Fanqing Guo is approved:

Chair

Date

Date

Date

University of California, Berkeley

Fall 2004

Nuclear Reactions with ^{11}C and ^{14}O Radioactive Ion Beams

Copyright 2004

by

Fanqing Guo

ABSTRACT

Nuclear Reactions with ^{11}C and ^{14}O Radioactive Ion Beams

by

Fanqing Guo

Doctor of Philosophy in Chemistry

University of California, Berkeley

Professor Joseph Cerny, Chair

Radioactive ion beams (RIBs) have been shown to be a useful tool for studying proton-rich nuclides near and beyond the proton dripline and for evaluating nuclear models. To take full advantage of RIBs, Elastic Resonance Scattering in Inverse Kinematics with Thick Targets (ERSIKTT), has proven to be a reliable experimental tool for investigations of proton unbound nuclei.

Following several years of effort, Berkeley Experiments with Accelerated Radioactive Species (BEARS), a RIBs capability, has been developed at the Lawrence Berkeley National Laboratory's 88-Inch Cyclotron. The current BEARS provides two RIBs: a ^{11}C beam of up to 2×10^8 pps intensity on target and an ^{14}O beam of up to 3×10^4 pps intensity. While the development of the ^{11}C beam has been relatively easy, a number of challenges had to be overcome to obtain the ^{14}O beam.

The excellent ^{11}C beam has been used to investigate several reactions. The first was the $^{197}\text{Au}(^{11}\text{C},\text{xn})^{208-\text{xn}}\text{At}$ reaction, which was used to measure excitation functions for the $4n$ to $8n$ exit channels. The measured cross sections were generally predicted quite well using the fusion-evaporation code HIVAP. Possible errors in the branching ratios of α decays from At isotopes as well as the presence of incomplete fusion reactions probably contribute to specific overpredictions.

^{15}F has been investigated by the $\text{p}(^{14}\text{O},\text{p})^{14}\text{O}$ reaction with the ERSIKTT technology. Several $^{14}\text{O}+\text{p}$ runs have been performed. Excellent energy calibration was obtained using resonances from the $\text{p}(^{14}\text{N},\text{p})^{14}\text{N}$ reaction in inverse kinematics, and comparing the results to those obtained earlier with normal kinematics. The differences between $^{14}\text{N}+\text{p}$ and $^{14}\text{O}+\text{p}$ in the stopping power function have been evaluated for better energy calibration. After careful calibration, the energy levels of ^{15}F were fitted with an R-matrix calculation. Spins and parities were assigned to the two observed resonances. This new measurement of the ^{15}F ground state supports the disappearance of the $Z = 8$ proton magic number for odd Z , $T_z=-3/2$ nuclei.

It is expected that future work on proton-rich nuclides will rely heavily on RIBs and/or mass separators. Currently, radioactive ion beam intensities are sufficient for the study of a reasonable number of very proton-rich nuclides.

To my mother Jiaying, father Qixiao, wife Birong, and daughter YaYa

Table of Contents

LIST OF FIGURES.....	vi
LIST OF TABLES	ix
ACKNOWLEDGMENTS	xi
1 INTRODUCTION.....	1
1.1 Toward and Beyond the Proton Dripline	
with Radioactive Ion Beams	1
1.2 Thesis Organization.....	5
2 RADIOACTIVE ION BEAMS	9
2.1 Introduction.....	9
2.2 Methods of Producing Radioactive Ion Beams	12
2.3 Opportunities with Radioactive Ion Beams	18
2.4 Summary	21
3 EXPERIMENTAL EQUIPMENT AND TECHNIQUES.....	22
3.1 Preparation of Nuclides	22
3.1.1 The 88-Inch Cyclotron	22
3.1.2 Production Reactions for Proton-Rich Nuclides.....	25

3.2	Elastic Resonance Scattering Reactions in Inverse Kinematics with Thick Targets	27
3.2.1	Inverse Kinematics	28
3.2.2	Thick Target	32
3.2.3	Energy Resolution	34
3.2.4	Inelastic Scattering Competing Reactions	36
3.2.5	Cross section.....	38
3.2.6	Applicability of ERSIKTT to Radioactive Ion Beams.....	38
3.3	Radiation Detection	39
3.3.1	Radiation Detectors.....	39
3.3.2	Particle-Identification Telescopes.....	40
3.3.3	Counting Electronics	42
3.4	Data Analysis.....	44
3.4.1	Data Reduction in Software.....	44
3.4.2	Calibration of Detector Systems	46

4 BEARS: PRODUCTION OF RADIOACTIVE		
ION BEAMS OF ^{11}C AND ^{14}O	48	
4.1	Introduction.....	48
4.2	Test Experiments.....	50
4.2.1	Tests with Mimicking BIF at the 88-Inch Cyclotron.....	50
4.2.2	Batch Mode Coupling of BIF to the 88-Inch Cyclotron.....	55
4.2.3	Transfer-Line Mode for Coupling BIF to the 88-Inch Cyclotron	57

4.3	Final BEARS Configuration	58
4.3.1	Target system at BIF	58
4.3.2	Transport.....	60
4.3.3	Cryogenic system.....	62
4.3.4	Ion Source injection.....	63
4.3.5	Ionization and Acceleration	65
4.4	Production of a Radioactive ^{14}O Ion Beam	66
4.4.1	^{14}O Chemistry in BIF	66
4.4.2	Ionization and Acceleration of ^{14}O	68

5 USING RADIOACTIVE ^{11}C ION BEAMS TO MEASURE EXCITATION		
FUNCTIONS IN THE REACTIONS $^{197}\text{Au}(^{11}\text{C},xn)^{208-x}\text{At}$	71	
5.1	Introduction.....	71
5.2	Experiment	73
5.3	Results and Discussion	79
5.3.1	α -spectra	79
5.3.2	$^{197}\text{Au}(^{12}\text{C},xn)^{209-x}\text{At}$	81
5.3.3	$^{197}\text{Au}(^{11}\text{C},xn)^{208-x}\text{At}$	85
5.3.4	Comparisons of $^{197}\text{Au}(^{11}\text{C},xn)^{208-x}\text{At}$ with $^{197}\text{Au}(^{12}\text{C},xn)^{209-x}\text{At}$	87
5.4	Conclusion	89

6 ENERGY LEVELS OF ^{15}F.....	90	
6.1	Introduction.....	90

6.2	Experiment	93
6.3	Results and Discussion	97
6.3.1	R-matrix formalism	97
6.3.2	Results	100
6.4	Discussion	105
6.4.1	Comparison	105
6.4.2	Isobaric Multiplet Mass Equation of $T=3/2$, $A=15$	107
6.4.3	Thomas-Ehrman Shift	109
6.4.4	Disappearance of the Magic Number Effect	111
6.5	Summary	113
7 SUMMARY AND FUTURE WORK		114
7.1	Summary	114
7.2	Outlook	116
8 REFERENCES		120

LIST OF FIGURES

1-1: Nuclear landscape showing the known nuclei and terra incognita	1
2-1: Schematic representations of the two basic types of radioactive ion beam facilities.....	13
2-2: A hybrid PF based ISOL RIB system	15
2-3: Illustration of research opportunities with high intensity radioactive ion beams.....	19
3-1: The 88-Inch Cyclotron Facility	23
3-2: Cave 4A beamline and the scattering chamber.....	24
3-3: Spectrum of α particles produced from the interaction of 45 MeV ^{15}N with a thick ^4He target at 0° ($\theta_{\text{c.m.}}=180^\circ$)	29
3-4: Energy straggling of 90 MeV ^{14}O beams in polyethylene targets	33
3-5: Schematic drawing that illustrates the slowing down process of the beam in the $[\text{CH}_2]_n$ target	36
3-6: Level structure in ^{15}F	37
3-7: Stopping power curves for protons and alphas in silicon.....	41
3-8: Generalized counting electronics	43
3-9: An example of 2D-gating process: $^{14}\text{N}+\text{p} \rightarrow ^{15}\text{O}$	45

4-1: Nitrogen gas-cell target system	51
4-2: A four component, differentially pumped skimming system for injecting aero-sols into the ECR ion source.....	52
4-3: Cryogenic trapping system	54
4-4: Particle Identification of (a) $^{22}\text{Ne}^{8+}$ and $^{11}\text{B}^{4+}$, (b) $^{11}\text{C}^{4+}$ and $^{11}\text{B}^{4+}$, and (c) $^{11}\text{C}^{6+}$	56
4-5: The transfer-line connecting the BIF and the 88-Inch Cyclotron.....	58
4-6: Target system for activity production at the Biomedical Isotope Facility	59
4-7: System for transporting activity between the two accelerator buildings	61
4-8: Capillary-outlet pressure and activity observed in the cryogenic trap during a typical transfer between the two accelerator buildings	62
4-9: System for injection of activity into the AECR-U ion source at a controlled rate	63
4-10: Transfer of ^{11}C activity from the cryogenic trap to the reservoir.....	65
4-11: System for production of H_2^{14}O and conversion to $[^{14}\text{O}]\text{CO}_2$	67
4-12: The $\Delta\text{E-E}$ spectra showing the ^{14}O beam quality	69
5-1: Target and detector setup	78
5-2: Measured α -spectrum at a degraded 93 MeV ^{11}C beam.....	79
5-3: α spectra from the $^{197}\text{Au}(^{12}\text{C},\text{xn})^{209-\text{x}}\text{At}$ and $^{197}\text{Au}(^{11}\text{C},\text{xn})^{208-\text{x}}\text{At}$ reactions at various energies.....	80

5-4: $^{197}\text{Au}(^{12}\text{C},\text{xn})^{209-\text{x}}\text{At}$ excitation functions.....	83
5-5: Measured evaporation residue and fission excitation functions are compared with statistical model calculations for (a) $^{19}\text{F} + ^{188}\text{Os}$ and (b) $^{19}\text{F} + ^{192}\text{Os}$ system	84
5-6: $^{197}\text{Au}(^{11}\text{C},\text{xn})^{208-\text{x}}\text{At}$ excitation functions.....	86
6-1: Known energy levels of ^{15}F and ^{15}C	92
6-2: The experimental setup for the $^{14}\text{O} + \text{p}$ thick target elastic resonance scattering experiment	93
6-3: The proton spectrum for the $\text{p}(^{14}\text{N},\text{p})^{14}\text{N}$ reaction.....	96
6-4: The energy corrections for protons produced by two beams: 120 MeV ^{14}N and ^{14}O	97
6-5: The excitation functions for two $\text{p}(^{14}\text{O},\text{p})^{14}\text{O}$ runs.....	101
6-6: The final excitation function and fitted curves.....	103
6-7: The comparison of results from three different labs using the same $\text{p}(^{14}\text{O},\text{p})^{14}\text{O}$ reaction.....	106
6-8: TES: Experimental and calculated energy levels of the $^{15}\text{C} - ^{15}\text{F}$ mirror nuclei.....	110
6-9: Single-nucleon separation energies	112
7-1: Decay scheme of ^{18}Ne	117
7-2: Population of the 6.15 MeV 1^- resonance in ^{18}Ne with 4.67 MeV ^{14}O	118

LIST OF TABLES

2-1: RIB facilities using the PF method, existing or under construction	6
2-2: RIB facilities using the ISOL method and a post-accelerator, either existing or under construction.....	17
2-3: Next-generation ISOL and In-Flight RIB facilities proposed in Europe and the USA.....	18
2-4: Representative examples of beam requirements for the general research areas discussed in this report and schematically illustrated in Fig. 2-3	20
4-1: Ionization efficiencies and hold-up times of the 88-Inch Cyclotron's ECR ion sources	54
5-1: α -decay properties for At and Po isotopes	72
5-2: Predicted $^{197}\text{Au}(\text{C},\text{xn})^{208-\text{x}}\text{At}$ cross sections at different ^{11}C beam energies.....	74
5-3: Measured and predicted cross section ratios in $(^{11}\text{C},\text{xn})$ and $(^{12}\text{C},\text{xn})$ channels.....	88
6-1: The R-matrix parameters for ^{15}F from $\text{p}(^{14}\text{O},\text{p})^{14}\text{O}$	103
6-2: Comparison of the results for the energy levels of ^{15}F	107

6-3. The IMME fitting parameters for $J^\pi=1/2^+$, $T=3/2$

in ^{15}O with different values for the ^{15}F ground state..... 108

ACKNOWLEDGMENTS

This dissertation would have been impossible without the assistance of many people. I want to thank my advisor, Professor Joseph Cerny, for his years of patience, guidance, and unwavering support. I would like to thank Dr. Dennis Moltz, for his invaluable knowledge and skills of experimental systems and his persistence through experimental adversity. I also want to thank Dr. Larry Phair for leading me through the CAVE 4A scattering chamber, electronics, and data acquisition system.

I am deeply grateful to the other members of the Cerny Group, both past and present, including graduate students Mike Rowe (later as a post-doc) and Dongwon Lee, and post-docs James Powell (later as staff), Kari Perajarvi and Rainer Joosten, and visiting scholars Peter Haustein and Xiaoji Xu, and undergraduate students Mitch André Garcia, Thazin Win and James Lee. I would like to thank Rick Norman, Dan Z.Q. Xie, Daniela Leitner, Peggy McMahan, and the late Ruth-Mary Larimer in the Nuclear Science Division and Jim O’Neil and Henry. F. VanBrocklin in the Biomedical Isotope Facility of the Life Science Division for assistance in the BEARS project.

I also wish to thank other scientific and technical staff at the 88-Inch Cyclotron for helping me out countless times. Particular thanks go to Fred Perry, Bill Tiffany, and the rest of the 88-Inch Cyclotron machine shop staff for

building equipment and to take care of beamline, to Jim Morel and the whole cyclotron crew for providing great beams, and to Bob Fairchild for assistance with EH&S issues. I also want to thank “Doty” (Theodosia) Valrey, and other staff in the Department of Chemistry, University of California, Berkeley for making my graduate life much easier. Thanks also to the administrative staff at LBNL. My sincere gratitude to all of you.

Saving the best for last, as the first to be graduated from college and graduate school, I would like to thank my family. Thanks to my parents, brothers and sisters for their love and support. Thanks to my wife Birong and daughter YaYa for their assistance and strong support, including the nights that I was away on experiments, and for the few moments I almost gave up. They will never know how grateful I am for all their support and help. I definitely would not be here if it weren’t for them and I am forever indebted to them.

And finally my thanks to the American people. This work was supported by them through the Director, Office of Energy Research, Division of Nuclear Physics of the Office of High Energy and Nuclear Physics of the U. S. Department of Energy under Contract DE-AC03-76SF00098.

C H A P T E R 1

INTRODUCTION

1.1 Toward and Beyond the Proton Dripline with Radioactive Ion Beams

Nuclear science, including both nuclear physics and nuclear chemistry, is a subject that explores the structures and properties of atomic nuclei, nuclear reactions, the nature of radioactivity, and the synthesis of new isotopes. Nuclear properties, among which are mass, radius, relative abundance (for stable nuclides), decay modes and half-lives (for radioactive nuclides), reaction modes and cross sections, spin, magnetic dipole and electric quadrupole moments, and excited states [Kra88], no doubt are one of the most important sources for understanding the nuclear system. There are about 2500 known nuclides and among them approximately 270 are stable and 50 are naturally radioactive.

Figure 1-1 shows the nuclear landscape. The black squares, which indicate the stable nuclides, define the valley of stability. So far, most experimental studies of nuclear properties have focused on nuclei either in or near this valley

[Cas00]. The white region neighboring the stable nuclides represents known, short-lived nuclides that have been produced and studied in the laboratory, totaling about 2000. For many of them, there is only evidence of their existence; their basic nuclear properties remain to be measured. Beyond these nuclides, but still inside the region delineated by the proton and neutron driplines, some 4000 additional nuclides are predicted to exist. The proton and neutron dripline boundaries occur where the binding energy of the last proton or neutron becomes zero. When the driplines are reached and even crossed, many new interesting phenomena can be observed, such as halo nuclei, neutron skin, and new doubly magic nuclei.

The study of nuclei far from stability has received much attention recently. As in other physical systems, measurements at the limits can provide important results, which can, when contrasted with more stable systems, shed new light on the underlying symmetries and lead to improved insights into and understanding of the nuclear system. Prominent recent milestones have been: the discovery of additional heavy chemical elements; the observation of neutron halos in light, highly neutron-rich nuclei, which was immediately followed by a widespread theoretical effort that has considerably advanced our understanding of this phenomenon; and the experimental mapping of the nuclear shell structure far from stability, reaching in some cases the neutron or proton driplines.

On the proton rich side, many interesting questions arise. The proton dripline lies much closer to the valley of stability than the neutron dripline. Therefore, it has been possible to establish the proton dripline for most of the

elements up to and even beyond lead. Near the proton dripline, many interesting physics questions have been explored. Among them are proton radioactivity

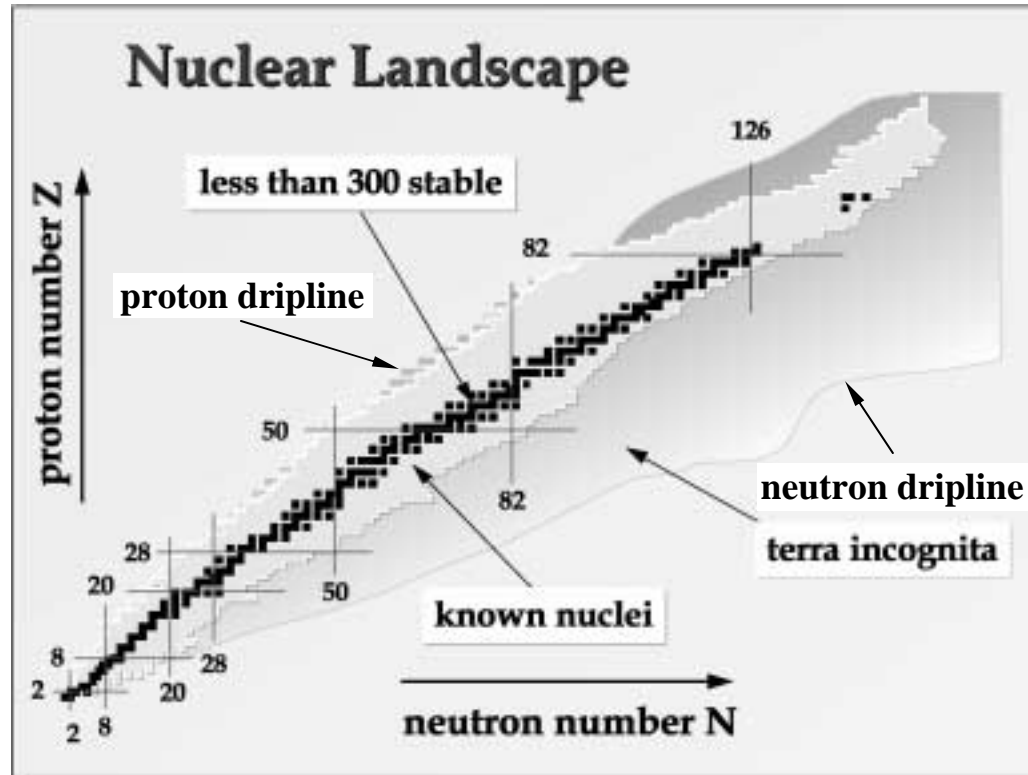


Fig. 1-1: Nuclear landscape showing the known nuclei and terra incognita [Cas00]. The black squares represent the stable nuclides. The adjacent region represents known short-lived unstable nuclides. Beyond that, but inside the region bounded by the two driplines, are nuclides that are yet to be explored (terra incognita).

and beta-delayed two proton emission, as well as nuclear structure beyond the proton dripline; the effects of the proton-neutron interaction and the prospects for emergence of nuclear superconductivity; possible isospin breaking interactions in mirror nuclei; novel nuclear shapes; and the properties of nuclei impor-

tant in the nucleosynthesis in stars. Very proton rich nuclei are also important for tests of the standard model and studies of the astrophysical rapid proton capture process [Cas00].

There remain difficulties in reaching nuclei very far from stability. For example, although near dripline nuclides may be produced in fusion-evaporation reactions with the combination of stable nuclear beams and stable or near-stable targets, the production cross sections can be very small. In addition, such reactions are not very selective; many other radioactive nuclei will be produced simultaneously in far greater yields.

Several additional factors make the study of near dripline proton-rich nuclei particularly challenging. First, the high levels of radiation surrounding the target during bombardment often require that the activity be transported away from the target area for counting. Second, it is common for exotic nuclei to have half-lives shorter than one second because the energy available for beta decay increases rapidly as the dripline is approached. This necessitates that transport methods be very fast. Third, beta-activity levels observed in these experiments are many orders of magnitude greater than the direct proton or beta-delayed proton activities of interest; thus, it is critical that the protons can be unambiguously separated from the beta-decay “background.” Finally, the small reaction cross sections for the production of nuclei far from stability make the maximization of transport and detection efficiencies critical [Row98]. These challenges have spurred the development of many novel experimental techniques. One re-

cent area of progress is in the development of radioactive ion beams (RIBs), which provide variable energy beams of exotic nuclei.

With RIBs characterized by beam intensities of $\sim 10^3$ - 10^8 particles/second, experiments studying near dripline or even beyond dripline nuclides may be produced with direct or compound nucleus reactions, and favor cross sections which are large. The reaction mechanisms of interest can be relatively simple and straightforward. However, the experiments using RIBs require complicated beam and detector technology development.

This thesis describes the efforts to develop a RIBs capability at Lawrence Berkeley National Laboratory and examines the properties of several proton-rich exotic nuclei using the techniques of α -decay spectroscopy and proton elastic scattering spectroscopy.

1.2 Thesis Organization

Following this introduction, Chapter 2 will present general background about RIBs, including some discussion associated with RIB technology, which will be necessary for understanding the experimental measurements in this thesis. Chapter 3 discusses the general aspects of the experimental apparatus and techniques that have been utilized in this work. Chapter 4 specifically deals with the research and development of ^{11}C and ^{14}O RIBs produced by the Berkeley Experiments with Accelerated Radioactive Species (BEARS) project. Chapter 5 presents the results from the first application of the ^{11}C RIB produced by

BEARS to investigate excitation functions in reactions of $^{197}\text{Au}(\text{C},\text{xn})^{208-\text{x}}\text{At}$.

Chapter 6 presents the results from the first application of the ^{14}O RIB produced by BEARS to investigate the energy levels of ^{15}F by elastic scattering reactions of $\text{p}(\text{O},\text{p})^{14}\text{O}$ in an inverse kinematics thick-target arrangement. Chapter 7 contains concluding remarks and discusses possible future projects with RIBs provided by BEARS.

Since the pioneering experiments on the interaction cross sections and nuclear radii of exotic He, Li, and Be nuclides with RIBs at Berkeley in the mid-80s [Tan85a, Tan85b], experimental studies with RIBs have been widely expanded. Using projectile fragmentation, high-energy heavy-ion beams have been used to produce a wide variety of isotopes. Secondary beams of ^6He , ^8He , ^8Li , ^9Li , ^7Be , and ^{10}Be were produced through the projectile fragmentation of an 800 MeV/nucleon ^{11}B primary beam bombarding a Be production target [Tan85b]. ^{11}Li was produced from a ^{20}Ne primary beam [Tan85b]. These exotic-isotope beams represent one of the earliest experimental applications of radioactive ion beams. Since the Bevalac and SuperHILAC involved in the RIB research at LBNL were shut down in the beginning of the nineties, an ISOL type BEARS project was proposed by Cerny [Cer96]. Following preliminary tests at the 88-Inch Cyclotron, a transfer line was constructed to couple a cyclotron in the Biomedical Isotope Facility with the 88-Inch cyclotron [Cer99, Pow00, Pow03]. Currently, two beams have been developed: ^{11}C , with an intensity up to 2×10^8 ions per second on target [Joo00, Pow00], and ^{14}O , with an intensity up to 3×10^4 ions per second on target.

A relatively simple fusion-evaporation reaction $^{197}\text{Au}(^{11}\text{C},\text{xn})^{208-\text{x}}\text{At}$ has been investigated to demonstrate the application of the radioactive ^{11}C ion beams from BEARS. These results have been compared with those from $^{197}\text{Au}(^{12}\text{C},\text{xn})^{209-\text{x}}\text{At}$ with a stable ^{12}C beam producing the same astatine isotopes to test fusion-evaporation model code predictions, i.e., ALICE [Bla82], HIVAP [Rei81], and PACE [Gav80]. These results are useful in understanding the deexcitation process of the compound nuclei [Joo00].

In the late seventies, the energy levels of ^{15}F were investigated by Kekelis *et al.* [Kek78] and Benenson *et al.* [Ben78] with the low cross section transfer reaction $^{20}\text{Ne}(^{3}\text{He}, {}^{8}\text{Li})^{15}\text{F}$. Only two levels have been observed so far, the ground state and the first excited state. The adopted values for the energies of these two levels are 1.47 ± 0.13 MeV and 2.77 ± 0.10 MeV relative to the mass-energy of the proton and ^{14}O [Ajz91]. The ground state is very broad with a width of 1.0 ± 0.2 MeV, which is difficult to measure accurately. The width for the first excited state is 0.24 ± 0.03 MeV. Since the cross sections were small, about 1-4 μb , the statistics were poor for both states. Recently, these two levels have been re-investigated by several authors [Gre97, Lep03, Pet03, Gol04] with two reactions: the elastic scattering reaction $^{14}\text{O} + \text{p} \rightarrow {}^{15}\text{F}$ [Pet03, Gol04] and a transfer reaction $^{16}\text{O}(^{14}\text{N}, {}^{15}\text{C})^{15}\text{F}$ [Lep03]. In addition, the properties of these two states have been predicted from theoretical calculations using a conventional Woods-Saxon potential plus a surface term deduced from the mirror nucleus ^{15}C [Gre97]. While most of these experimental studies agree well with one another on the position of the first excited state, questions have remained about

the energy and width of the broad ground state. To clarify this question, a new measurement of the ^{15}F levels using elastic scattering of ^{14}O on a hydrogen target (polyethylene) in an inverse kinematics thick-target arrangement has been completed and analyzed.

By presenting the results of the radioactive ion beam development and the reaction measurements discussed in the preceding paragraphs, it is the goal of this thesis to further demonstrate the value of radioactive nuclear beams and corresponding technological development as new tools for probing the properties of highly unstable proton-rich nuclides.

C H A P T E R 2

RADIOACTIVE ION BEAMS

2.1 Introduction

The burgeoning field of Radioactive Ion Beam (RIB) research is one of the most exciting developments in nuclear science in the last two decades. Since the pioneering experiments with modern projectile fragmentation type radioactive beams at Berkeley in the mid-80s, experimental studies with radioactive ion beams have been widely expanded. The number of nuclei in the nuclear chart able to be accessed with these beams has been increased. Numerous experimental studies of far from stability nuclei with both stable and radioactive ion beams show many important differences in their structure from that of stable nuclei. New forms of nuclear structure, such as neutron halos and neutron skins, have been found in unstable nuclei. There are changes in the nuclear shell structure, for example the disappearance of the magic numbers known for stable nuclei and the appearance of new magic numbers in unstable nuclei. The importance of radioactive ion beams has been being well recognized in nuclear science, astrophysics, and other fundamental and applied fields [Cas00, Ver03, Jon03].

Though the utilization of radioactive ion beams can be traced back to 1951 [Kof51a, Kof51b, Kof51c], the concept of radioactive ion beams was first mentioned by J. P. Bondorf in 1966. He pointed out “the rich field of information that would be opened by a future use of unstable targets and projectiles in nuclear reaction study” of nuclides far from the stability line [Bon67]. Traditionally, the ions produced by an accelerator are stable or (sometimes) long-lived radioactive isotopes (for example, ^{14}C , $t_{1/2} = 5730$ years). With radioactive ion beam technology, beams of unstable nuclei are available from the new configurations of accelerators. The half-lives of the unstable nuclei that can be utilized cover a broad range, from milliseconds to hours. Given the rapid development of radioactive ion beams during the past two decades, it is not possible to cover all the details about these beams. Only the general aspects of radioactive ion beams will be dealt with in this chapter.

Many different techniques have been used to produce RIBs [Nit90a, Nit90b, Nit92, Nit93]. The two major techniques are Projectile Fragmentation (PF) and the Isotope Separator-on-line (ISOL). While the Projectile Fragmentation technology was first tested in about 1972 with the Bevatron at LBNL [Hec72], the ISOL technology was developed much earlier, in the fifties. This latter technology was highly developed with the ISOLDE at CERN [Kof76]. The ISOL technology will be used for the next generation of RIB accelerators: the planned Rare Isotope Accelerator (RIA) in the United States and the European Isotope-separation-on-line radioactive ion beam facility (EURISOL). Since the ISOL method was the first to be used to develop radioactive ion beams and

since, in addition, the BEARS project uses the ISOL technology, it is of interest to describe the history of the ISOL method.

The earliest experiment with RIBs can be traced back to 1951 at the Niels Bohr Institute in the University of Copenhagen, Denmark [Kof51a, Kof51b, Kof51c]. The experimental purpose was to measure the recoil momentum of heavy decay products from the β -decay of neutron-rich noble gas isotopes of Kr and Xe. Although the experiment was simple, it incorporated all the basic elements suggested for use in succeeding generations of RIB facilities.

The experimental arrangement included two main instruments of the time: a cyclotron providing an 11 MeV deuteron beam and an isotope separator. The deuterons bombarded an internal beryllium target producing neutrons. These neutrons then bombarded a uranium target, after having been moderated by paraffin surrounding the target. Gaseous fission products were transported out of the target by NH_3 , CO_2 , and H_2O gases from the decomposition of $(\text{NH}_4)_2\text{CO}_3$ baked under vacuum and brought to the ion source of the isotope separator. At this point, isotopes of the noble gases Kr and Xe were ionized, separated, and collected for decay measurements which were carried out with Geiger-Müller counters [Kof76, Han01]. This was the first time that the accelerator, isotope separator and detectors worked simultaneously, providing a truly on-line experiment. Notably, there was not even a term "on-line" until the early sixties.

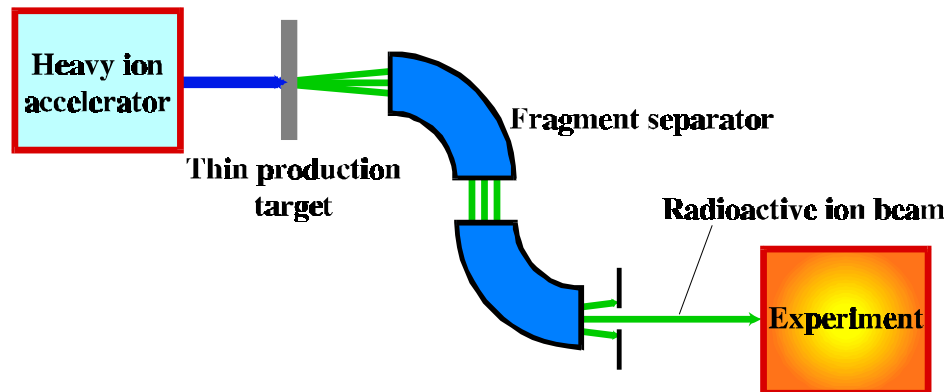
2.2 Methods of Producing Radioactive Ion Beams

Many radioactive ion beam facilities are in operation, under construction, or being proposed. These facilities are mainly based on either Projectile Fragmentation or the Isotope Separator-on-line. Figure 2-1 shows the main features of the two approaches.

In the PF method, medium to high energy (typically 50-2000 MeV per nucleon) heavy ion beams are used to bombard a relatively thin target. The exotic nuclear fragments which are produced are emitted, with much of the momentum of the incoming projectile, at forward angles in the laboratory system. These fragments then pass through a mass separation device which selects a particular A and Z by using a combination of magnetic and energy-loss devices. The exotic beam of interest then proceeds to bombard a target for secondary reactions, or one may make direct measurements on the exotic beam itself.

In the ISOL method, a high intensity (up to 200 μ A), high energy (500-1000 MeV) light ion beam (p , d , 3He) bombards a thick, hot, heavy nuclear target. The products diffuse and desorb out of the target. They are then transported to the ion source of an isotope separator. After separation, the beam can be either used at low energies or be post accelerated to higher desired energies for nuclear reactions.

Projectile Fragmentation



ISOL

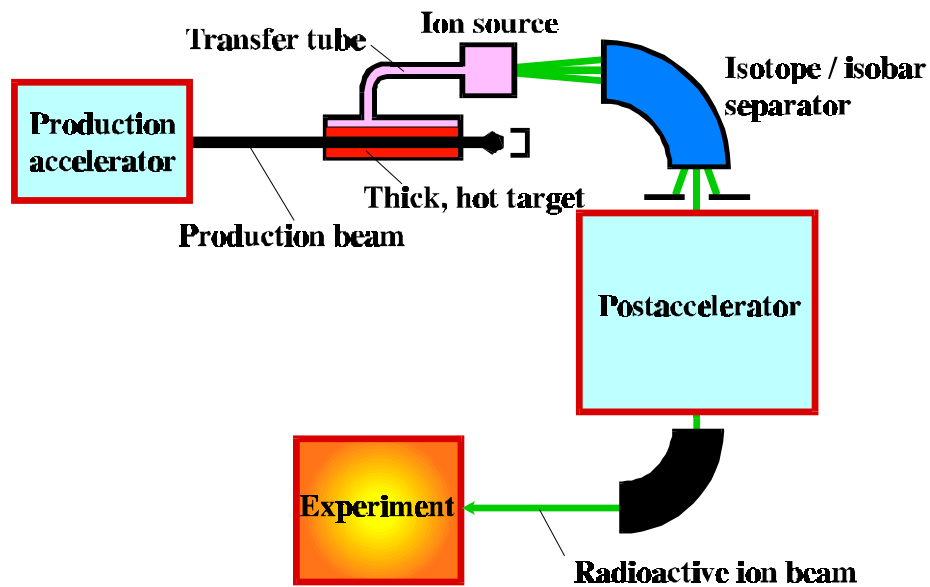


Fig. 2-1: Schematic representations of the two basic types of radioactive ion beam facilities. From the 1997 Columbus “White Paper” Report, see also [Cas00].

Each method has its strong and weak points. The PF methods have two major advantages. First, the exotic nuclides are produced in PF almost instantaneously, within microseconds, which is significantly below the timescale of β -

decay. (This is because the reaction products recoil out of the target at approximately the same velocity as the primary beam.) Secondly, there is no Z restriction. All species produced in the target are available for isotope separation. The main disadvantages of PF relate to the beam intensity, quality and energy. Because of the lower primary beam intensity ($\sim 1 \text{ p}\mu\text{A}$) and the relatively thin target ($1\text{g}/\text{cm}^2$) technology, the PF method suffers from lower secondary beam intensity and poorer beam quality, i.e., wider energy spread, higher level of beam contamination (multiple Z values) and large emittance. Also the secondary beam energies of $\sim 50 \text{ MeV}$ per nucleon or higher, found in many PF facilities, may be suited for nuclear reaction studies and some nuclear structure studies, but are too high for most of nuclear structure research. Although the energy of the PF secondary beam can be decreased either by degraders or by a storage ring (cooler and decelerator) to lower energies, there are still problems. The degrader approach involves multiple secondary reactions, scattering, and straggling, therefore resulting in poorer beam quality. The storage ring method is limited by secondary beam emittance/acceptance, long cooling times, and space charge problems.

In contrast, the ISOL approach provides higher beam intensity, superior beam quality and readily flexible beam energies. Exotic nuclei are produced by an intense light ion beam (up to $200 \mu\text{A}$ of H, D, or ^3He beams) on, typically, a thick heavy nuclide target (about $100 \text{ g}/\text{cm}^2$). The secondary beam in ISOL can be $10^4\text{--}10^5$ higher than in the PF. With its chemical separation, the beam has much better Z selection but, of course, the ISOL approach is not necessarily

applicable to all elements. With post-acceleration, the secondary beam can be varied at will. The disadvantages of the ISOL method are the lower (or ~zero) production rate for certain elements with special chemical properties, longer separation times (~100 milliseconds or more), more unwanted radioactivity and a possible high radiation field, and post-acceleration requirements.

The two methods are complementary both in approach and, frequently, in physics. Hybrid methods combining both PF and ISOL features are being developed. For example, in a PF based ISOL method, the exotic nuclei are produced with a much thinner target than in ISOL, separated magnetically while in-flight, stopped in helium gas, ionized, and re-accelerated. With this technique, shorter lived exotic nuclei are much more accessible, beam contamination is much decreased, and the beam intensity is still acceptable. The next generation Rare Isotope Accelerator (RIA) in the United States will use this PF based ISOL hybrid method. Figure 2-2 shows a prototype of such an RIB facility.

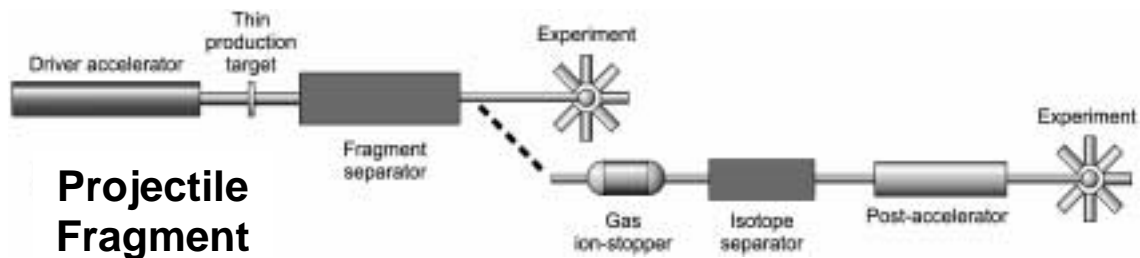


Fig. 2-2: A hybrid PF based ISOL RIB system [Ver03].

Table 2-1: RIB facilities using the PF method, existing or under construction [Ver03, Nol02]

Location	RIB starting date	Primary accelerator	Fragment separator
GANIL Caen, France	1985	2 separated-sector cyclotrons up to 95 A MeV	LISE SISSI
GSI Darmstadt, Germany	1989	UNILAC + SIS up to 1 A GeV	FRS, ESR
Flerov Laboratory Dubna, Russia	1996	2 cyclotrons	ACCULINNA COM-BAS
KVI Groningen, Netherlands	(2005)	Superconducting cyclotron AGOR $K = 600$	TRIMP
NSCL East Lansing, USA	1991	Superconducting cyclotron K1200 up to 200 A MeV	A1200 Projectile Fragment Separator
NSCL East Lansing, USA	2001	Superconducting cyclotrons K500-K1200	A1900 Projectile Fragment Separator
RIKEN Saitama, Japan	1992	Ring-cyclotron up to 135 A MeV	RIPS Saitama, Japan
RIKEN Saitama, Japan	(2005)	Ring-cyclotrons up to 400 A MeV (light ions)	3 fragment separators storage & cooler rings up to 150 A MeV (heavy ions)
IMP Lanzhou, China	1997	Separated-sector cyclotron $K = 450$, up to 80 A MeV	RIBLL proposed storage & cooler rings (2004)
ATLAS/ANL Argonne, USA	1998	Superconducting linac 5-10 A MeV, 400 pnA	split-pole FMA
MARS & Big Sol @ Texas A&M, USA	1992 & 2002	K500 superconducting cyclotron 100-200 pnA	MARS, Big Sol
TWINSOL Notre Dame/UMich, USA	1987	FN Tandem 10 MeV, 1 μ A	a pair of in-line superconducting solenoid magnets

Table 2-1 lists RIB facilities using the In-Flight method, existing or under construction. Table 2-2 lists the RIB facilities using the ISOL method and a post-accelerator, either existing or under construction. Table 2-3 lists the next

generation ISOL and In-Flight (PF) RIB facilities proposed in Europe and the USA.

Table 2-2: RIB facilities using the ISOL method and a post-accelerator, either existing or under construction [Ver03, Nol02]

Location	RIB Starting Date	Driver	Post-accelerator
Louvain-la-Neuve Belgium	1989	cyclotron p, 30 MeV, 200 μ A	cyclotrons K = 110, 44
SPIRAL: GANIL Caen, France	2001	2 cyclotrons heavy ions up to 95 A MeV, 6 kW	cyclotron CIME K = 265, 2–25 A MeV
SPIRAL-II: GANIL Caen, France	(2008)	s/c linear accelerator LINAG heavy ions up to 40 A MeV	cyclotron CIME K = 265, 2–25 A MeV
REX ISOLDE: CERN Genève, Switzerland	2001	PS booster p, 1.4 GeV, 2 μ A	Linac 0.8-3.1 A MeV
MAFF Munich, Germany	(2008)	reactor 10^{14} n/cm ² .sec	Linac up to 7 A MeV
EXCYT Catania, Italy	(2004)	cyclotron heavy ions	15-MV tandem 0.2–8 A MeV
HRIBF Oak Ridge, USA	1997	cyclotron p, d, α , 50-100 MeV, 10-20 μ A	25-MV tandem
ISAC-I: TRIUMF Vancouver, Canada	2000	cyclotron p, 500 MeV, 100 μ A	Linac up to 1.5 A MeV
ISAC-II: TRIUMF Vancouver, Canada	(2005)	cyclotron p, 500 MeV, 100 μ A	Linac up to 6.5 A MeV
BEARS: LBNL Berkeley, USA	1999	cyclotron p, 11 MeV, 40 μ A	Cyclotron K = 140, 1-20 A MeV
ATLAS: ANL Argonne, USA	1994	Cyclotron p, 10 MeV, \geq 100 μ A ANL IPNS P, 50 MeV, \sim 15 μ A	FN Tandem + SC Linac, 0.5-5 A MeV

Table 2-3: Next-generation ISOL and In-Flight RIB facilities proposed in Europe and the USA [Ver03, Nol02]

Location	Driver	Post-accelerator	Fragment	Type of separator facility
Europe (Germany)	synchrotron, heavy ions: 1.5 A GeV	----	'Super-FRS'	In-Flight GSI
Europe: EURISOL	protons, 1 GeV, 1-5 MW	SC linac, up to 100 A MeV	----	ISOL
USA: (RIA) Rare Isotope Accelerator	900 MeV protons heavy ions: 400 A MeV, 100 kW	ATLAS linac 8-15 MeV	4-dipole separator	ISOL, In-Flight

2.3 Opportunities with Radioactive Ion Beams

Radioactive ion beams open new opportunities for the study of nuclear structure, nuclear reactions, astrophysics and other fundamental and applied fields. With radioactive ion beams, the properties of nuclei will be explored to answer key scientific questions about the origin of the elements, the limits of nuclear existence, the properties of nuclei with extreme ratios of neutrons to protons, the equation of state of neutron-rich nuclear matter, and physics beyond the standard model of particle physics.

The general scientific opportunities with high intensity and exotic radioactive ion beams are schematically illustrated in Fig. 2-3. This figure shows regions of interest in the nuclear landscape that can be explored with a next-generation radioactive ion beam facility. Each topic is given a circled number which corresponds to an entry in Table 2-4 in which representative examples for each area of interest are given in order to quantify beam requirements and experimental approaches. The circled numbers represent examples of reactions

and techniques, beams, desired intensities, and energy ranges for each area of interest. The desired beam intensities, while not available from present first-generation radioactive ion beam facilities, could be achievable with expected new technological developments at an advanced radioactive ion beam facility. These examples are generally representative of a large class of similar studies. The examples are given to outline the overall performance characteristics needed for an exploration of the new science opportunities. They are taken from the “Columbus” White Paper 1997; see also [Cas00].

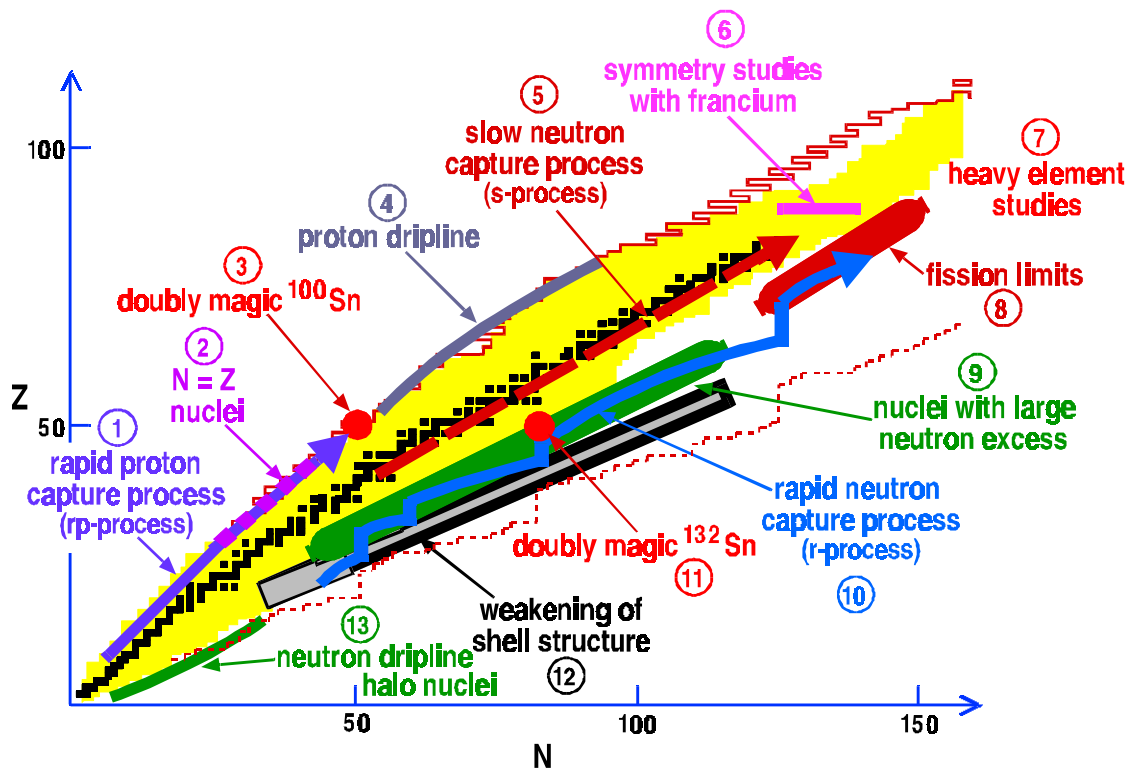


Fig. 2-3: Illustration of research opportunities with high intensity radioactive ion beams.

From the “Columbus” White Paper 1997, see also [Cas00].

Table 2-4: Representative examples of beam requirements for the general research areas discussed in this report and schematically illustrated in Fig. 2-3. Only a few typical ion species can be shown for each entry to exemplify the intensity and energy ranges needed for performing experiments in these areas.

Physics Topics*	Reactions and Techniques	Beams	Desired Intensities		Energy Range [MeV/u]
			[particles/sec]		
1. rapid proton capture (rp processes)	transfer, elastic, inelastic, radiative capture, Coulomb dissociation	^{14}O , ^{15}O , ^{26}Si , ^{34}Ar , ^{56}Ni	$10^8\text{-}10^{11}$ $10^5\text{-}10^{11}$		0.15-15
2. reactions with and studies of N=Z nuclei, symmetry studies	transfer, fusion, decay studies	^{56}Ni , ^{62}Ga , ^{64}Ge , ^{68}Ge , ^{67}As , ^{72}Kr	$10^4\text{-}10^9$		0.1-15
3. decay studies of ^{100}Sn	decay	^{100}Sn	1-10		low energy
4. proton dripline studies	decay, fusion, transfer	^{56}Ni , 64 , ^{66}Ge , ^{72}Kr	$10^6\text{-}10^9$		5
5. slow neutron capture (s-process)	capture	134 , ^{135}Cs , ^{155}Eu	$10^8\text{-}10^{11}$		0.1
6. symmetry studies with francium	decays, traps	$^{\text{A}}\text{Fr}$	10^{11}		low energy
7. heavy element studies	fusion, decay	$^{50\text{-}52}\text{Ca}$, ^{72}Ni ^{84}Ge , ^{96}Kr $^{140\text{-}144}\text{Xe}$, 142	$10^4\text{-}10^7$ $10^6\text{-}10^8$ $10^7\text{-}10^{11}$		5-8
8. fission limits	fusion-fission	^{146}Cs ^{142}I , $^{145\text{-}148}\text{Xe}$, $^{147\text{-}150}\text{Cs}$	$10^4\text{-}10^7$		5
9. rapid neutron capture (r-process)	capture, decay, mass measurement	^{130}Cd , ^{132}Sn , ^{142}I	$10^4\text{-}10^9$		0.1-5
10. nuclei with large neutron excess	fusion, transfer, deep inelastic	$^{140\text{-}144}\text{Xe}$, 142 ^{146}Cs ^{142}I , $^{145\text{-}148}\text{Xe}$, $^{147\text{-}150}\text{Cs}$	$10^7\text{-}10^{11}$ $10^2\text{-}10^7$		5-15
11. single-particle states/ effective nucleon-nucleon interactions	direct reactions, nucleon transfer	^{132}Sn , ^{133}Sb	$10^8\text{-}10^9$		5-15
12. shell structure, weakening of gaps, spin-orbit potential	mass measurement, Coulomb excitation, fusion, nucleon transfer, deep inelastic	$^{\text{A}}\text{Kr}$, $^{\text{A}}\text{Sn}$, $^{\text{A}}\text{Xe}$	$10^2\text{-}10^9$		0.1-10
13. (near) neutron-dripline studies, halo nuclei	mass measurement, nucleon transfer	^8He , ^{11}Li , ^{29}Ne , ^{31}Na , ^{76}Cu	$10^6\text{-}10^8$ $10^3\text{-}10^6$		5-10

*The numbers 1-13 refer to the corresponding labeling in Fig. 2-3.

Among the research interests shown in Fig. 2-3 and Table 2-4, the applications of radioactive ion beams to proton-rich nuclei will be emphasized in this thesis. One of the reasons is that BEARS provides two proton-rich radioactive

ion beams, ^{11}C and ^{14}O . With them, some proton rich nuclei can be explored.

Another reason is that the proton dripline lies much closer to the valley of stability than the neutron dripline.

2.4 Summary

Radioactive ion beams as a new technology bring unprecedented opportunities to nuclear physics, astrophysics, and other fields. The RIB facilities, either with the projectile fragmentation method or the Isotope Separation-On-Line method, or a hybridization of both, are providing, or are going to provide, exciting results for our improved understanding of nuclear matter.

C H A P T E R 3

EXPERIMENTAL EQUIPMENT AND TECHNIQUES

3.1 Preparation of Nuclides

All the experiments in this thesis were performed at the 88-Inch Cyclotron at Lawrence Berkeley National Laboratory. All the beams except ^{11}C and ^{14}O originated at the 88-Inch Cyclotron. The ^{11}C and ^{14}O were produced by a small cyclotron in the Biomedical Isotopes Facility and transferred to the 88-Inch Cyclotron for acceleration. This add-on capability of light radioactive ion beams at the 88-Inch Cyclotron is called the Berkeley Experiments with Accelerated Radioactive Species (BEARS). The BEARS will be described in detail in Chapter 4.

3.1.1 The 88-Inch Cyclotron

The 88-inch Cyclotron was constructed from the late fifties to the early sixties and commissioned in 1962 [Kel62]. The cyclotron is an azimuthally-varying field (AVF) cyclotron. Originally, the cyclotron was designed to accelerate light isotopes exclusively. With improvements in ion source technology, i.e.,

the electron cyclotron resonance (ECR) ion source, it can accelerate almost every isotope from proton to uranium as well as a group of mixed isotopes (cocktail mode) [Cla83, Xie91, Lyn98, Xie00, Lei03]. Currently three ECR ion sources, LBL-ECR, AEGR-U and VENUS, are (or will be) used to accelerate both stable and radioactive isotopes. The maximum energy (and corresponding intensity) for the ion beams used in this work [Lyn98] is: ^1H , 55 MeV/u (6 $\text{e}\mu\text{A}$); ^{12}C , 35 MeV/u ($\sim 1 \text{ e}\mu\text{A}$); ^{14}N , 35 MeV/u ($\sim 1 \text{ e}\mu\text{A}$); ^{11}C , 35 MeV/u (up to 2×10^8 particles/second on target); and ^{14}O 35 MeV/u (up to 3×10^4 particles/second on target).

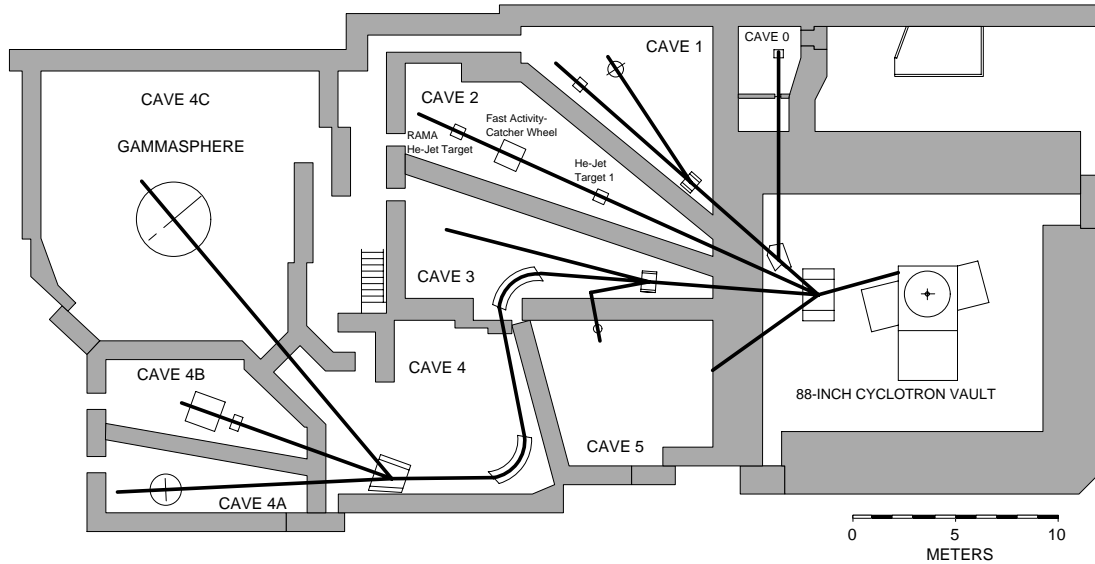


Fig. 3-1: The 88-Inch Cyclotron Facility. All experiments were performed in Cave 2 and Cave 4A [Row98]. Some configurations of the caves have changed during this thesis work. Cave 2 is currently being re-configured as a neutron beamline.

The beams were extracted from the cyclotron and directed into Cave 2 or Cave 4A as shown in Figure 3-1. Cave 2, currently under upgrade, had three different target systems. The upstream helium-jet target was used for production of ^{11}C for a preliminary study of ^{11}C radioactive ion beams for the BEARS (Chapter 4). With different target and detector set-ups, $^{197}\text{Au}(^{11}\text{C},\text{xn})^{208-\text{xn}}\text{At}$ and $^{197}\text{Au}(^{12}\text{C},\text{xn})^{209-\text{xn}}\text{At}$ reactions were also carried out in Cave 2 (Chapter 5).

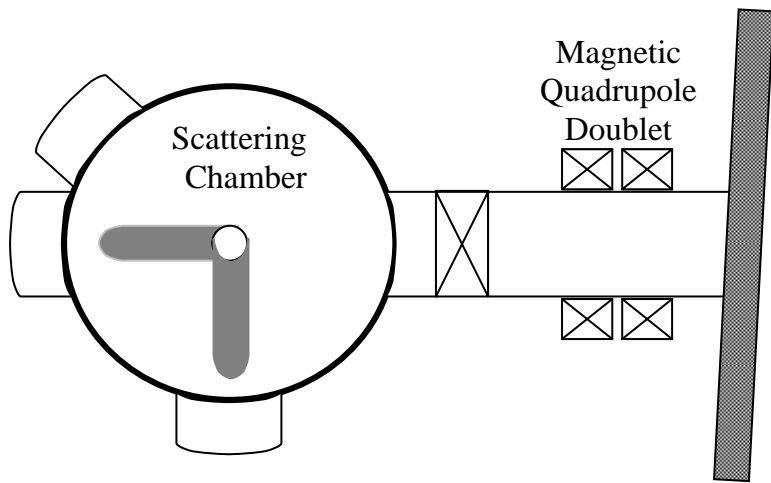


Fig. 3-2: Cave 4A beamline and the scattering chamber. The experiments to investigate light proton rich nuclei are performed in this cave.

Cave 4A has a 60 inch scattering chamber equipped with two, step-servo arms which hold detector modules. The two arms can be controlled to move between 0° and 180° with a precision of about 0.2° . In the center of the chamber, there is an adjustable target holder. Its height adjustment permits 5 targets to be available, with an orientation between -75° to 75° . All of the controls can be performed with step motors, both in Cave 4A and in the counting area. The

vacuum system is made up of a roots pump, an ion pump and a cryo pump. The best vacuum can reach about 5×10^{-6} Torr but most of the time the vacuum is 2×10^{-5} Torr. The investigation of levels in ^{15}F by elastic scattering of ^{14}O on a hydrogen target (such as polyethylene) was performed in Cave 4A (Chapter 6).

3.1.2 Production Reactions for Proton-Rich Nuclides

Traditionally, with reactions of stable beams and stable targets, most studies of proton-rich exotic nuclides have used one of three different nuclear reaction types to produce the activity of interest: direct, fusion-evaporation or fragmentation. The fusion-evaporation reaction has been used in the excitation function measurement of $^{197}\text{Au}(^{11}\text{C},\text{xn})^{208-\text{xn}}\text{At}$ and $^{197}\text{Au}(^{12}\text{C},\text{xn})^{209-\text{xn}}\text{At}$. With more and more radioactive ion beams becoming available, other types of reactions are accessible to explore exotic nuclei. Resonance reactions, for example elastic resonance scattering, are important to explore the levels of bound or unbound proton rich exotic nuclei, which are usually difficult to reach with standard techniques. Elastic resonance scattering has been used in the study of the energy levels of ^{15}F by $^{14}\text{O} + \text{p} \rightarrow ^{15}\text{F}$. While elastic resonance scattering will be discussed in detail later, a brief discussion of other reaction types will clarify why they were used. A more detailed discussion of nuclear reactions may be found elsewhere [Sat83, Kra89, Fes92].

Direct reactions (or peripheral reactions) proceed directly from the entrance channel to the exit channel without the formation of an intermediate state. The reaction products are formed in a single step which occurs on a nuclear time scale, $\sim 10^{-21}$ seconds. Direct reactions include elastic scattering, ine-

lastic scattering, stripping and pickup reactions, quasi-elastic scattering, etc.

The energy levels of the nucleus of interest can be measured from the reaction products directly. The spin and parity of the nuclei can often be deduced from the angular distribution of the reaction products. For example, the mass of ^{15}F was first determined using the $^{20}\text{Ne}(^{3}\text{He}, ^{8}\text{Li})^{15}\text{F}$ pick-up reaction with a cross section of ~ 100 nb/sr [Kek78, Ben78].

As mentioned before concerning the production methods for radioactive ion beams, proton rich exotic nuclides are produced in fragmentation reactions employing high-energy, heavy-ion projectiles (typically, 50-100 MeV/A) bombarding light nuclide targets. After in-flight separation (on the order of μs), the nuclides of interest are recorded with their energy, magnetic rigidity and time of flight (TOF) through the system, which allows their A and Z to be directly and uniquely identified.

In previous chapters, the opportunities with radioactive ion beams have been described as leading to a new frontier in nuclear science. Since many radioactive ion beams are still in the development stage, their intensities are rather low compared with stable beams. While developing techniques will improve the radioactive ion beam intensities for use in future experiments, some relatively unique experiments utilizing the current radioactive ion beams have been used to investigate interesting nuclear problems. One of the experimental techniques currently being utilized is the elastic scattering resonance reaction in inverse kinematics with thick targets, which is especially suitable for nuclei

around the proton dripline which are explored with low beam intensity radioactive ion beams.

3.2 Elastic Resonance Scattering Reactions in Inverse Kinematics with Thick Targets

Elastic Resonance Scattering in Inverse Kinematics with Thick Targets (ERSIKTT) combines the high cross sections of elastic resonance scattering with the energy-scanning efficiency of a thick target and still permits reasonable energy resolution [Art90, Ben93, Hue98, Mar00, Mar01, Gal01]. The inverse kinematics produces forwardly focused reaction products and creates the possibility of making measurements at 0° in the laboratory (180° c.m.).

In this method, a heavy-ion beam at rather low energy (≤ 10 MeV/u) is brought into a scattering chamber and impinges on a thick target, which typically contains hydrogen or helium atoms. The thick target serves simultaneously as an energy degrader for the primary beam, a scattering target and a beam stop. Detectors are placed at forward angles for detection of the energy and angle of the scattered light target ions. The incoming beam ions are continuously slowed down in the thick target, and if their energy at some point along the path corresponds to a resonance in the compound system, the cross section for elastic scattering increases dramatically. The light scattered nuclei have a relatively high energy and a much smaller stopping power than the heavy ions and pass through the target to reach the detectors. To observe reac-

tions at 0° lab (180° c.m.), the target thickness must be chosen so that the beam is stopped in the target.

ERSIKTT is well suited for radioactive ion beams. The relatively low intensities of radioactive ion beams require reactions with large cross sections and experimental setups with high efficiencies. The elastic resonance reactions can have cross sections around 1 barn in the c.m. and even larger (up to 4 times) in the lab system with inverse kinematics.

Depending upon the method of production, the quality of radioactive ion beams can be relatively poor. The energy spread is often not as narrow as that of the stable beams due to production and/or separation requirements. However, using ERSKITT, the energy resolution of the beam is not a primary factor in determining the experimental setup. In addition, the lab resolution and energy spread will be reduced by approximately a factor of 4 in the c.m. system for an experiment performed in inverse kinematics (see section 3.2.1).

3.2.1 Inverse Kinematics

In a conventional experimental setup, the projectile is usually lighter than the target, except in reactions between very light nuclei. Elastic resonance scattering of light particles (p, d, α ...) was performed with conventional kinematics by varying the energy of the light particle in steps of a few keV. The first study with this technique was measuring energy levels of ^{17}F ; it was carried out at the Wisconsin electrostatic generator in the early 50's by scattering of protons on a thin ^{16}O target [Lau51].

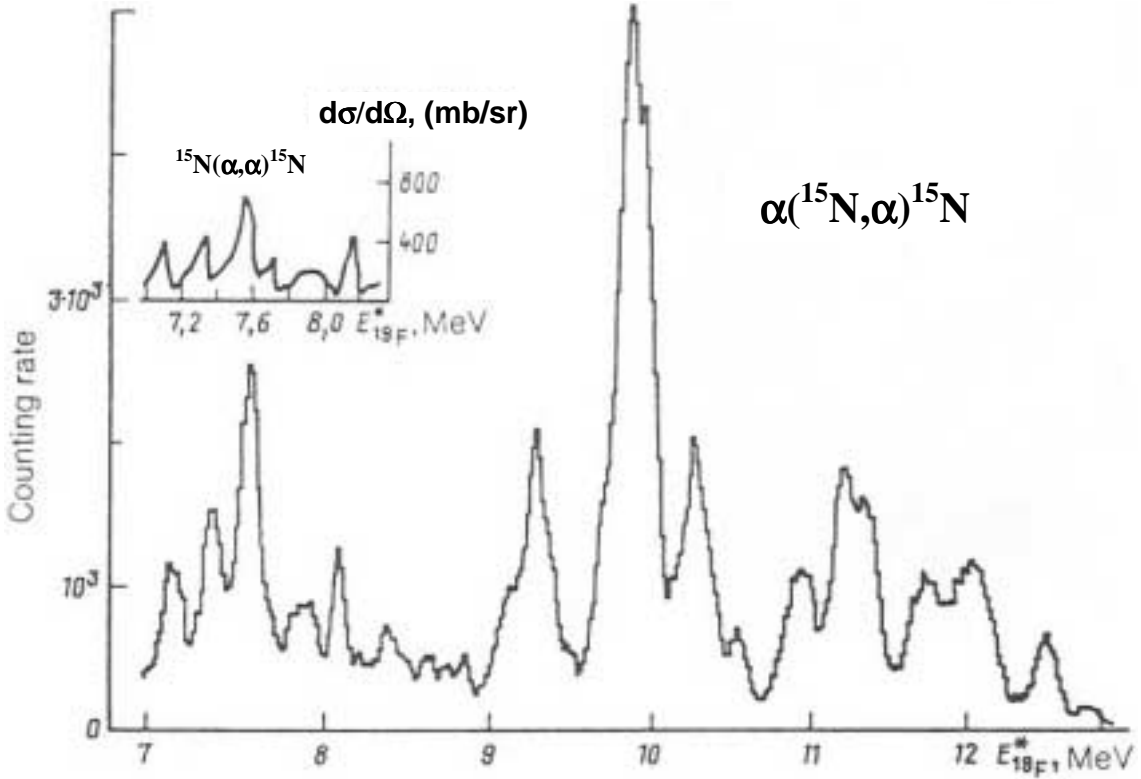


Fig. 3-3: Spectrum of α particles produced from the interaction of 45 MeV ^{15}N with a thick ^4He target at 0° ($\theta_{\text{c.m.}} = 180^\circ$) [Art90]. In the inset, a conventional kinematics measurement at $\theta_{\text{c.m.}} = 169.1^\circ$ is given [Smo61].

As research moved from light ion beams to heavy beams, it became possible to observe the same scattering experiment using an inverse geometry, i.e., with the heavy ion as the projectile and the light ion as the target. This has been shown to have several advantages, especially for radioactive ion beams. One of the early experiments was to scatter ^{15}N on a thick ^4He gas target to investigate α -cluster states in ^{19}F [Art90]. Figure 3-3 compares conventional kinematics with inverse kinematics for the $^4\text{He} + ^{15}\text{N}$ reaction. The first elastic

scattering experiment in inverse kinematics with a RIB was performed to investigate a low-lying 1^- resonance in ^{14}O by scattering ^{13}N on hydrogen in 1991 at Louvain-la-Neuve [Del92].

If an elastic scattering reaction in inverse kinematics is $m(M,m)M$, where M is the heavy projectile and m is the light target ion which is then detected (p , d , $\alpha\dots$), the relationship between the detected laboratory energy of m , $E_{m,\text{lab}}$, and the beam energy $E_{M,\text{lab}}$ is:

$$E_{m,\text{lab}} = 4 \frac{mM \cos^2 \theta_{\text{lab}}}{(m+M)^2} E_{M,\text{lab}} \quad (3-1)$$

It is of interest to compare the detected energy of m in inverse kinematics, $E_{m,\text{lab}}$, with the energy of m in a conventional kinematics (CK) $M(m,m)M$ experiment:

$$E_{m,\text{lab}} = \frac{4M^2 \cos^2 \theta_{\text{lab}}}{(m+M)^2} E_{m,\text{lab, CK}} \quad (3-2)$$

The $E_{m,\text{lab, CK}}$ is the laboratory energy of m using conventional kinematics geometry.

The energy of m in the center of mass, $E_{\text{c.m.}}$, is related to the detected energy of m , $E_{m,\text{lab}}$, by the following equation:

$$E_{\text{c.m.}} = \frac{m+M}{4M \cos^2 \theta_{\text{lab}}} E_{m,\text{lab}} \quad (3-3)$$

The angle and cross section in c.m. are related to those in the lab by:

$$\theta_{\text{c.m.}} = 180^\circ - 2\theta_{\text{lab}} \quad (3-4)$$

and

$$\left(\frac{d\sigma}{d\Omega} \right)_{c.m.} = \frac{1}{4\cos\theta_{lab}} \left(\frac{d\sigma}{d\Omega} \right)_{lab} \quad (3-5)$$

From Equation 3-2, one finds that the proton energies are about a factor of 4 larger in inverse geometry than in conventional geometry. This “magnifier” effect is very useful for studying low-lying resonances. For example, for protons, the detection limit with a silicon detector telescope is about 700 keV [Row98]. In the reaction $p(^{14}\text{O},p)^{14}\text{O}$, this 700 keV inverse kinematics corresponds to about 187 keV in conventional kinematics. Thus the detected low limit is lowered to 187 keV. Another advantage is obvious. Also, the resolution in the c.m. can be much better than the experimental resolution (see Equation 3-3).

The scattered light ions in typical inverse geometry cover forward angles in the lab, narrower than the angle range of 0° - 180° found in conventional kinematics. This narrower geometry focuses the light ions into a smaller cone and therefore increases the detection solid angle (see Equation 3-4 and 3-5). Due to reference frame transformation, the cross section in the lab is about 4 times that of the c.m. This is especially useful for experiments with low intensity radioactive ion beams.

Usually, inverse kinematics is used with a thick target. If the target thickness is sufficient to stop the beam, it is possible to measure the scattered light ions at 0°_{lab} , which corresponds to $180^\circ_{c.m.}$. Measurement at $180^\circ_{c.m.}$ simplifies the theoretical analysis, for example R-matrix theory analysis; in addition, the inter-

ference from the nonresonant (Coulomb and potential) scattering is minimal compared to the resonance scattering [Kra88b].

3.2.2 Thick Target

There are advantages and disadvantages to using a thick target in ER-SIKTT, which stops the beam completely. With a thick target, while the beam is gradually slowed down, a continuous range of energies can be “swept” for resonances. The thick target also shields the detectors from the direct beam for 0° measurements [Art90]. With this simple but effective set-up, many resonances can be investigated simultaneously with one bombardment. This is especially valuable for radioactive ion beams, due to their low beam intensities.

The disadvantage of targets thick enough to stop the beam is the deteriorated energy resolution due to beam projectile and product straggling (see Figure 3-4). This will be a serious problem for products near the end of the stopping range. Therefore, a thinner target may be used for more precise information on the energy and width of one state or a few states after they are surveyed by a thick target run.

Hydrogen may be prepared as a solid or a gas target while helium is only used as a gas target. Compared to a solid target, the advantages of a gas target are mainly its homogeneity and the possibility of easily modifying the target thickness by adjusting the pressure. This is convenient for changes of the beam and/or the beam energy during a run. Using a solid target simplifies the target preparation and also simplifies the solid angle calculations which are used for the final cross section determination. With a solid target, the solid angle calcula-

tion is simple since the thickness of the target ($\leq 500 \mu\text{m}$) is trivial compared with the distance between the target and the detectors.

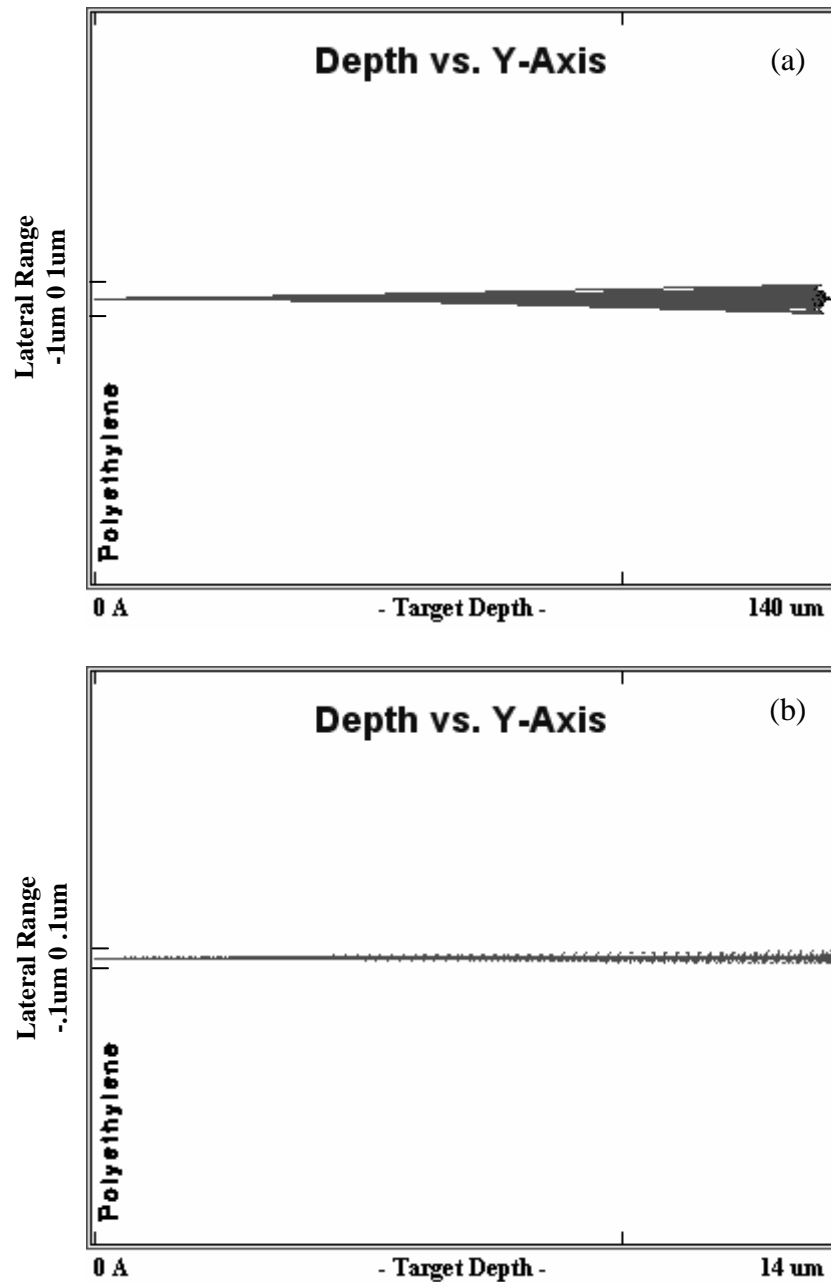


Fig. 3-4: Energy straggling of 90 MeV ^{14}O beams in polyethylene targets: a) $140 \mu\text{m}$, b)

$14 \mu\text{m}$. Calculated by SRIM 2003 [Zie03a].

With a gas target, the target thickness can be up to a few tens of centimeters, and the detector may be right behind the target. Different interaction locations, therefore, have different solid angles. (Of course, using a composite solid target, such as polyethylene for hydrogen, requires that background runs be made on the additional element.)

There are also special technical problems associated with a hydrogen target when it is used in inverse kinematics [Mar01]. Due to the technical difficulty of making a pure solid or liquid hydrogen target and the special precautions necessary to use a pure hydrogen gas target, a chemical compound containing hydrogen, for example methane gas CH_4 , is used. This again will require background measurements. Sometimes use of composite targets will increase the uncertainties and errors in the measurements, if the contribution from the carbon background is large.

3.2.3 Energy Resolution

Characteristic of all our $^{14}\text{O}+\text{p}$ experiments is a total energy resolution of about 55 keV, in the center of mass frame. Even though in these experiments the energy resolution has little effect on the final R-matrix fit, it is important to understand the most significant factors determining the resolution.

In this particular case, the main contributions to the observed resolution come from the intrinsic detector resolutions, which were about 100 keV for the 72 μm thick Si- ΔE detector and about 150 keV for the 3 mm thick Si-E detector. These two detectors were used together in all our ^{14}O runs as a 0-degree Si-telescope. The total resolution of this telescope is about 180 keV in the labora-

tory frame of reference or about 45 keV in the center of mass frame of reference.

At the 88-Inch cyclotron, the typical energy spread of a beam is about $\pm 0.5\%$. In the case of a 120 MeV ^{14}O beam this means about ± 0.6 MeV initial energy spread. While the beam is slowing down in the polyethylene $[\text{CH}_2]_n$ target, the energy spread is further increased to about 3 MeV near the end of its range in the target. For simplicity, let us now assume a narrow resonance at a certain excitation energy in ^{15}F (see Fig. 3-5). Because of the energy spread ΔE , this resonance will be excited at different depths in the polyethylene target. The importance of this depth variation to the final energy resolution of our experiment can be evaluated using Equation 3-6 [Mar00]:

$$\varepsilon \sim \frac{\Delta E}{4} \frac{z^2}{Z^2} \quad (3-6)$$

where z and Z are the proton numbers of the scattered target and projectile nucleus. In the case of ± 3 MeV energy spread of the ^{14}O , out-coming protons will have a spread of about 12 keV in the laboratory frame of reference and only about 3 keV spread in the c.m. system.

However, in the c.m. energy 1.0 to 3.5 MeV range for the detected protons, much larger contributions to the energy resolution will originate from the straggling of the protons in the polyethylene (about 23 keV), from the size of beam spot and the “size of the detectors” (10 to 30 keV).

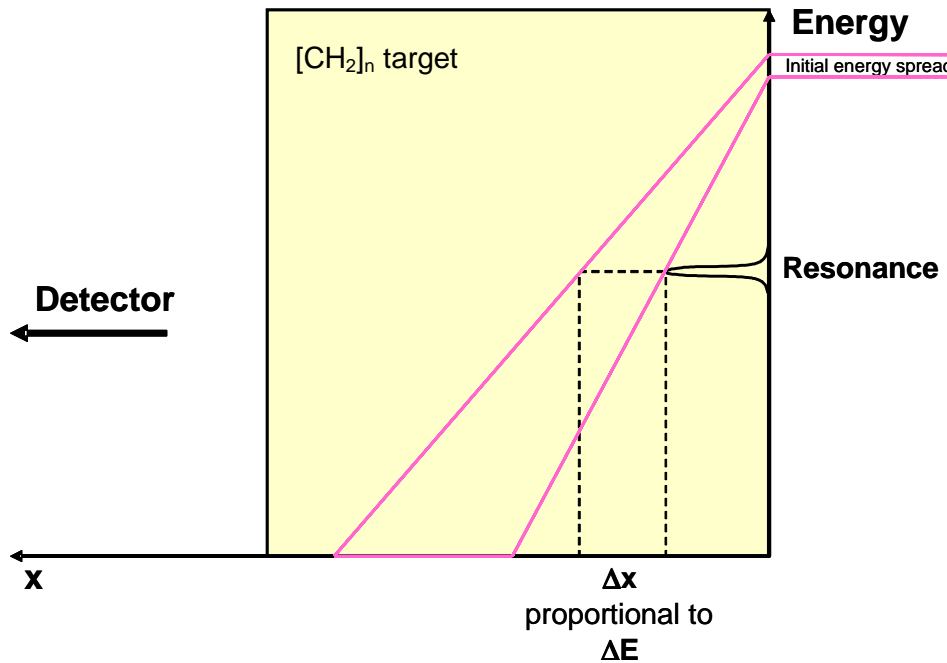


Fig. 3-5: Schematic drawing that illustrates the slowing down process of the beam in the $[\text{CH}_2]_n$ target.

Generally, the energy spread of the radioactive beam does not restrict the applicability of the method. In reality, an effective energy resolution of 30 keV in the c.m. frame is feasible by using proper experimental set-ups. At angles other than 0° lab (180° c.m.) the resolution deteriorates, mainly due to kinematical broadening of the energy for protons scattered at different angles.

3.2.4 Inelastic Scattering Competing Reactions

There is an assumption underlying the ERSIKTT technique that the elastic cross section at a resonance is the dominating contributor above all other processes. Often the only other candidate that must be considered is the inelastic resonance scattering. The inelastic scattering probability is strongly related

to the level structure of the nuclei involved. Level structure is important, since in inelastic scattering, part of the kinetic energy is converted into internal excitation. The 120 MeV $^{14}\text{O} + \text{p}$ reaction is relatively simple in this sense since the proton does not have excited states and the first excited state in ^{14}O lies quite high, at 5.17 MeV (see Fig. 3-6). In the $^{14}\text{O} + \text{p}$ runs (see Chapter 6), the beam was degraded to about 84.5 MeV before it entered the thick polyethylene target. With such a beam, one is able to probe states in ^{15}F up to about 4.15 MeV. As shown in Fig. 3-6, even theoretically under these conditions there is only a very small energy window for possible inelastic scattering. For the ground- and the first-excited-state-resonances in ^{15}F , elastic scattering is obviously the only open channel.

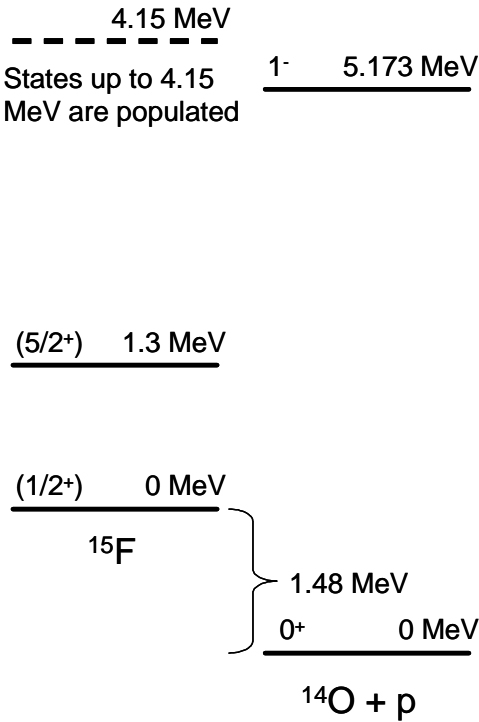


Fig. 3-6: Level structure in ^{15}F .

3.2.5 Cross section

It is easier to extract cross sections from thin target experiments than from thick target experiments [Rol88]. The main additional complication in thick target experiments, such as the one discussed above, arises from the fact that the beam is stopped inside the target. As is well known, in such a process one cannot assume a constant stopping power for the beam. In other words, during the slowing down process a beam particle will “see” different amounts of target nuclei at different energies. Therefore, to relate the observed yield of protons to a relative cross section versus energy, one must correct for the changing energy loss of the bombarding ion as it slows down. The energy loss rate effectively determines the distance the ion travels in the target while in a specified energy interval, and thus the effective areal density of target protons. Thus, observed yields must be multiplied by a function related to the beam ion energy loss to calculate the elastic scattering excitation function:

$$\sigma \propto Y \times dE/dx \quad (3-7)$$

3.2.6 Applicability of ERSIKTT to Radioactive Ion Beams

In summary, the ERSIKTT method is a powerful tool for the studies of low to medium energy resonances in exotic nuclei. The low intensities of radioactive ion beams are counteracted by the large cross sections characteristic of elastic scattering, the forwardly focused scattered protons and the scanning of the whole energy region by every beam particle due to the thick target. The target thickness also allows for measurement at 0°_{lab} ($180^\circ_{\text{c.m.}}$), where other scat-

tering amplitudes have their minima. In this approach, the rather large energy spread of radioactive ion beams does not seriously deteriorate the energy resolution. The inverse kinematics makes the proton energies larger than in conventional measurements, and the transformation from the lab to the c.m. improves the resolution. A further benefit is that the theory of elastic scattering has been in use for half a century and is well understood.

There are also some obvious problems related to this technique. One of them is of course the difficulty of producing the needed radioactive ion beams (RIB). This technical problem will be at least partly solved with the second generation RIB facilities like the Rare Isotope Accelerator (RIA) in the USA. Another obstacle may be the more difficult interpretation of the data, especially when both the spin of the projectile and that of the target are non-zero.

3.3 Radiation Detection

3.3.1 Radiation Detectors

Only conventional surface barrier silicon detectors (with thickness less than 1000 μm) and Si(Li) detectors (3-5mm) were used in this thesis. A so called Si-telescope constructed from such detectors makes particle identification possible. The different detector configurations used in this work are discussed in Chapters 4-6. Detailed operating principles for silicon detectors can be found in the literature [Kno79, Tso83]. Therefore, only the most important specific features relevant to this thesis are discussed in the following.

3.3.2 Particle-Identification Telescopes

One way to distinguish between protons, alphas and other heavier particles is to rely on the difference between their stopping powers. The stopping power dE/dx [Ber93] for ions varies as:

$$-\frac{dE}{dx} = \frac{4\pi \cdot \rho \cdot r_e^2 \cdot m_e c^2}{\beta^2} \frac{1}{u A} Z z^2 L(\beta^2) \propto \frac{M z^2}{E} \quad (3-8)$$

where ρ is the density of the stopping material (for example Si); r_e and m_e are the classical electron radius and mass; β is the velocity of the incident ion relative to the speed of light; u is the atomic mass unit; Z and A are the atomic number and mass number of the stopping material; z , M and E are the charge, mass and energy of the incident ion, respectively. The quantity $L(\beta^2)$ is called the stopping number; it takes into account fine details of the energy loss process and depends on specific properties of the stopping medium. Equation 3-8 does not hold for incident ions at low energy (~ 250 keV for protons, ~ 1 MeV for alpha particles, depending on the medium). As the ion velocity approaches the velocity of the atomic electrons, the ions will begin to capture electrons from the stopping medium; this will cause the stopping power to decrease with decreasing energy. Figure 3-7 shows stopping power curves for protons and alpha particles in silicon.

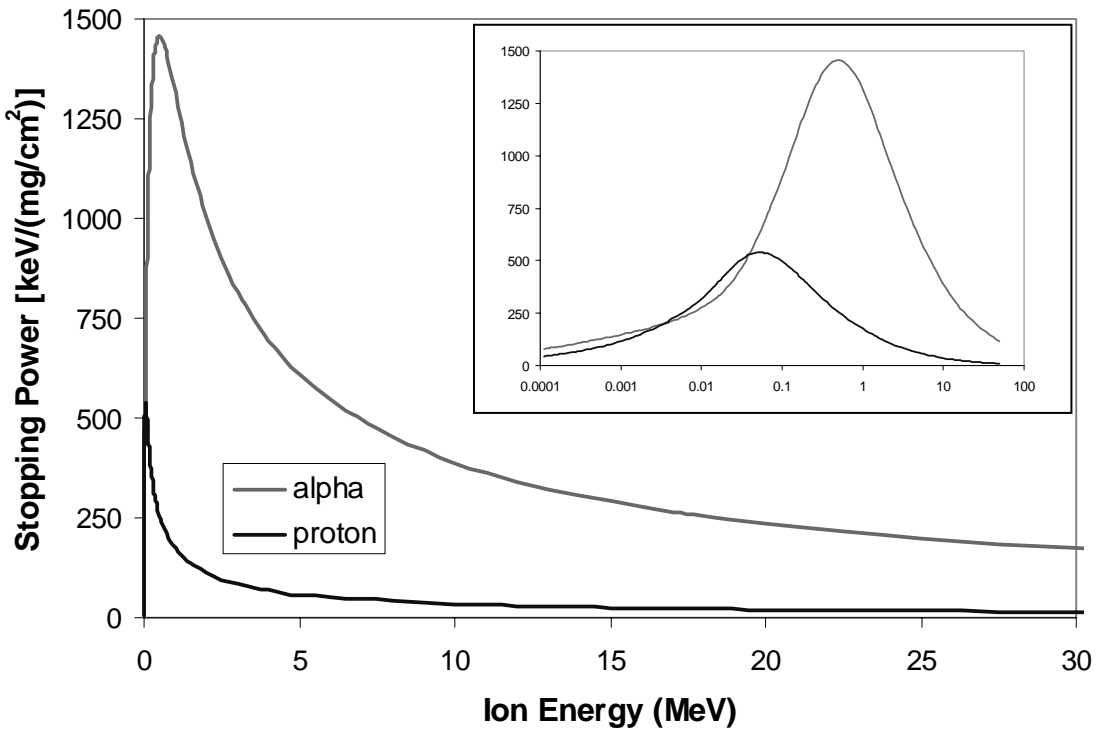


Fig. 3-7: Stopping power curves for protons and alphas in silicon, from the SRIM calculations [Zie03a].

The dependence of the stopping power on the charge, mass and energy of the incident ion can be used for identification. A popular method based on this idea is the use of particle-identification (PI) telescopes, which are usually composed of a thin “ ΔE ” detector and a thick “ E ” detector [Gou75]. The thin “ ΔE ” detector measures the differential energy loss. After the ΔE detector, the ions are fully stopped in the following “ E ” detector; the telescope allows measurement of the total energy. Using results of Equation 3-8, it has been found

empirically that the ΔE and E detector signals may be combined according to the equation:

$$PI = (E + \Delta E)^{1.73} - E^{1.73} \propto Mz^2 \quad (3-9)$$

to produce a particle identifier signal that is proportional to the mass M and the charge squared z^2 of the ion; light ions (e.g., p , α , etc.) will produce different peaks in this spectrum. By gating on these peaks, either in hardware or software, a separation of events based on the charge and mass of the species detected may be achieved.

3.3.3 Counting Electronics

Figure 3-8 depicts a typical electronics configuration for the ΔE - E telescope used in this work. The counting electronics may be divided into two categories according to function: the energy determination and the event discrimination. This separation does not take place immediately. In both cases, the preamplifiers first integrate and amplify the charge collected by the detectors. The collected charge will be proportional to the energy lost by the ion in the active region of the detector. To reduce the noise, the preamplifiers are located as close to the detectors as possible. Preamplifier signals are then fed into the main amplifier, which has both slow (1 μ sec) and fast (0.2 μ sec) outputs. The energy/slow output is directed into an analog-to-digital converter (ADC) while the 'fast' output goes to a constant fraction discriminator (CFD). In the CFD, the fast pulse is reshaped into a nuclear instrument module (NIM) format and en-

ergy thresholds are set at the same time. Output pulses from a NIM are sent to a gate and delay unit and then to a logical AND unit. Such a unit generates a NIM output only in the case when incoming signals from the ΔE and E detectors have a time overlap of at least 100 ns. The output from the logical AND unit goes to a master gate unit and to an overall control box for the CAMAC.VME data acquisition system.

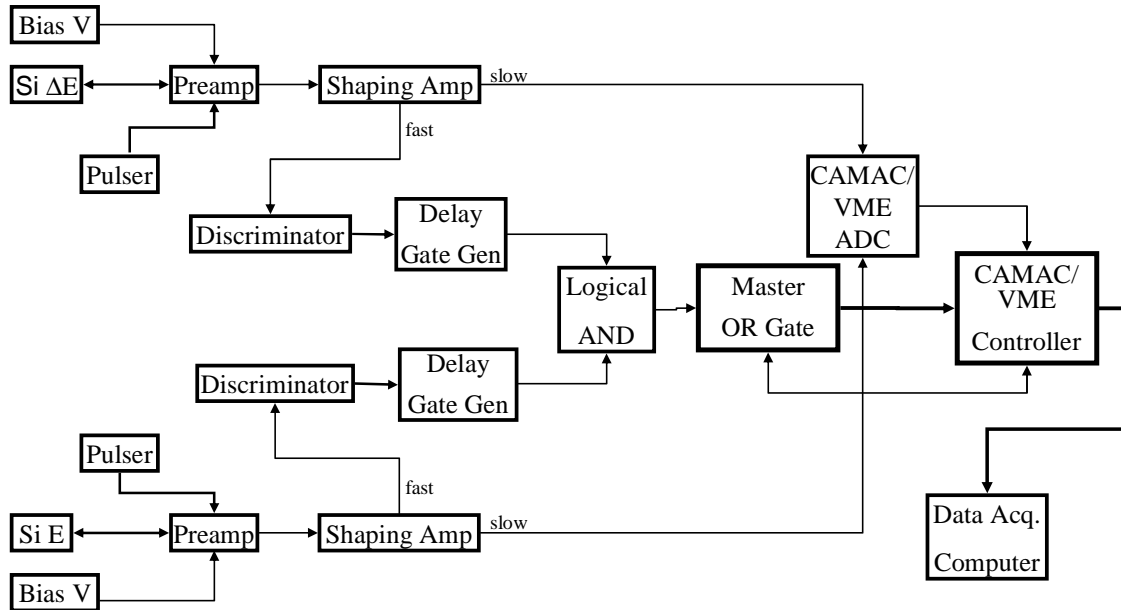


Fig. 3-8: Generalized counting electronics. See text for an explanation of abbreviations and functions of individual modules.

When the CAMAC/VME controller registers an appropriate signal, it triggers the ADC modules to read all of their inputs and also triggers the crate controller, in either CAMAC or VME type, to read the ADC's. When the memory of

the controller module is full, its contents are dumped to the data acquisition computer, where events are stored.

As mentioned earlier, the ADC's read the slow outputs of the shaping amplifiers. Silicon detectors have a rapid charge collection and therefore one μ s shaping times in amplifiers are usually sufficient. The ADC's are peak sensitive, producing a digitized signal proportional to the pulse amplitude. The width of the master gate that triggers the read operation must be matched to the longest shaping time in use to ensure that the maximum amplitudes are recorded.

The relationship between the energy lost in the detectors and the signal measured by the ADC's may not be precisely linear [Row98]. Though this non-linearity of the slow-signal electronics is not large, in many cases it must be accounted for in order to obtain a reliable energy calibration. This is especially true when it is necessary to extrapolate to a region outside of the available calibration range. The typical integral non-linearity was $\sim 0.3\%$ for most regions of the experimental spectrum [Row97, Row98].

In our experiments the singles count rate of the silicon detectors was typically limited to about 40 kHz in order to keep the number of random coincidences between the E and the ΔE detector at a statistically-low level.

3.4 Data Analysis

3.4.1 Data Reduction in Software

The data are stored in the so called event mode. Such a data format permits off-line analysis including ΔE - E matrix presentations of the coincidence data and corresponding multidimensional gating. Two-dimensional gating of the ΔE - E matrix can be used efficiently to separate the different exit channels from one another. The data acquisition and analysis codes used in this work are: CHAOS [Rat91], Kmax [Elf97, Spa04, Bak92, Pie91], and SpecTcl [Fox96, Fox03].

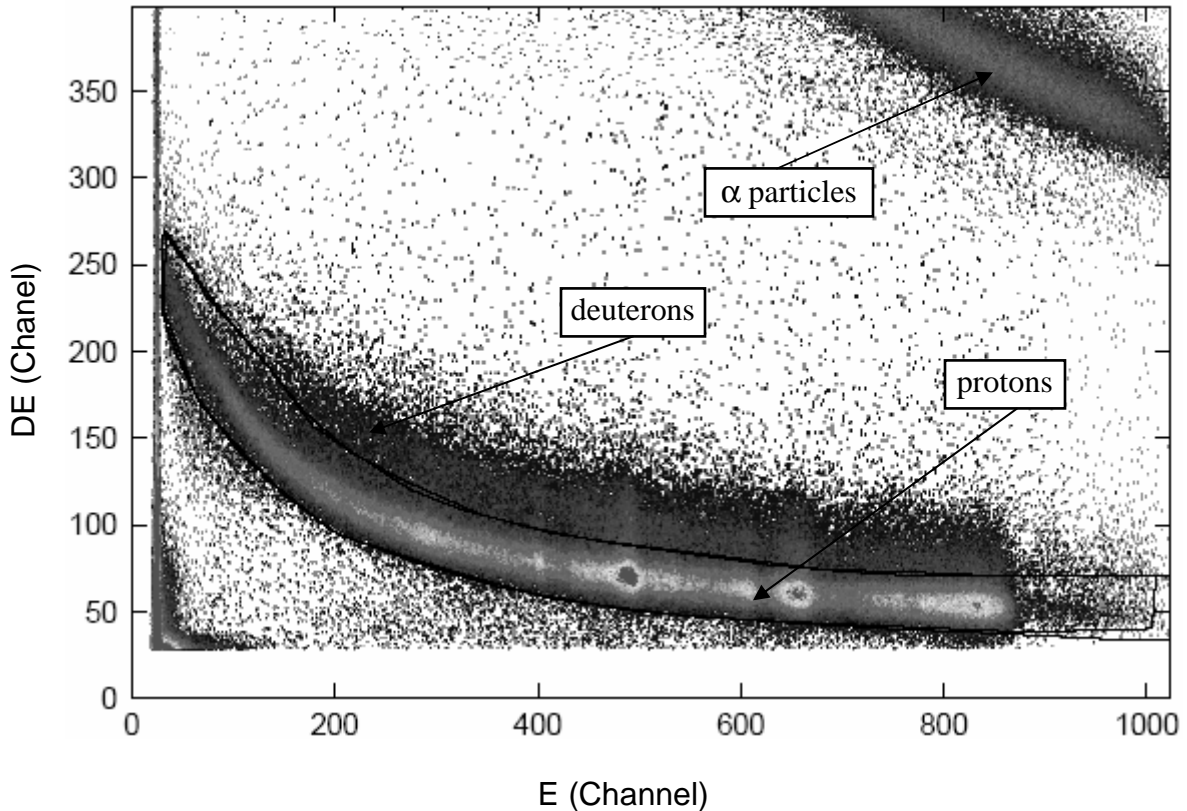


Fig. 3-9: An example of 2D-gating process: $^{14}\text{N} + \text{p} \rightarrow ^{15}\text{O}$.

When the data are displayed in the Si- ΔE vs. Si- E projections, one can usually separate the light ion species of interest. Sometimes overlap occurs at low energies due to effects related to the resolution of the detectors, and more importantly, to energy-loss straggling in the ΔE detector.

Figure 3-9 illustrates the two-dimensional gating of the ΔE - E spectra. The reaction studied was 120 MeV ^{14}N on a $[\text{CH}_2]_n$ target and the gate is drawn around the detected protons. As can be seen, the alpha particle reaction channel is also open in this reaction.

3.4.2 Calibration of Detector Systems

In our $^{14}\text{O}+\text{p}$ experiments, the calibration of the Si-detectors was mainly based on the proton spectrum from the $\text{p}(^{14}\text{N},\text{p})^{14}\text{N}$ reaction. This will be discussed in detail later in chapter 6. In addition, standard α sources (e.g., ^{153}Gd , 3.182 MeV; ^{241}Am , 5.486 MeV) and a precision pulse generator were used. To optimize the accuracy of the measurements, we always tried to calibrate with the ^{14}N beam before and after the main ^{14}O run.

The ^{14}N calibrations are accurate to about 15 keV in the center of the mass frame over the entire energy range of 1 to 5 MeV. However, a significant correction is required to use this calibration with $^{14}\text{O}+\text{p}$. The higher energy loss of ^{14}O in the degrader foil and target lead to interactions occurring at a shallower depth in the target, relative to the equivalent scattering by ^{14}N . Thus, protons scattered by ^{14}O have lost more energy as they emerge from the back of

the target. The calculated energy loss corrections for ^{14}O and ^{14}N beams are shown in chapter 6.

C H A P T E R 4

BEARS: PRODUCTION OF RADIOACTIVE ION BEAMS OF ^{11}C AND ^{14}O

4.1 Introduction

For many years, the Lawrence Berkeley National Laboratory (the Lab) has been one of the leaders in the research, development, and application of radioactive ion beams. The first re-acceleration of radioactive nuclides was done in 1970 with experimenters from what was then called the Lawrence Radiation Laboratory [Che70]. Fission fragments spontaneously produced by ^{252}Cf were accelerated to energies of ~ 200 MeV using a model MP Van de Graaff accelerator at the High Voltage Engineering Corporation in Burlington, Massachusetts. While the purpose of this work was to investigate new methods of producing heavy ion ($>\text{Ar}$) beams for the study of super heavy nuclei, it is one of the earliest works on radioactive ion beams.

Following another approach, projectile fragmentation experiments were first tested in 1971 by Heckman *et al.* in the Lab [Hec71, Hec72]. These ex-

periments were carried out at the Bevatron on the nuclear fragmentation of nitrogen-14 ions at an energy of 2.1 GeV per nucleon on carbon and hydrogen targets. This effort was continued in the 1980's by Tanihata *et al.* [Tan85a, Tan85b]. Experiments measuring the interaction cross sections and nuclear radii of exotic He, Li, and Be nuclides were performed with radioactive ion beams from the Bevalac at the Lab.

In the meantime, different radioactive ion beam facilities were intensively discussed in the Lab by many authors [Alo84, Alo89, Cla90, Fei90, Kre87, Kre91, Mye90, Nit84, Nit88, Nit89, Nit90a, Nit90b, Nit92, Nit93, Nit94]. Among them, Nitschke was one of the strong advocates for an ISOL-type radioactive ion beam facility in North America.

Since the Bevalac and SuperHILAC involved in the radioactive ion beam research at the Lab were shut down at the beginning of the nineties, these efforts have been continued by experimenters at the 88-Inch Cyclotron. After a small Biomedical Isotope Facility (BIF) cyclotron was installed in the Lab [Van97], the idea of coupling the BIF cyclotron with the 88-inch cyclotron was proposed: this became Berkeley Experiments with Accelerated Radioactive Species (BEARS) [Cer96].

The basic BEARS system involves isotope production in a N_2 gas target at the BIF low-energy proton cyclotron, transport as CO_2 via a 350-m-long capillary to the 88-Inch Cyclotron, cryogenic separation of the activity from the target and carrier gases, and injection into the 88-Inch Cyclotron's advanced electron-cyclotron resonance ion source for ionization and subsequent acceleration

[Cer99, Pow00, Pow03]. We have initially focused on the production of ^{11}C ($t_{1/2}=20$ min) and ^{14}O ($t_{1/2}=71$ s), both produced from a nitrogen gas target. The maximum thick-target production yields are approximately 1×10^{11} atoms/s of ^{11}C and 5×10^9 atoms/s of ^{14}O [Pow03]. Finally, two beams have been used for experiments: ^{11}C with an intensity up to 2×10^8 ions per second on target [Joo00, Pow00] and ^{14}O with an intensity of up to 3×10^4 ions per second on target [Guo03, Guo04].

4.2 Test Experiments

4.2.1 Tests with Mimicking BIF at the 88-Inch Cyclotron

Prior to the construction of a radioactive isotope activity transfer line between the two accelerators, tests were carried out entirely at the 88-Inch Cyclotron, which was used to mimic the BIF Cyclotron, producing up to $10\ \mu\text{A}$ of 10 MeV protons. These proton beams were directed into the target chamber of a nitrogen gas-jet transport system. ^{11}C and ^{14}O were produced via (p,n) and (p,α) direct reactions on the nitrogen, which acted as the target and carrier gas. The ^{11}C and ^{14}O were then sent to ECR ion sources for ionization and further acceleration (Figure 4-1).

The ECR ion sources, particularly the upgraded Advanced ECR source (AECR-U) [Xie98], can reliably achieve good ionization efficiencies at high-charge states with a vacuum of less than 10^{-6} Torr. Therefore, a central technical challenge of BEARS was the coupling of the isotope production system to

an ECR ion source. Two methods were tried for coupling the isotope production system to the ECR ion source systems. One was a skimming method [Mol97] and the other was a cryo-trapping method [Pow98].

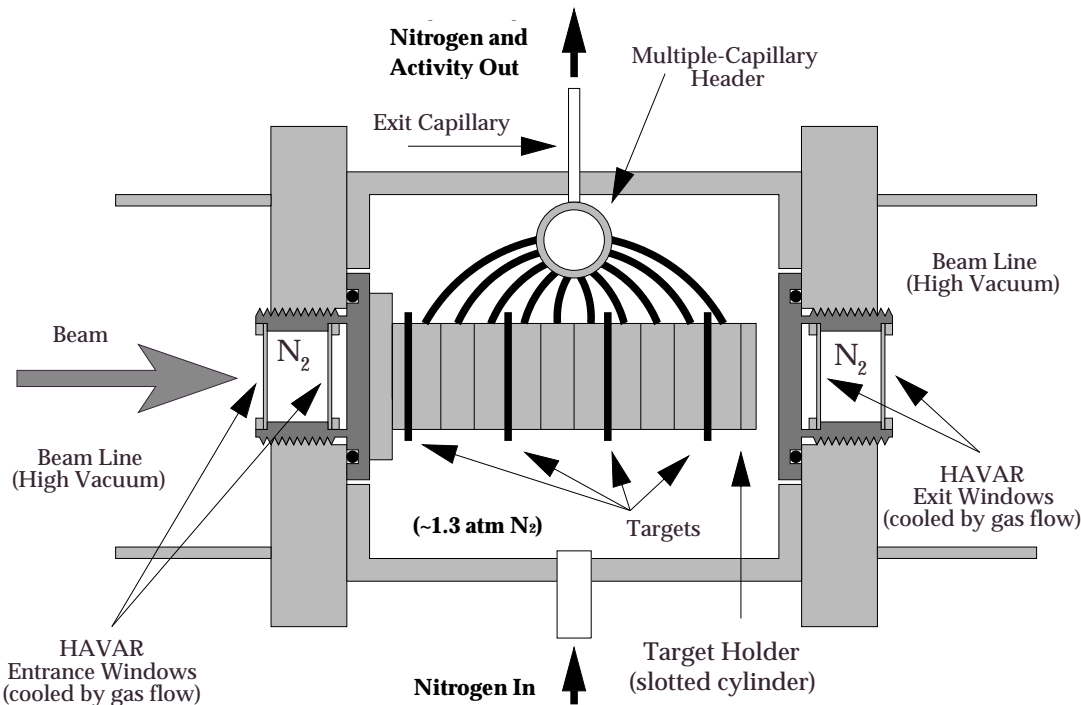


Fig. 4-1: Nitrogen gas-cell target system [Row98].

First, the skimming method was tried. Since the gas-jet system required a pressure of one or two atmospheres, a highly effective gas-skimming system was constructed and coupled directly to the ECR, with four differentially pumped skimming stages (see Figure 4-2). Aerosol clusters (made from ethylene glycol) containing the radionuclides of interest and carrier gas entered the first stage in a jet at near-sonic velocity. The heavier clusters exited in a narrower cone than the expanding gas, allowing them to pass through the small

holes in the three successive skimmers. Once inside the ECR, the aerosols were caught on heated surfaces, which vaporized the activity. Tests showed that the gas pressure could be sufficiently reduced so that, with a full target gas load, the ECR performance was not significantly degraded.

Unfortunately, it was found that this system failed to transport significant amounts of ^{11}C or ^{14}O . This was traced to the majority of the activity forming gaseous compounds and thus not attaching to the aerosol clusters. The amount of ^{11}C in a chemical form that could be transported was only on the order of 0.1-0.5%. Nevertheless, a beam of ^{11}C was extracted and detected, although at very low intensity.

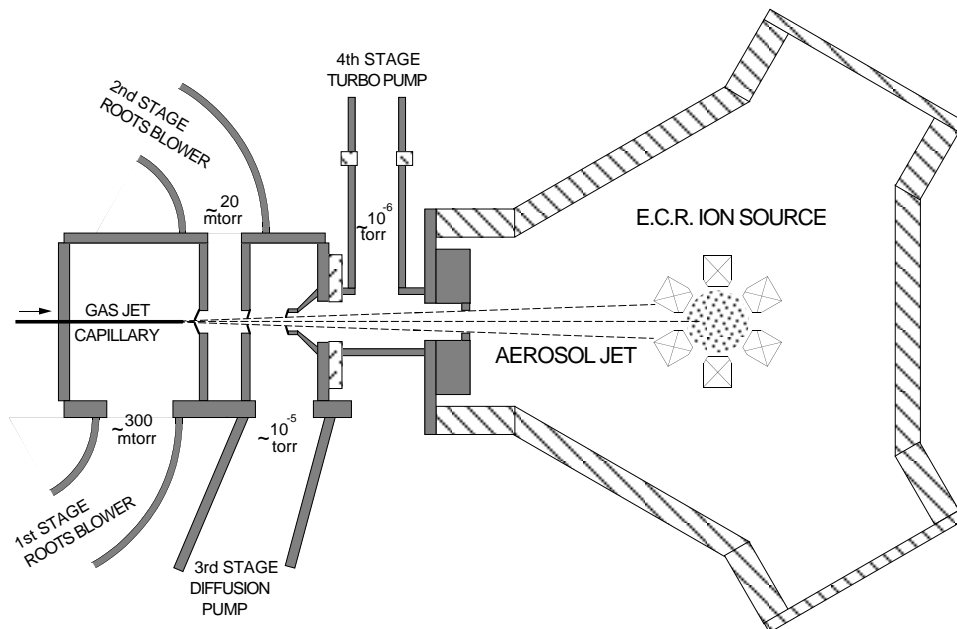


Fig. 4-2: A four component, differentially pumped skimming system for injecting aerosols into the ECR ion source.

In the second approach, the cryo-trapping method, the N_2 target gas flowed continuously from the target region through a plastic capillary of 3-mm inner diameter (i.d.), to an area next to the ion source, where it passed through a cryogenic trap consisting of a stainless-steel coil submerged in liquid nitrogen. A pump at the outlet kept the pressure in the coil well below 1 atm, preventing the condensation of the nitrogen gas, but allowing the trapping of such gases as CO_2 , N_2O , etc. (Fig. 4-3a). After stopping the flow of target gas and pumping away the residual nitrogen, the liquid nitrogen surrounding the trap was replaced with a dry ice and alcohol bath, raising the temperature enough to release gases such as CO_2 while keeping any water contamination frozen (Figure 4-3b). The gas was slowly passed into the ion source through an adjustable valve, at a rate low enough to prevent overloading of the source. Beams of ^{11}C and ^{14}O in various charge states were extracted from the ECR source, and their yields were measured by selecting these beams using an analyzing magnet and then measuring the build-up and decay of radioactivity in a Faraday cup. For each test the ion source was first tuned for the same charge state as a corresponding stable isotope.

Both ^{11}C and ^{14}O were successfully trapped and released, in quantities of about a third of those estimated from the known production yields [Kit90]. Beams of several different charge states were extracted from the ion sources. A summary of the measured ionization efficiencies is given in Table 1, along with similar results for stable carbon and oxygen, taken with a calibrated CO leak under carefully tuned conditions. The AECR-U was found to have good efficien-

cies for the radioactive isotopes, with a maximum of 11% for $^{11}\text{C}^{4+}$ and 3.6% for $^{14}\text{O}^{6+}$. These numbers are lower than the measured stable-isotope efficiencies, possibly because of the relatively high gas load coming from the trap [Xie99].

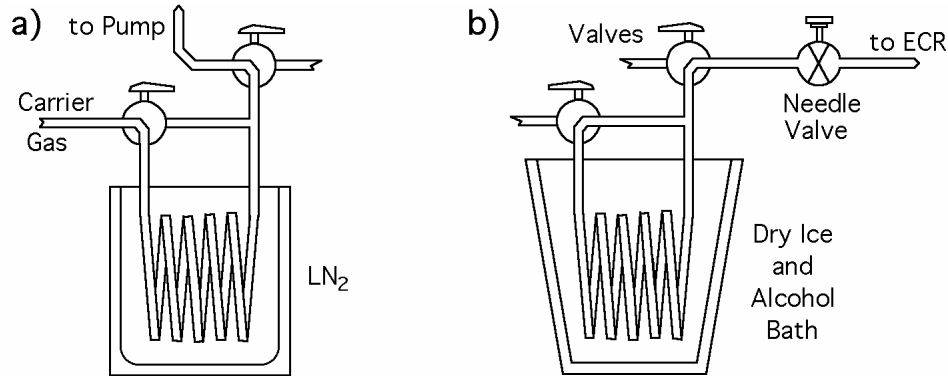


Fig. 4-3: Cryogenic trapping system: (a) trapping and (b) release at dry ice temperatures into the ECR ion source.

Table 4-1: Ionization efficiencies and hold-up times of the 88-Inch Cyclotron's ECR ion sources

Ion	ECR			Ion	AECR-U with stable CO leak (^{12}C and ^{16}O)	
	%	%	τ_{fast} (sec)		%	τ_{fast} (sec)
$^{11}\text{C}^{1+}$	1.1					
$^{11}\text{C}^{2+}$	0.7					
$^{11}\text{C}^{3+}$	0.4	4				
$^{11}\text{C}^{4+}$	0.9	11	24	$^{12}\text{C}^{4+}$	24	5.6
$^{11}\text{C}^{5+}$	0.1	4		$^{12}\text{C}^{5+}$	14	
$^{11}\text{C}^{6+}$		2				
$^{14}\text{O}^{3+}$	0.4					
$^{14}\text{O}^{4+}$	0.4					
$^{14}\text{O}^{5+}$	0.4			$^{16}\text{O}^{5+}$	12.5	
$^{14}\text{O}^{6+}$		3.6		$^{16}\text{O}^{6+}$	27	7.1
$^{14}\text{O}^{7+}$		1.2	20-30	$^{16}\text{O}^{7+}$	6	
$^{14}\text{O}^{8+}$		0.4				

It is important for efficient RIB production that the time the radioactive species spends in the source, the “hold-up” time, should be short in comparison to its lifetime. Source hold-up times in the AEGR-U have been measured for stable CO and found to be of the order of 5-7 sec (Table 4-1). When the decay of the activity is measured for ^{11}C and ^{14}O , two components are seen in the decay curve. The fast component is on the order of 20-30 sec for both species, which is associated with the holdup time of ions in the plasma. The slow component is on the order of 360 sec for ^{11}C , which is associated with sticking of the plasma-dissociated components of CO to the ion-source plasma-chamber walls. If one could shorten the hold-up times in the source for ^{11}C and ^{14}O to be nearer to that of stable carbon and oxygen, the ionization efficiencies should approach those of the stable species. This is particularly important for the 71 sec ^{14}O , for which nearly an order of magnitude improvement could be made.

4.2.2 Batch Mode Coupling of BIF to the 88-Inch Cyclotron

In parallel with construction of the transfer line between the two accelerators, development of accelerated ^{11}C beams continued. During a second series of tests, now using BIF, ^{11}C was produced as CO_2 and cryogenically separated from other gases. It was then transported by truck to the 88-Inch Cyclotron in a lead-lined Dewar, where it was injected into the AEGR-U and ionized. Each batch of ^{11}C was produced for a period of about 50 min, separated and transported in 15 min, and injected into the source over a period of 15 to 30 min. It was during these batch tests that a ^{11}C beam was first accelerated using the 88-Inch Cyclotron.

Due to the low intensity of radioactive beams, it was necessary to tune the cyclotron optics with stable analogue beams. A scattering foil and a particle identification telescope were used to analyze the accelerated beam after extraction from the cyclotron (Fig. 4-4). The cyclotron was initially tuned on $^{22}\text{Ne}^{8+}$, then the cyclotron frequency was adjusted to accelerate the trace amounts of residual $^{11}\text{B}^{4+}$ always present in the ion source (see Figure 4-4a). The ^{11}C was introduced; however, cyclotron frequencies for ^{11}B and ^{11}C , with a separation of only 1.4 kHz, make them unresolvable (see Fig. 4-6b). The measured ^{11}C beam intensity was 0.5 to 1×10^8 ions/s, which was maintained over a period of about 20 min.

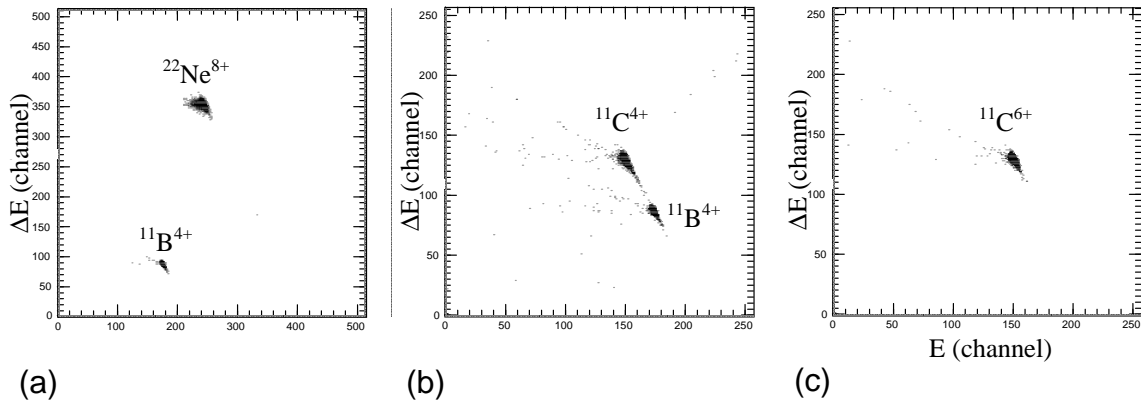


Fig. 4-4: Particle Identification of (a) $^{22}\text{Ne}^{8+}$ and $^{11}\text{B}^{4+}$, (b) $^{11}\text{C}^{4+}$ and $^{11}\text{B}^{4+}$, and (c) $^{11}\text{C}^{6+}$.

The ^{11}B to ^{11}C beam ratio was about 1% during the initial test, but increased by more than three orders of magnitude in a later experiment when the AECR-U had been contaminated with boron. However, the boron component of

the beam could be eliminated easily by stripping the beam after acceleration and magnetically separating fully stripped $^{11}\text{C}^{6+}$ from $^{11}\text{B}^{5+}$ (Figure 4-4c).

4.2.3 Transfer-Line Mode for Coupling BIF to the 88-Inch Cyclotron

Figure 4-6 shows the 350 m long capillary transfer-line coupling the two accelerators. A short gas-transport time is required, both to reduce decay losses suffered by short-lived isotopes like 71-s ^{14}O , and to minimize radiation levels during transit and outside the two accelerator buildings. Tests were carried out, without radioactivity, by using bursts of helium gas in a flow of nitrogen gas. The differing response of a thermal-convection vacuum gauge to helium and nitrogen allowed timing measurements to be made. It was found that the fastest transport times could be achieved by pre-evacuating the transport capillary for a few minutes before applying pressurized gas. For these tests, a volume of helium, comparable to the amount needed to fill the BIF gas target, injected in front of the driving nitrogen, traveled the 350 m distance in 12–30 s. The exact time depended on the capillary size, the drive-gas pressure, and the degree to which the capillary was pre-evacuated. The regime investigated spanned 2–4 mm inner capillary diameters, 1–8 atm pressure, and 1 to 5 min pump-out. Capillary evacuation could be improved by supplying drive gas for only a short time, approximately 10 s. Longer drive times did not result in noticeably faster transport.

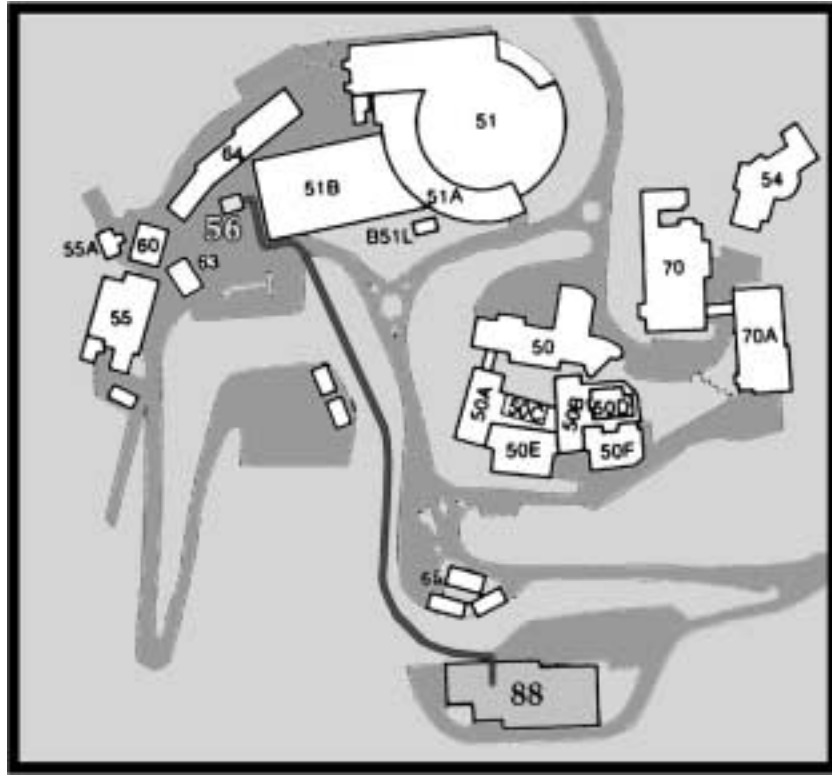


Fig. 4-5: The transfer-line connecting the BIF (Building 56) and the 88-Inch Cyclotron (Building 88).

4.3 Final BEARS Configuration

The final BEARS configuration has been described in detail by Powell *et al.* [Pow00]. BEARS is a highly automated system. In addition, radiation control and safety systems are installed to protect personnel and the public. The following sections describe the entire BEARS system along with its typical operation for the production of ^{11}C beams. The same system is used for ^{14}O beams with significant modification only in the production of the $\text{C}^{16}\text{O}^{14}\text{O}$.

4.3.1 Target System at BIF

Figure 4-6 shows the BIF gas–target system [Van97]. The target, 80 mm deep and 13 ml in volume, is filled through valve V1 to 22 atm with the nitrogen target gas. The gas is then bombarded for 5 min with 10 MeV protons, typically with intensities of $\sim 30 \mu\text{A}$. During bombardment, the pressure in the water-cooled target increases to 50 atm due to beam heating. After 5 min, the beam is shut off, and the irradiated gas is unloaded through valve V2 into a "holding tank" where the gas is held prior to transport. After unloading, the target is re-filled and the cycle is repeated.

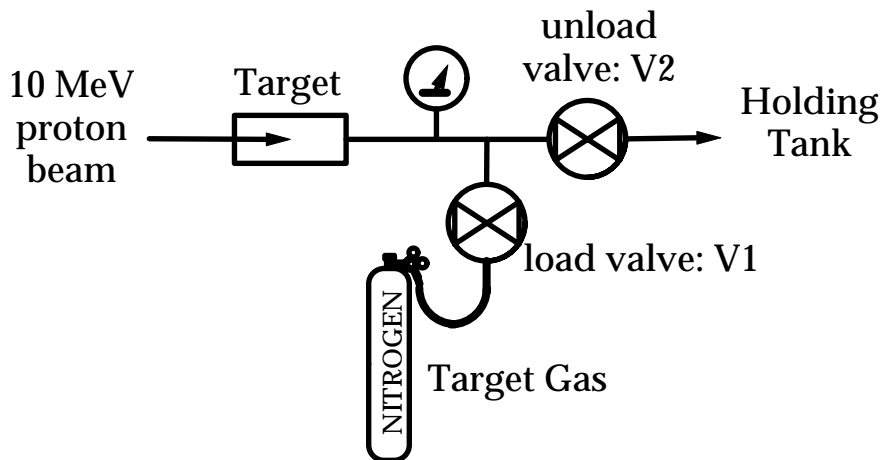


Fig. 4-6: Target system for activity production at the Biomedical Isotope Facility.

In order to be transported and cryogenically separated by the rest of the BEARS system, the ^{11}C activity must take the chemical form of CO_2 . By controlling an exact fraction of oxygen introduced into the nitrogen target gas, a balance was found with both a good $^{11}\text{CO}_2$ yield and a gas load low enough for good AEGR-U ion source operation. An additional load valve and gas supply were added to the gas–target system shown in Figure 4-6; the target was first

partially loaded with 1% O₂ plus 99% N₂ to 4.4 atm, then topped off to 22 atm with pure nitrogen. The optimum oxygen fraction was found to be around 0.2%.

4.3.2 Transport

Figure 4-7 illustrates the components of the transport system, which carries the activity from the BIF facility to the 88-Inch cyclotron. While the BIF cyclotron is preparing a 5-min batch of ¹¹C, the transport capillary (polypropylene; 3.0-mm i.d.) is evacuated from both ends, both through valve V7 at the 88-Inch Cyclotron, and through valve V6 at BIF. The holding tank (a 3 m length of 4.5-mm i.d. tubing) is also evacuated at the same time (valves V4 and V6 open, V2 and V3 closed). Valve V4 is closed just before the target is unloaded through V2 and the activated target gas is held in the holding tank for 1 to 2 min to allow some of the ¹⁴O, not needed during ¹¹C operation, to decay. To transport the gas, 6 atm of nitrogen is applied through valve V3, driving the target gas down the evacuated transport capillary (V2 and V6 closed; V3 and V4 open). The drive gas (V3) is shut off after about 10 s, and the pump-out valve (V6) is opened soon after. The approximately 3 min of pumping serves to reduce the pressure in the holding tank to less than 0.2 atm before it is valved off for the next target-unload cycle. Transport between the two buildings takes 20–23 s. All the activity arrives at the 88-Inch Cyclotron within a spike of about 2 s, indicating a lack of mixing with the drive gas.

During most of the 5 min cycle, the downstream end of the transport capillary is connected directly to the high-capacity pump through the three-way valve V7. Simultaneously, the cryogenic trap, a stainless-steel coil submerged

in liquid nitrogen, is being maintained at vacuum by a second "low-pressure" pump. For about a 10 s period, centered on the expected arrival time of the transported activity, the gas flow is diverted through the trap via valves V7–V10 and then to the high-capacity pump. After the activity arrives, the flow is redirected to the high-capacity pump, and the remaining nitrogen gas in the trap is removed by the low-pressure pump through valves V9 and V10.

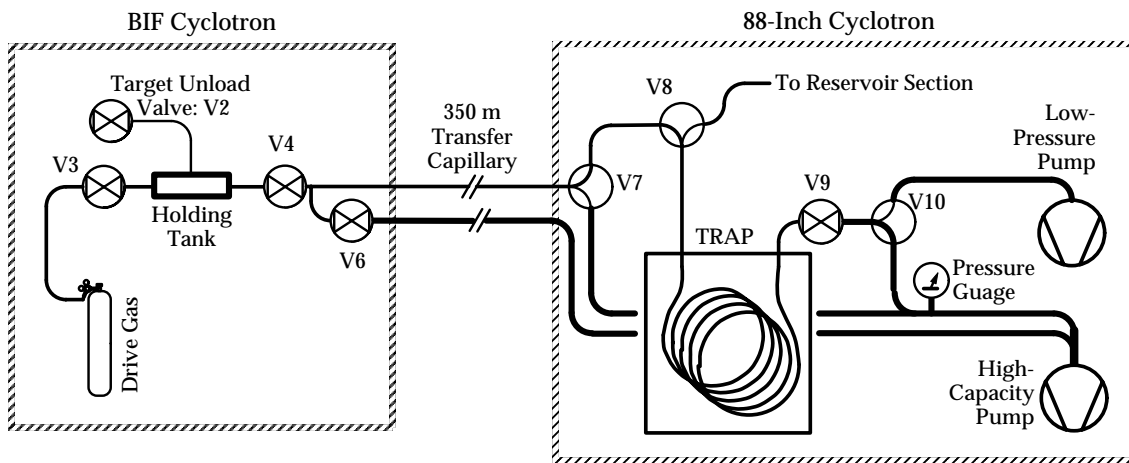


Fig. 4-7: System for transporting activity between the two accelerator buildings. Valves are indicated by V2–V10.

Figure 4-8 presents, for a typical transfer, the pressure at the capillary outlet as measured after the trap (this gauge is marked in Figure 4-7), and the activity measured in the cryogenic trap by a radiation detector.

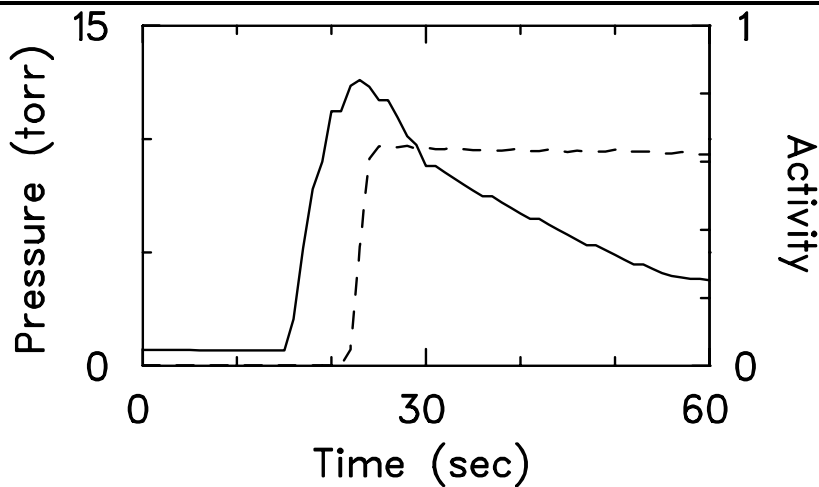


Fig. 4-8: Capillary-outlet pressure (solid line) and activity observed in the cryogenic trap (dashed line; arbitrary units) during a typical transfer between the two accelerator buildings. Transport was started (V4 opened) at $t=0$.

4.3.3 Cryogenic System

Before being injected into the AEGR-U ion source, the ^{11}C activity must be released from the cryogenic trap by heating. The trap itself consists of a small coil of thin-walled (0.4 mm), 4-mm i.d. stainless-steel tubing. The entire coil is enclosed within a 5-cm vertical tube of low heat-capacity foam insulation. This open-bottomed tube is partially submerged in a liquid-nitrogen bath such that the liquid level completely covers the trap coil. To warm the trap, pressurized room-temperature dry nitrogen is applied to the outer tube, displacing the liquid nitrogen and bubbling out through the bottom of the tube. The flow of gas past the trap coil causes it to warm. A thermocouple, fixed inside a separate section of identical steel tubing, monitors the temperature. With the thin-walled

steel tubing currently used, the trap can be warmed from 77 to 220 K in about 20 seconds.

4.3.4 Ion Source Injection

Figure 4-9 shows a schematic diagram of the BEARS system from the cryogenic trap to the ion source. After most of the nitrogen drive gas has been pumped away through valve V9, warming of the trap is begun. When the temperature of the trap reaches \sim 120 K, pumping is ceased (V9 closed) and the trap is connected to a "reservoir" section through three-way valve V8. The reservoir is located as close to the ion source as possible, about 3 m from the trap. The reservoir itself is of small volume, formed mostly by the 40 cm^3 internal volume of the thermal convection gauge tube used to monitor the gas pressure.

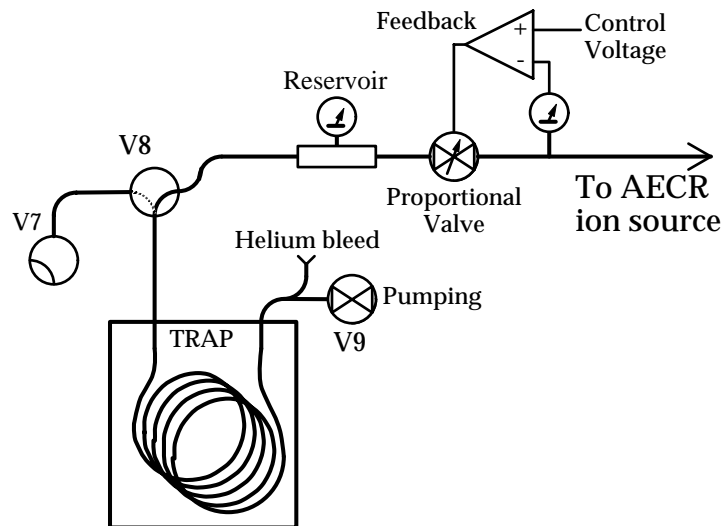


Fig. 4-9: System for injection of activity into the AECR-U ion source at a controlled rate.

As the trap continues to warm, ^{11}C activity, as $^{11}\text{CO}_2$, is released from the trap and passes into the reservoir. A slight flow of helium bled into the system at a controlled rate from just in front of valve V9 aids in purging the activity from the trap. When the trap reaches ~ 230 K, it is disconnected from the reservoir. Pumping through valve V9 is resumed, and the trap is cooled again to liquid-nitrogen temperatures in preparation for the next trapping cycle. The transfer is monitored by three PIN-diode radiation detectors: one on the trap; a second on the reservoir; and a third, attached just after valve V8, that observes the activity flowing in the tubing between the two. Figure 4-10 illustrates data from a typical transfer, showing the cryotrap temperature and the readings in the three radiation detectors. The activity can be seen leaving the trap, passing through the line, and entering the reservoir.

The gas in the reservoir is bled into the ion source at a controlled rate through a proportional solenoid valve controlled by simple feedback from a thermal convection gauge. This feedback maintains the pressure at the outlet at a set value, as long as sufficient gas is available in the reservoir. Stable operation can be easily maintained for reservoir pressures less than a few Torr. The line connecting to the ion source is 4.5-mm i.d. stainless steel and about 3 m long. The conduction of this line is low enough that, even though the AECR-U ion source operates at pressures of a few 10^{-7} Torr, the pressure required at the valve outlet is several milliTorr, which is high enough to be measured and controlled by the thermal convection gauge.

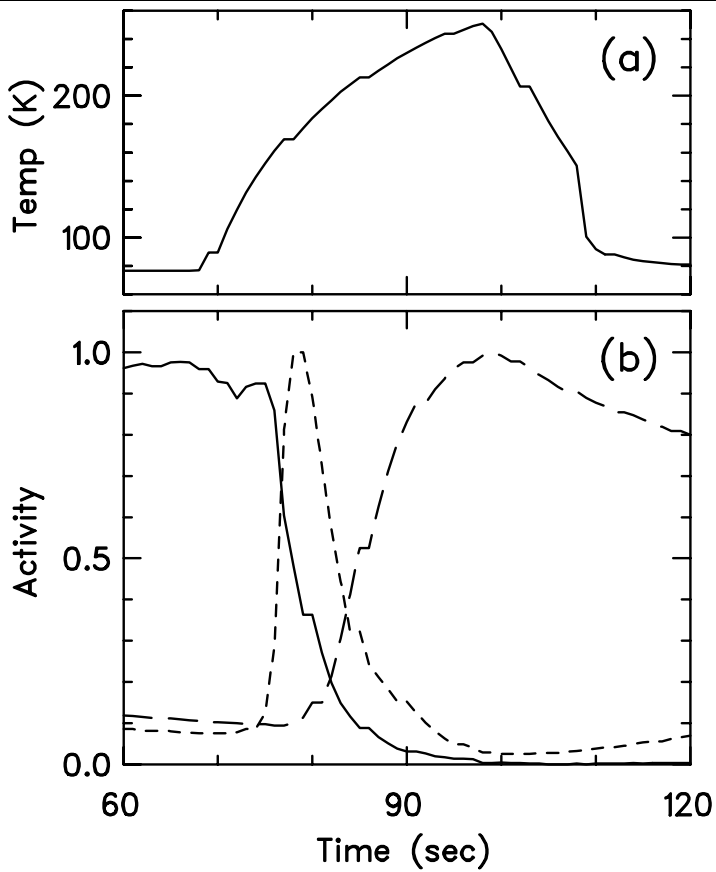


Fig. 4-10: Transfer of ^{11}C activity from the cryogenic trap to the reservoir. The temperature of the trap is plotted in (a) while (b) displays the measured activity at three points: the trap (solid line), the reservoir (long-dashed line), and the line connecting the two (short-dashed line).

4.3.5 Ionization and Acceleration

The controlled injection of activity is crucial to achieve stable operation of the AECR-U ion source. The ^{11}C is ionized, extracted, and accelerated according to the techniques described in the earlier section on development tests. A

stripper foil is located at an appropriate point of the beam line and the $^{11}\text{C}^{6+}$ beam is selected by an analyzing magnet in order to completely eliminate ^{11}B contamination. Once a small amount of fully stripped carbon has been obtained on an amplified Faraday cup (>2 pA), the AEGR-U, injection line, cyclotron, and beam line elements may be fine tuned to maximize the ^{11}C yield on target.

4.4 Production of a Radioactive ^{14}O Ion Beam

Development of ^{14}O as the second BEARS beam also presented considerable technical challenges, due to its short half-life of 71 s and the complicated radiation and surface chemistries of oxygen in the target and on the chamber surface. The usual techniques developed for medical uses of ^{15}O involve the addition of significant amounts of carrier oxygen, which in our case overloads the ECR ion source. As a solution, ^{14}O is produced as water in a carrier-free form, and is chemically converted in two steps to ^{14}O -replaced carbon dioxide, a form readily usable by the BEARS. The radioactive carbon dioxide is again cryogenically separated from the helium transport gas before injection into the 88-Inch Cyclotron's AEGR-U ion source.

4.4.1 ^{14}O Chemistry in BIF

Producing an ^{14}O ($t_{1/2}=71$ sec) beam required considerable additional development, which is described in detail in [Pow03]. Figure 4-11 shows the system for production of H_2^{14}O and its conversion to $[^{14}\text{O}]\text{CO}_2$. In brief, ^{14}O was first produced in the form of H_2^{14}O by bombarding a high-pressure gas target

composed of nitrogen with a few percent hydrogen. The H_2^{14}O vapor was separated from the unloaded target gas through momentary freezing at -40°C , and chemically converted to $[\text{H}_2^{14}\text{O}]^{14}\text{O}$ in two steps: $\text{H}_2^{14}\text{O} \rightarrow \text{C}^{14}\text{O}$ through reaction with graphite at $1000\text{--}1100^\circ\text{C}$ followed by oxidation to $[\text{H}_2^{14}\text{O}]^{14}\text{O}$ over a platinum catalyst. Target unloading, water separation, and chemical conversion took about 15 seconds, after which the $[\text{H}_2^{14}\text{O}]^{14}\text{O}$ was transferred by the helium driver gas to the 88-Inch Cyclotron using the same BEARS systems developed for $^{11}\text{CO}_2$ [Pow00]. Each batch of activity typically was produced every 90 seconds.

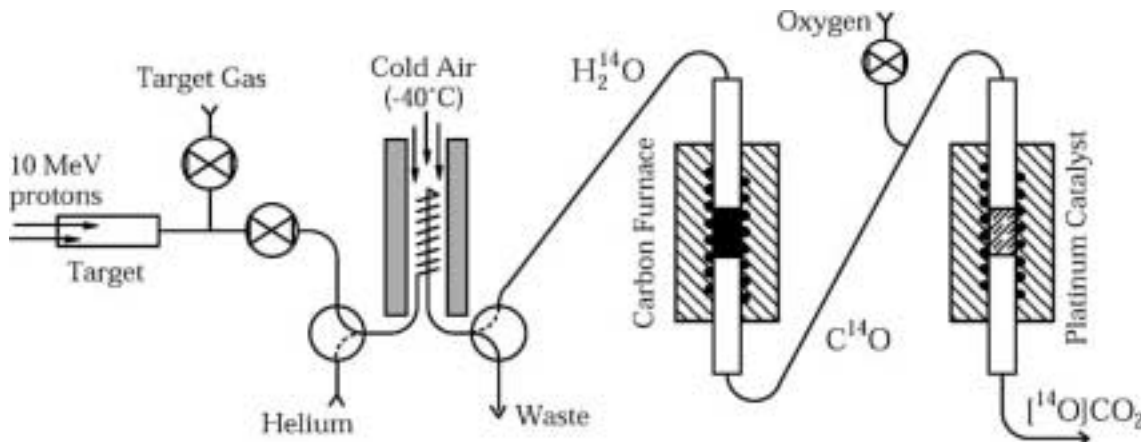


Fig. 4-11: System for production of H_2^{14}O and conversion to $[\text{H}_2^{14}\text{O}]^{14}\text{O}$. The target gas is unloaded to waste through a small coil of stainless steel tubing kept cold by a flow of -40°C air from a vortex tube, in order to freeze out and separate the H_2^{14}O . The activity, released by applying a strong electric current to resistively heat the coil, is carried in a flow of helium through two chemical conversion steps. The first converts H_2^{14}O to C^{14}O over graphite at $1000\text{--}1100^\circ\text{C}$; the second oxidizes the carbon monoxide to $[\text{H}_2^{14}\text{O}]^{14}\text{O}$ over platinum at 180°C [Pow03].

At the 88-Inch Cyclotron, the cryogenically separated $[^{14}\text{O}]\text{CO}_2$ was injected into the ACER-U ion source, using a variable valve to produce a steady gas flow. Although the method of producing ^{14}O first as H_2^{14}O was chosen so as to avoid introducing additional carrier oxygen, there was always some additional carbon dioxide which threatened to overload the ion source. Care needed to be taken to keep the entire system upstream of the chemical conversion steps clean and dry.

As had been previously observed with ^{11}C beams [Pow00], there was a significant slow component in the hold-up time for ^{14}O in the ACER ion source. The beam of oxygen-14 remained a significant time after $[^{14}\text{O}]\text{CO}_2$ injection. When corrected for the radioactive decay of ^{14}O , the beam intensity dropped with a halflife of about three minutes. This may reflect ^{14}O radicals sticking to the source walls, possibly with isotopic exchange effects. Unfortunately, though this effect is of little importance with the 20-minute ^{11}C activity, with 71-second ^{14}O it leads to large decay losses.

4.4.2 Ionization and Acceleration of ^{14}O

Another difficulty was faced when the ^{14}O beam was extracted from the ion source in the 6+ charge state and accelerated to higher energy. As seen in Table 4-1, the ACER-U has the highest ionization efficiency for the ^{14}O 6+ state. To get as high as possible transmission through the 88-Inch Cyclotron [Cer99] and nearly fully stripping efficiency at about 10 MeV/u, a ^{14}O beam energy of 120 MeV was chosen. The mass difference between ^{14}O and ^{14}N nuclei is very small, only 0.001u, resulting in a 2.6 kHz resonance frequency difference for the

120 MeV 6+ ions with the 88-Inch Cyclotron. The cyclotron can only separate frequency differences of 5 kHz. Because the cyclotron cannot cleanly separate $^{14}\text{O}^{6+}$ from the much more intense residual $^{14}\text{N}^{6+}$, the beam was fully stripped to $^{14}\text{O}^{8+}$ by using a thin 204 $\mu\text{g}/\text{cm}^2$ aluminum stripper upstream between two magnets, M32 and M41 in Cave 3. However, it was found that the beam was still contaminated with lower energy $^{14}\text{N}^{7+}$ of the same magnetic rigidity, presumably from scattering from beamline components (Figure 4-12a). Careful RF tuning was done to minimize this effect and obtain reasonable ^{14}O transmission efficiency while allowing less than 1% $^{14}\text{N}^{7+}$ contamination (Figure 4-12b).

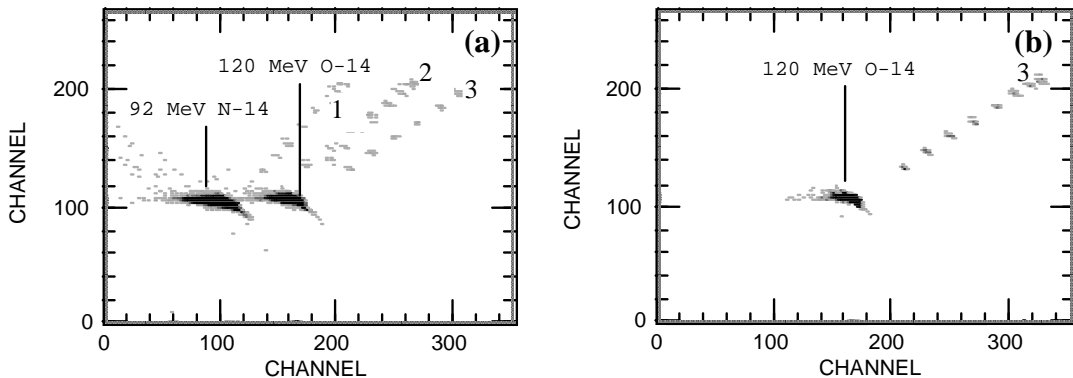


Fig. 4-12: The $\Delta E-E$ spectra showing the ^{14}O beam quality (a) the RF was not optimized for ^{14}O ; (b) RF was optimized for ^{14}O . No ^{14}N was seen. The different beam pile-ups are: 1, ^{14}N pile-up; 2, ^{14}N - ^{14}O pile-up; and 3, ^{14}O pile-up.

The final ^{14}O beam had an intensity that averaged about 8,000 pps on target, with a maximum beam of about 30,000 pps. This is much lower than the maximum of 2×10^8 pps achieved with the ^{11}C beam. Partly, this is due to the 20

times lower production yield of ^{14}O versus ^{11}C [Kit90] as well as losses in the additional chemical processing steps. However, much of the difference also appears to be due to hold up and isotopic exchange losses associated with ionization in the AEGR-U.

C H A P T E R 5

USING RADIOACTIVE ^{11}C ION BEAMS TO MEASURE EXCITATION FUNCTIONS IN THE REACTIONS $^{197}\text{Au}(^{11}\text{C},\text{xn})^{208-\text{x}}\text{At}$

5.1 Introduction

Nuclear models and corresponding computational codes are essential to nuclear research. For fusion-evaporation reactions, a few codes based on statistical models have been developed, such as ALICE [Bla82], HIVAP [Rei81], and PACE [Gav80]. The reliability of these codes needs to be evaluated for different constraints, for example, by changing mass number A, nuclear charge Z and neutron-proton ratio N/Z as inputs. While these codes work reasonably well for reactions involving nuclei near the valley of stability, their validity needs to be tested when nuclei away from this valley are involved in the reactions. It is only recently that radioactive ion beams have become available to perform this particular type of experiment.

In the framework of the BEARS, a relatively simple fusion-evaporation reaction, $^{197}\text{Au}(^{11}\text{C},\text{xn})^{208-\text{x}}\text{At}$, has been investigated to demonstrate the application of radioactive ^{11}C ion beams from BEARS. These results are compared with those from $^{197}\text{Au}(^{12}\text{C},\text{xn})^{209-\text{x}}\text{At}$ with a stable ^{12}C beam, which produce the same astatine isotopes to test fusion-evaporation model code predictions [Joo00].

Table 5-1: α -decay properties for At and Po isotopes.

Isotope	Halflife		E_α [keV]		BR [%]	
^{205}At	26.2 min			5902	10	
^{204}At	9.2 min			5951	3.8	
^{203}At	7.4 min			6087	31	
^{202}At	184 sec	182 sec	6228	6135	18	8.7
^{201}At	89 sec			6344	71	
^{200}At	47 sec	43 sec	6412	6464	43	57
^{202}Po	44.7 min			5587	1.9	
^{201}Po	15.3 min	8.9 min	5683	5786	1.6	2.9
^{200}Po	11.5 min			5862	11.1	
^{199}Po	5.5 min	4.2 min	5952	6059	7.5	24
^{198}Po	106 sec			6181	57	
^{197}Po	56 sec	26 sec	6282	6383	44	84

Since gold is monoisotopic, the only compound nucleus in the reactions of $^{197}\text{Au}(^{11}\text{C},\text{xn})^{208-\text{x}}\text{At}$ is ^{208}At . Each of the astatine isotopes shows a unique signature in its α -decay line, so different isotopes can be identified simultaneously by analyzing the α -energies and half-lives (see Table 5-1). Moreover the polonium α -decay lines due to $^{197}\text{Au}(^{11}\text{C},\text{pxn})^{207-\text{x}}\text{Po}$ reactions and

$^{197}\text{Au}(^{11}\text{B},\text{xn})^{208-\text{x}}\text{Po}$ reactions (because of possible ^{11}B impurities in the beam)

can be easily separated. Table 5-1 shows the α -decay energies, branching ratios, and half-lives for the relevant At and Po isotopes.

5.2 Experiment

Of the three codes mentioned above, HIVAP has generally been found to be in closer agreement with experimental cross sections. However, HIVAP is less efficient than ALICE [Bla82] because HIVAP uses a Monte Carlo approach, in which enormous numbers of trials are required to obtain precise predictions of these cross sections. While HIVAP was used for the final cross section fit, ALICE has been used for experimental planning. The cross sections for the $(^{11}\text{C},\text{xn})$ reactions on gold were calculated using ALICE and are shown in Tables 5-2. The fairly large cross sections enabled us to measure these reactions even with the relatively low beam intensities for radioactive ion beams. With a gold target of 1 mg/cm^2 , the yield per mb cross section and for 10^8 ^{11}C ions/sec can be calculated by

$$Y = \frac{1 \times 10^{-3} \text{ g} \cdot \text{cm}^{-2}}{197 \text{ g} \cdot \text{mol}^{-1}} (6.023 \times 10^{23} \text{ mol}^{-1}) (\sigma \times 10^{-27} \text{ cm}^2) (I \times 10^8 \text{ sec}^{-1})$$

$$= 0.31 \sigma I \text{ (sec}^{-1}\text{)} \quad (5-1)$$

where σ is the cross section in mb and I is the beam intensity in 10^8 ^{11}C ions/sec. With a 10^8 ^{11}C ions/sec beam intensity and the predicted cross sections given in Table 5-2, the yields for most of the astatine isotopes are from a

few to 200 nuclei per second. The yields can be optimized by proper irradiation/counting cycles using the known α -branching ratios, and half-lives as well as the choice of target thickness.

Table 5-2: Predicted $^{197}\text{Au}(^{11}\text{C},\text{xn})^{208-\text{x}}\text{At}$ cross sections at different ^{11}C beam energies.

$E_{^{11}\text{C}}$ [MeV]	σ [mb]					
	^{205}At	^{204}At	^{203}At	^{202}At	^{201}At	^{200}At
50	0	0	0			
60	0.4	30	59	0		
70	0.5	19	473	92	0	
80	0.1	3.6	117	686	86	0
90	0	0.9	22	254	728	27
100		0.3	7.3	70	531	456
110		0.1	2.2	20	166	557
120		0	0.9	7.8	59	260
130			0.4	3.2	19	85
140			0.2	1.7	14	52
150			0	0.7	3.8	16
160				0.3	2.7	10
170				0.2	1.2	4.7
180				0	0.7	2.7

The Coulomb barrier E_C for ^{11}C on ^{197}Au is calculated to be about 65 MeV by equation 5-2:

$$E_C = 1.44 \frac{Z_1 Z_2}{r_0 (A_1^{1/3} + A_2^{1/3})} \quad (5-2)$$

where Z_1 , A_1 , Z_2 , and A_2 are the nuclear charge and the mass of the projectile and target nucleus, respectively, and r_0 is the radius constant with a value

taken to be 1.3 fm. As Table 5-2 shows, the cross sections for most astatine isotopes are small when the beam energy is above the 120 MeV ^{11}C beam energy. Therefore, the energy range investigated was from about 65 MeV to 120 MeV.

The data were taken in three runs during both the development and the commissioning phases of the BEARS system. During the development phase, before completion of the transfer line, two runs were dedicated to tests of the injection of ^{11}C into the AEGR source, following by ionization and acceleration through the 88-Inch Cyclotron. For this purpose, a total of twelve ≈ 1 Ci batches of ^{11}C as CO_2 were produced at the BIF cyclotron and trapped in a portable lead-lined Dewar. The Dewar was transported to the 88-Inch Cyclotron and the $^{11}\text{CO}_2$ was injected into the AEGR ion source using a prototype BEARS system. Each batch produced a beam of typically $(0.5\text{-}1) \times 10^8$ ions/sec for a period of ≈ 20 min. The third run was performed during the commissioning phase of the activity transfer line, when ^{11}C bursts of ≈ 200 mCi were transferred every 5 min and continuously fed into the AEGR ion source.

In all runs $^{11}\text{C}^{4+}$ ions were accelerated to $E_{^{11}\text{C}} = 120$ MeV. Before entering Cave 2, the beam passed through a 1.2 mg/cm^2 aluminum stripper foil mounted in front of the last bending magnet in the 88-Inch Cyclotron vault to fully strip the ^{11}C to the 6+ charge state. This permitted the separation of the ^{11}C ions from the co-resonant $^{11}\text{B}^{4+}$ ions also produced by the ion source. As described in

Chapter 4, the high quality radioactive ^{11}C ion beam guarantees minimum contamination from ^{11}B .

Figure 5-1 shows the target and detector set-up. To measure excitation functions, the beam energy was varied using aluminum degrader foils of 3.2 to 21.2 mg/cm² thickness. Thus, after the degraders, the initial beam energies were from 116 MeV (3.2 mg/cm²) to 93 MeV (21.2 mg/cm²). These varied energies allowed the measurement of a large number of data points in a given beam time. The beam intensity was monitored by measuring Rutherford scattering on a 5 mg/cm² gold foil using a silicon $\Delta E-E$ particle-identification telescope mounted at an angle of 15° to the beam. The telescope was calibrated for the absolute ^{11}C beam intensity by comparing its measured elastic scattering rate with ^{11}C activity that was collected on a catcher foil directly behind the scattering target and subsequently counted offline.

The target setup consisted of three 250 $\mu\text{g}/\text{cm}^2$ gold targets mounted at an angle of 15° towards the beam axis, resulting in an effective target thickness of 966 $\mu\text{g}/\text{cm}^2$. The gold foil acted as both targets and catcher foils for astatine recoils. The thin target minimizes the energy loss of the α -particles in the target foils (when they are counted; see below). On the other hand, the larger effective thickness obtained by the 15° angle maximizes the yield of the astatine isotopes. Between each pair of targets 7.5 mg/cm² aluminum foils were mounted to decrease the beam energy by steps of ~5 MeV, thus allowing three energy points to be measured simultaneously. These degrader foils were backed with a

1 mg/cm² gold layer in order to compensate partially for recoils leaving the targets. With degraders between targets, the lowest energy that was reached was about 65 MeV. For the first target, the elastic-scattering target served the same purpose. The setup was mounted on a plunger system, thus allowing the targets to be simultaneously moved in less than 1 sec from the beam axis to a position between individual pairs of 500 μm thick, 450 mm² Si detectors, each about 7 mm from a target. There the α -particles are stopped in less than 35 μm of detector material. The solid angle for the detection of the astatine α -decays was $\approx 17\%$ of 4π sr for each detector, depending on the size of the beam spot on target for a given set of degraders.

The detector resolution was on the order of ≈ 27 keV FWHM. The energy loss in 250 $\mu\text{g}/\text{cm}^2$ thick gold targets is $\Delta E = 53 \pm 7$ keV for 6 MeV α -particles by SRIM calculation. However, depending on the origin of the decay in the 250 $\mu\text{g}/\text{cm}^2$ target and the angle of the emitted α particle, an energy loss of up to 100 keV in the target was taken into account.

For a given initial energy, the measurement was performed in a cyclic manner with alternating irradiation and counting periods. To optimize the yield, the irradiation and α -decay counting times were chosen based on the half-lives of the expected astatine isotopes (ranging from 43 sec for ^{200}At to 29.4 min for ^{206}At):

$$A = N_0 \sigma I (1 - e^{-\lambda t_1}) (1 - e^{-\lambda t_2}) \quad (5-3)$$

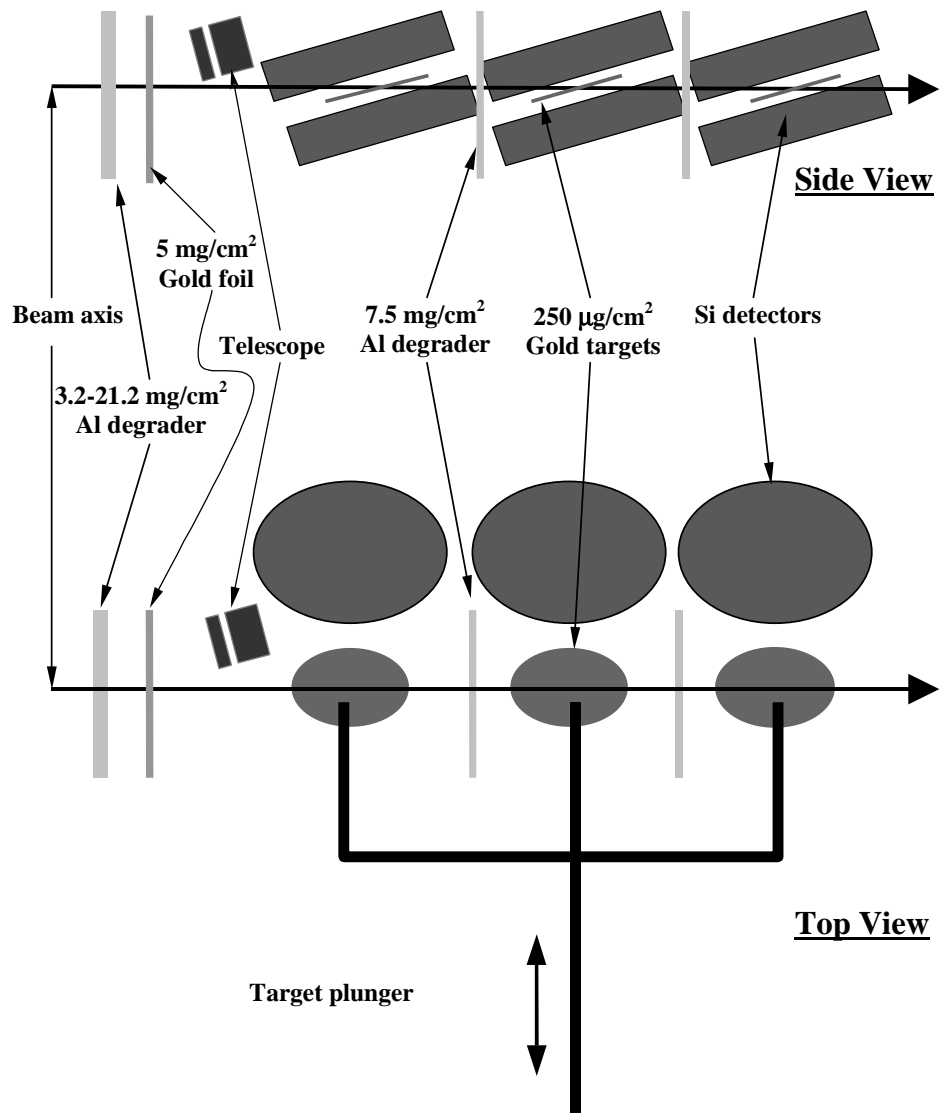


Fig. 5-1: Target and detector setup. Both the side view and the top view are shown. See text for details.

where N_0 is the target density, σ the cross section, I the beam intensity, t_1

the irradiation time, t_2 the counting time, λ the decay constant $\left(\frac{\ln(2)}{t_{1/2}}\right)$. The re-

sults were corrected for contamination by prior irradiations. The α -decay ener-

gies range from 5703 keV for ^{206}At to 6464 keV for ^{200}At [Fir96, Sch87a, Sch87b].

5.3 Results and Discussion

5.3.1 α -spectra

Figure 5-2 shows a typical α spectrum from the experiments during the “batch” runs with a degraded 93 MeV ^{11}C beam. Besides the α -decay groups of the astatines, the decay lines of polonium isotopes can also be observed. These predominantly resulted from the decay of the EC daughter nuclei of the astatine isotopes. The observed resolution is primarily due to the energy loss of the α -particles in the $250 \mu\text{g}/\text{cm}^2$ gold targets.

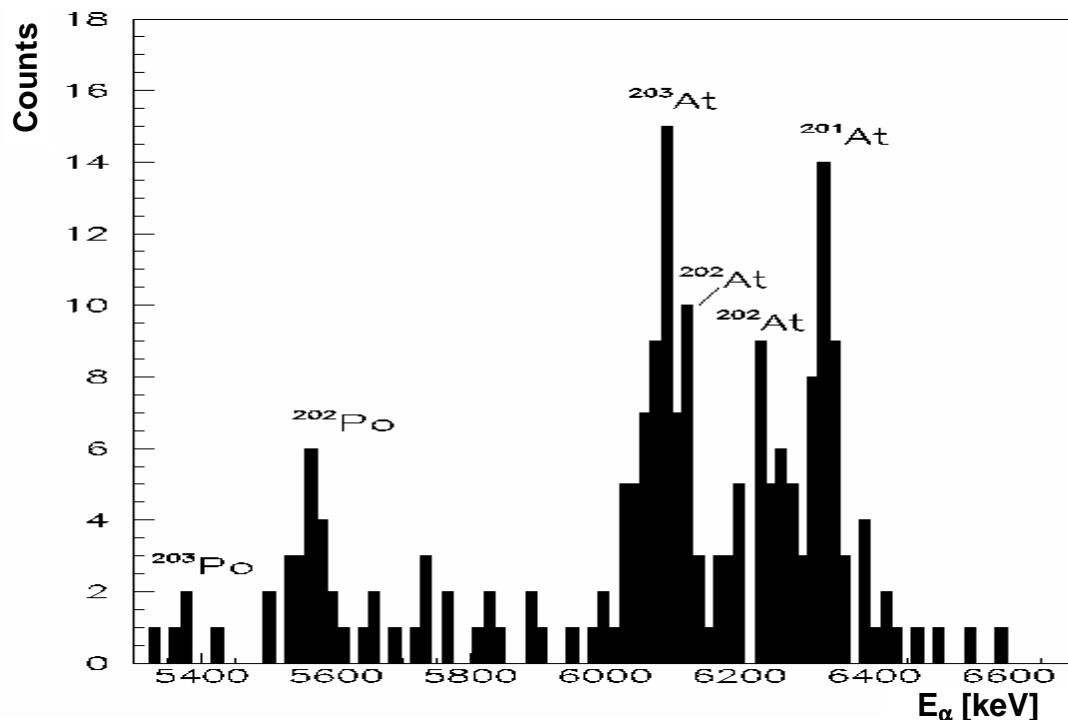


Fig. 5-2: Measured α -spectrum at a degraded 93 MeV ^{11}C beam.

Figure 5-3 shows α -decay spectra obtained at different bombarding energies for the $^{197}\text{Au}(^{12}\text{C},xn)^{209-x}\text{At}$ and $^{197}\text{Au}(^{11}\text{C},xn)^{208-x}\text{At}$ reactions. The ^{11}C data obtained in the continuous-beam mode (Figure 5-3e and Figure 5-3f) had

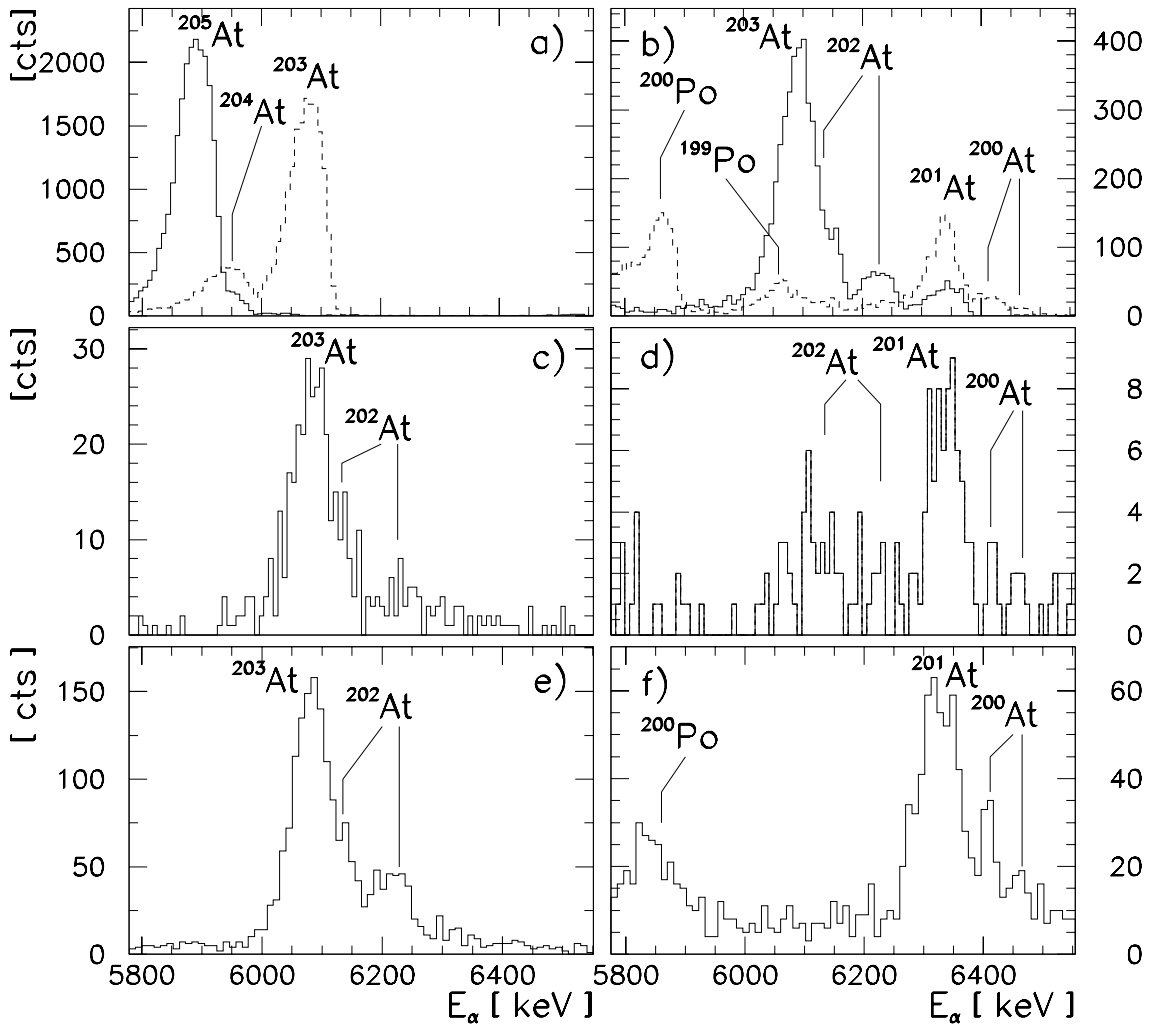


Fig. 5-3: α spectra from the $^{197}\text{Au}(^{12}\text{C},xn)^{209-x}\text{At}$ and $^{197}\text{Au}(^{11}\text{C},xn)^{208-x}\text{At}$ reactions at various energies. (a) ^{12}C at 76 MeV and 93 MeV (dashed line); (b) ^{12}C at 110 MeV and 132 MeV (dashed line); (c) ^{11}C in batch mode at 81 MeV; (d) ^{11}C in batch mode at 94 MeV; (e) ^{11}C in continuous mode at 84 MeV; (f) ^{11}C in continuous mode at 107 MeV.

much better statistics than the data obtained in batch mode (Figure 5-3c and Figure 5-3d), decreasing the statistical error significantly. The detector resolution combined with energy loss in the targets made it impossible to resolve α lines such as the 5951 keV decay of ^{204}At and the 5901 keV decay of ^{205}At , or the 6135 keV ^{202}At and the 6087 keV ^{203}At peaks, using energy information only.

Decay curves based on the halflives of the α decays were used to separate these decays. This worked very well for data with high statistics, such as the ^{12}C data. However, for low statistics, such as the ^{11}C data in batch mode, this method can cause significant errors. Because the $2n$ and $3n$ channels were not observed in the ^{11}C data, only the 6135 keV ^{202}At and the 6087 keV ^{203}At α -decays had to be separated. This was achieved by measuring the 6228 keV ^{202}At α decay. Using the known branching ratios, a calculated 6135 keV ^{202}At α -decay branch could then be subtracted from the $^{202}\text{At}/^{203}\text{At}$ peak. However, since the branching ratio of 6135 keV ^{202}At α -decay is $8.7 \pm 1.5\%$ with a large uncertainty, the error for this subtraction is large.

5.3.2 $^{197}\text{Au}(^{12}\text{C},xn)^{209-x}\text{At}$

Prior to using the ^{11}C beam, the $^{197}\text{Au}(^{12}\text{C},xn)^{209-x}\text{At}$ excitation functions were measured for the $3n$ to $9n$ channels at beam energies ranging from 60 to 130 MeV. These results were compared with earlier data by Thomas *et al.* [Tho62] and Bimbot *et al.* [Bim68], corrected for the more recent α -branching ratios of [Fir96, Sch87a, Sch87b]. The results of these two earlier measurements differ as much as a factor of 3, making a remeasurement desirable. Fig-

ure 5-4 shows the cross sections for the $^{197}\text{Au}(^{12}\text{C},xn)^{209-x}\text{At}$ reactions obtained in this experiment compared to the previous data. Our errors include the statistical errors as well as those due to uncertainties in beam intensity of $\approx 10\%$ and in detector efficiency and recoil collection efficiency of $\approx 5\%$. The results of this experiment are more consistent with the measurements of Thomas *et al.* [Tho62]. However, deviations can be seen in the $4n$ channel and for energies higher than 110 MeV. In the $4n$ channel, the Thomas *et al.* data show a sharp dropoff after reaching the peak of the excitation function. However, the Bimbot *et al.* [Bim68] data suggest a much smoother trend, comparable to our data. The cross sections we obtained for energies above 110 MeV are generally higher than those in the Thomas *et al.* data [Tho62]. The curves indicate results of a calculation using the fusion-evaporation code HIVAP [Rei81]. The best agreement with our data was obtained using the “default configuration” with a $\approx 10\%$ reduced scaling parameter of the level density constant. Moreover, all calculated cross sections had to be divided by a factor of 4 to match the data, which still is in good agreement within the predictive power of the statistical model used in fusion-evaporation codes. The general agreement of the predicted excitation functions with the data is good with the exception of the $6n$ channel leading to ^{203}At and the $8n$ channel leading to ^{201}At , where the maximum cross section is still overpredicted by a factor of more than two. This discrepancy may also be similar to results found in the incomplete fusion reactions with light heavy ion beams (^{12}C) [Ver93, Par91, Lun99, Mor04]. It is notable that the agreement of the summed cross section over all exit channels is very good.

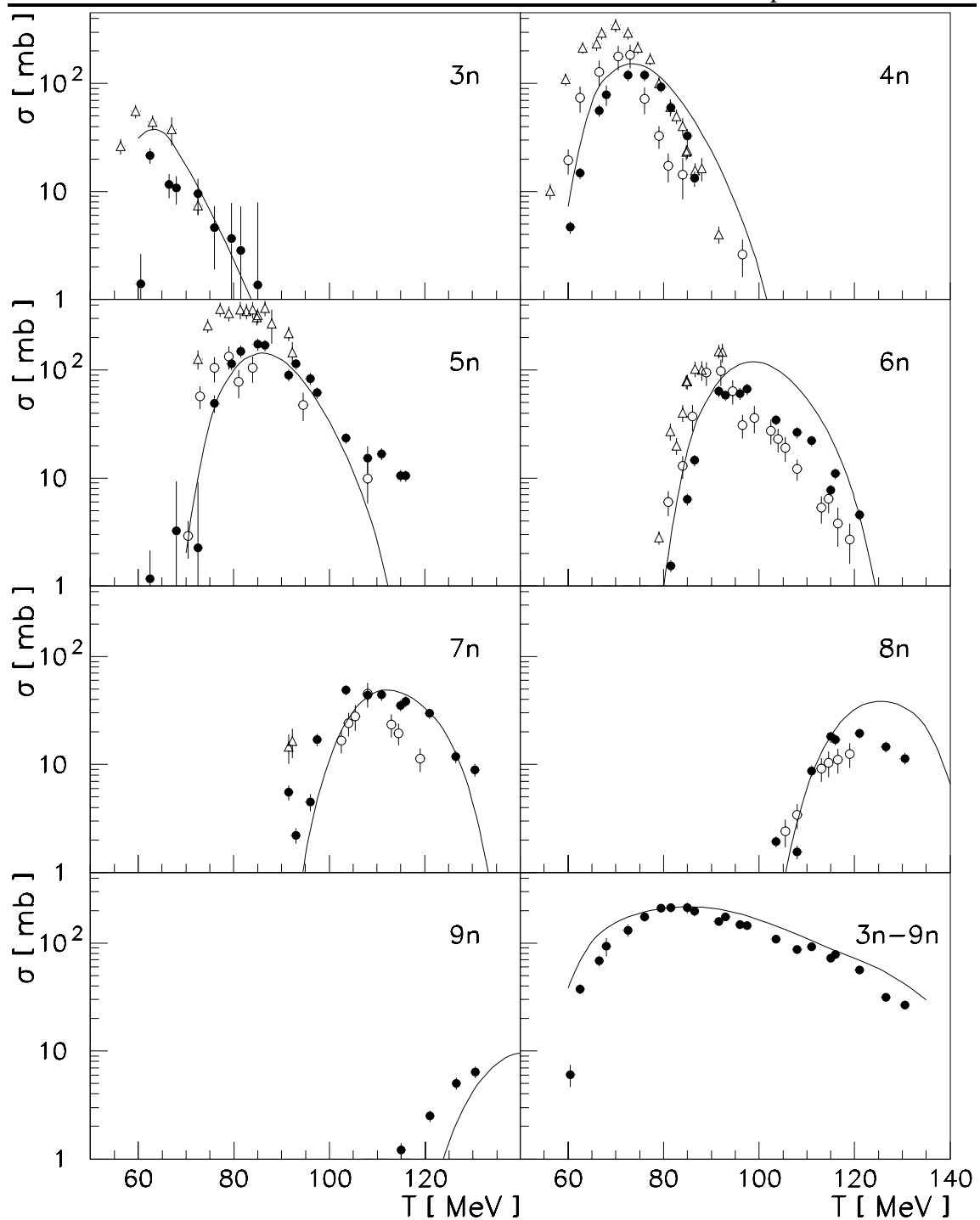


Fig. 5-4: $^{197}\text{Au}(^{12}\text{C}, xn)^{209-x}\text{At}$ excitation functions. The filled circles are the current data. The open circles represent the data of Thomas et al. [Tho62] while the open trian-

gles are the data of Bimbot et al. [Bim68]. The lines represent the predictions of the HIVAP code optimized for these data.

However in another experiment producing the isotope ^{203}At , no discrepancy between the measured and the statistical model predictions regarding ^{203}At evaporation residue (see Figure 5-5a) was found in the 4n channel of the fusion-evaporation reaction of $^{19}\text{F} + ^{188}\text{Os}$ [Mah03].

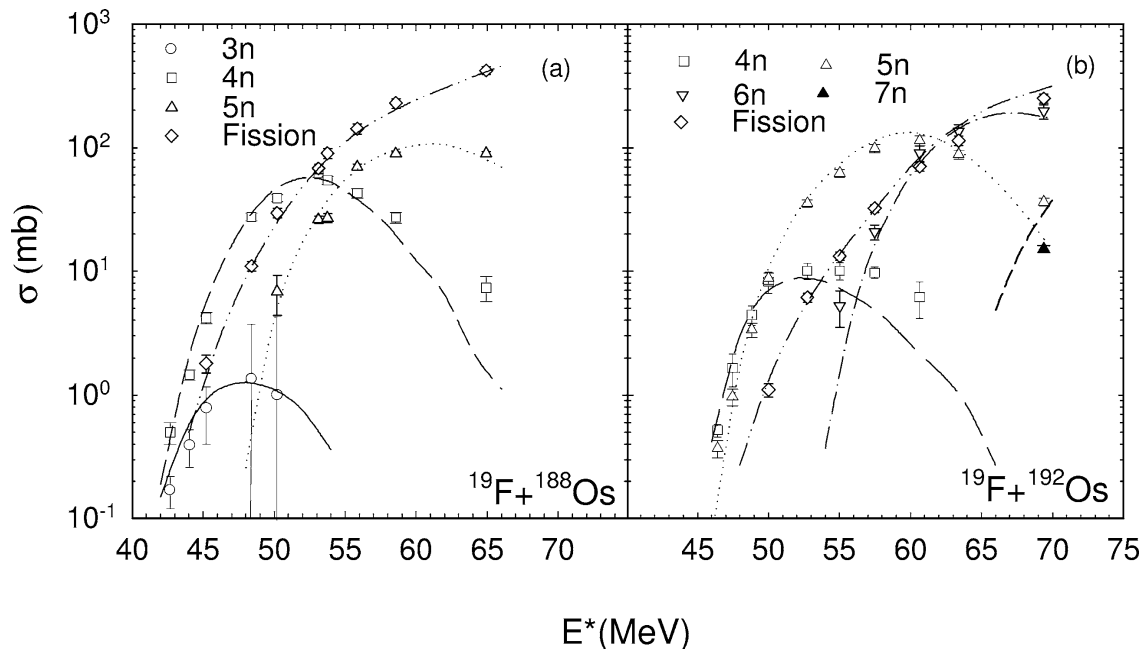


Fig. 5-5: Measured evaporation residue and fission excitation functions are compared with statistical model calculations for (a) $^{19}\text{F} + ^{188}\text{Os}$ and (b) $^{19}\text{F} + ^{192}\text{Os}$ system. The continuous, the dashed, the dotted, the dot-dashed, the short dashed and the dot-dot-dashed lines represent the statistical model fit for 3n, 4n, 5n, 6n, 7n, and fission cross-sections, respectively [Mah03].

Mahata *et al.* [Mah03] pointed out that the discrepancy between the measurement and the statistical model calculation reported in our work could be due to the use of an incorrect branching ratio in evaluating ^{203}At formation cross-sections, rather than deficiencies in the statistical model calculation. If this is true, the branching ratios reported in the literature will require further investigation.

5.3.3 $^{197}\text{Au}(^{11}\text{C},xn)^{208-x}\text{At}$

Figure 5-6 shows the cross sections for the $4n$ to $8n$ channels in the $^{197}\text{Au}(^{11}\text{C},xn)^{208-x}\text{At}$ reactions obtained in our experiments. The data taken in the continuous-beam mode have significantly smaller errors due to the improved statistics. The larger errors in the $4n$ and $6n$ channels are due to the low α -branching ratios of 3.8% for ^{204}At and 4.3% for the 6228-keV line of ^{202}At . The $8n$ channel also shows higher uncertainties. Here the short half-life of ^{200}At leads to a smaller saturation yield and, therefore, to a significantly reduced count rate, especially for the batch-mode data.

The curves in Figure 5-6 again show the predictions of the HIVAP calculations using the compound-nucleus parameter set optimized for the $^{197}\text{Au}(^{12}\text{C},xn)^{209-x}\text{At}$ reactions (and again divided by four). The agreement of the predictions with the data, though not as good as for ^{12}C , is fairly reasonable. The deviations are larger close to the barrier, where fusion-evaporation codes are generally very sensitive to the input parameters. The $6n$ channel is reproduced very well. For the $4n$ channel, the magnitude of the predicted cross section agrees with the measurement; however, the maximum is observed at a

higher energy than predicted. The $5n$ channel and the $7n$ channel leading to ^{203}At and ^{201}At , respectively, are still overpredicted by a factor of approximately three. The excitation function summed over the $4n$ - $8n$ exit channels shows that the HIVAP code generally overpredicts the yield. However, the summed $4n$ - $8n$ cross section (when divided by four) agrees within a factor of two with the data.

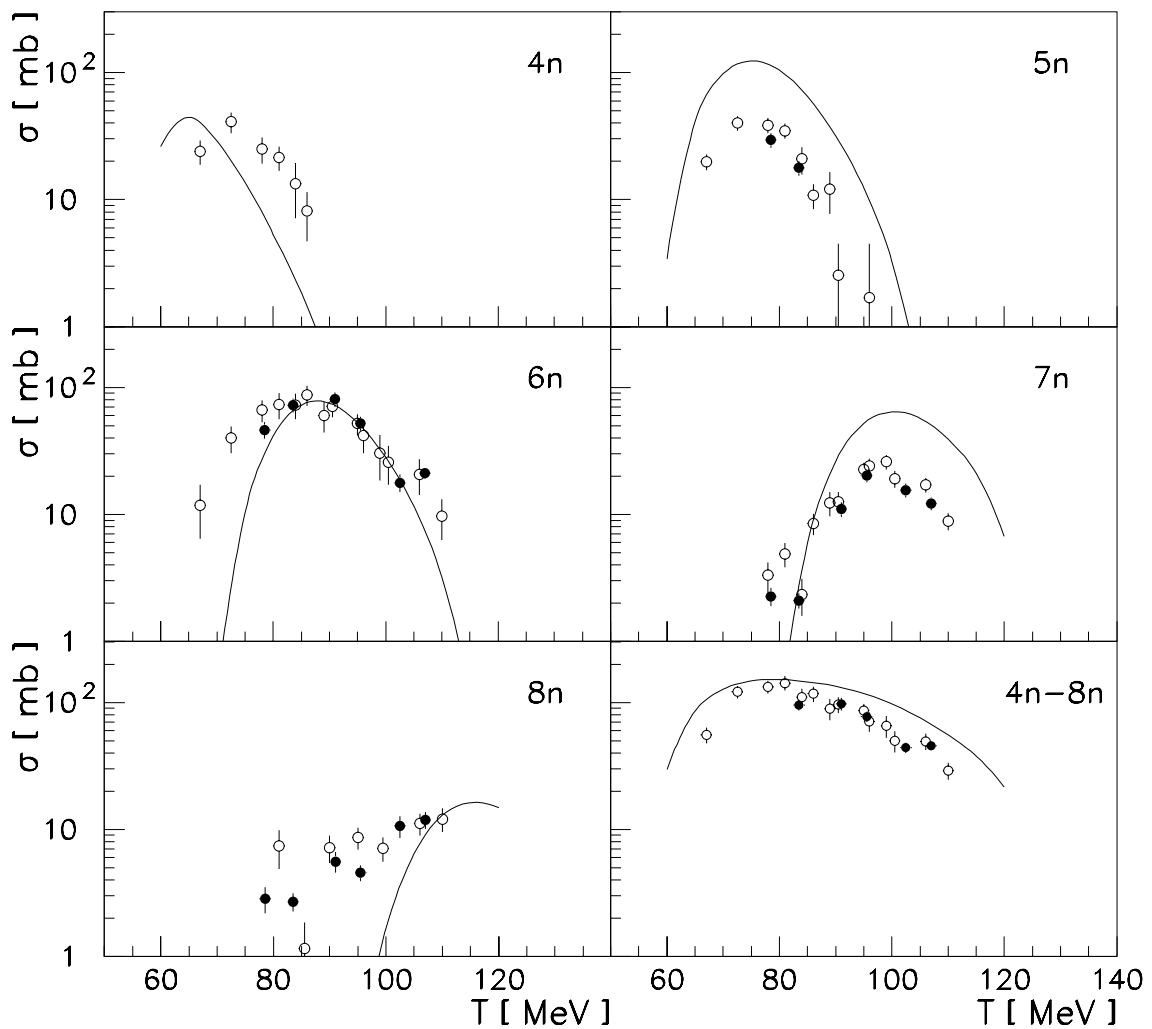


Fig. 5-6: $^{197}\text{Au}(^{11}\text{C},\text{xn})^{208-\text{x}}\text{At}$ excitation functions. The open circles are data taken in batch mode, while the filled circles represent the data taken in the continuous-beam mode. The lines represent predictions of the HIVAP code. See text.

5.3.4 Comparisons of $^{197}\text{Au}(^{11}\text{C}, xn)^{208-x}\text{At}$ with $^{197}\text{Au}(^{12}\text{C}, xn)^{209-x}\text{At}$

Table 5-3 compares the measured cross sections in the $(^{11}\text{C},xn)$ and $(^{12}\text{C},xn)$ reactions. The resulting cross section ratios are compared to HIVAP predictions. One can see that the use of a radioactive ^{11}C beam leads to higher cross sections for the production of neutron-deficient astatine isotopes when the required beam energies are well above the Coulomb barrier. This is not surprising, since one neutron less has to be evaporated using a ^{11}C beam to produce the same final astatine isotope. However, the increase in the cross sections is only on the order of a factor of two. Taking the lower beam intensity of a radioactive ^{11}C beam into account, it is evident that the use of this beam is advantageous only when using a stable ^{12}C beam is not convenient.

Although the cross sections for the $(^{11}\text{C},5n)$ and $(^{11}\text{C},7n)$ reactions (when divided by four) are overpredicted by a factor of up to three, the predicted and measured ratios of the ^{11}C and ^{12}C reaction cross sections leading to the same final isotopes agree reasonably well. The reason might be that the corresponding $(^{12}\text{C},6n)$ and $(^{12}\text{C},8n)$ reactions are overpredicted as well. In this context, it is also worth noting that the xn channels following these overpredicted channels [$(^{11}\text{C},6n)$, $(^{11}\text{C},8n)$, $(^{12}\text{C},7n)$, and $(^{12}\text{C},9n)$] open up at energies below the predicted ones. The code appears to treat either the cutoff of the overpredicted channels or the opening of the subsequent channels incorrectly. Apparently, the deviations of the predictions from the measured cross sections are caused by

an effect related to the produced isotopes, not the xn channel involved. This effect could be due to nuclear structure and requires further investigation. In general, however, predictions of the $(^{11}\text{C},xn)$ cross sections using the fusion evaporation code HIVAP give reasonable results; in particular, the ratios of the ^{11}C and ^{12}C cross sections are reproduced satisfactorily in the energy region well above the Coulomb barrier. Therefore, this code appears to be a good tool for estimating yields for reactions using beams of radioactive ions near stability, especially when the cross sections involving a stable isotope of the same beam element are known.

Table 5-3: Measured and predicted cross section ratios in $(^{11}\text{C},xn)$ and $(^{12}\text{C},xn)$ channels.

Isotope	Reaction	$\sigma_{\text{max}} [\text{mb}]$	Measured		Predicted
			$\frac{\sigma_{^{11}\text{C}}}{\sigma_{^{12}\text{C}}}$	$\frac{\sigma_{^{11}\text{C}}}{\sigma_{^{12}\text{C}}}$	$\frac{\sigma_{^{11}\text{C}}}{\sigma_{^{12}\text{C}}}$
^{204}At	$(^{11}\text{C},4\text{n})$	41.1 ± 7.6	0.24 ± 0.05		0.31
	$(^{12}\text{C},5\text{n})$	173.5 ± 22.9			
^{203}At	$(^{11}\text{C},5\text{n})$	40.1 ± 5.1	0.60 ± 0.11		1.05
	$(^{12}\text{C},6\text{n})$	66.7 ± 8.0			
^{202}At	$(^{11}\text{C},6\text{n})$	87.5 ± 15.5	1.98 ± 0.42		1.60
	$(^{12}\text{C},7\text{n})$	44.3 ± 5.3			
^{201}At	$(^{11}\text{C},7\text{n})$	26.1 ± 3.4	1.34 ± 0.23		1.67
	$(^{12}\text{C},8\text{n})$	19.5 ± 2.1			
^{200}At	$(^{11}\text{C},8\text{n})$	12.1 ± 2.6	1.89 ± 0.47		1.69
	$(^{12}\text{C},9\text{n})$	6.4 ± 0.8			

5.4 Conclusion

In conclusion, the first experiment using BEARS, the light-ion radioactive-beam capability at the LBNL 88-Inch Cyclotron, was successful. A ^{11}C beam with intensities of $(1\text{-}2)\times 10^8$ ions/sec on target was used to measure the excitation functions for the $4n$ to $8n$ exit channels in the $^{197}\text{Au}(^{11}\text{C},xn)^{208\text{-}x}\text{At}$ reactions. The measured cross sections were satisfactorily predicted using the fusion-evaporation code HIVAP. To investigate the overpredictions for even-neutron final nuclei, a detailed comparison of our data to the code needs to be performed. Also, possible errors in the branching ratios of α decays from At isotopes and the presence of incomplete fusion reactions are probably contributing to the overpredictions.

The BEARS system was also used to measure excitation functions in the $^{197}\text{Au}(^{11,12,13}\text{C, fission})$ reactions [Pea00]. These additional data will be very useful in understanding the deexcitation processes of the compound nuclei.

ENERGY LEVELS OF ^{15}F

6.1 Introduction

Light nuclei near and beyond the driplines provide a test bed for new nuclear structure phenomena, both from the experimental and the theoretical point of view [Lep03]. In the past two decades, new phenomena such as halo nuclei [Tan85a, Tan85b, Tan88, Kob88], as well as the disappearance of magic number effects [Nav00] along the neutron dripline and the concomitant appearance of new magic numbers [Oza00] have been observed. It is of great interest to see whether similar phenomena can be discovered near the proton dripline. To explore these phenomena, it is essential to have accurate and detailed information of these exotic nuclei, i.e., their energy spectra, and the spins and parities of their levels. With the development of new beam technologies, such as radioactive ion beams, it is possible to get information on nuclei far from the valley of stability that is difficult or impossible to acquire by traditional methods.

Proton rich beams provided by BEARS [Pow00, Pow03] make it possible to explore nuclei at or beyond the proton dripline. With the ^{14}O beam, the $T_z = -3/2$ nucleus ^{15}F has been investigated by elastic resonance scattering of ^{14}O on

a target containing hydrogen. ^{15}F has been of nuclear structure interest in a variety of calculations including predictions of the energy levels of $T_z = -3/2$ nuclides [Ant88, Bri98], Thomas-Ehrman shifts across $T=3/2$ multiplets [Oga99] and the disappearance of magic number effects due to unbalanced neutron-proton ratios [Pet03, Tho03]. The mass of ^{15}F is also critical for evaluating the relative di-proton decay probability of ^{16}Ne compared to the one proton decay probability [Tho01].

^{15}F is a member of a $T=3/2$ isobaric quartet, which also includes ^{15}C , ^{15}N , and ^{15}O . Energy levels of ^{15}F can be used to establish systematics within this isobaric multiplet, an example being the assignment of a $T=3/2$, $J^\pi = 1/2^+$, $E_{\text{ex}} \sim 11$ MeV state in ^{15}O [Ant88].

Another interest lies in investigating the Thomas-Ehrman shift (TES) between ^{15}C and its mirror nuclei ^{15}F -- the asymmetric effects in the energy levels between mirror nuclei [Tho52, Ehr51] (see Figure 1). The TES can be used to predict distortions in the expected energy spectra of mirror nuclei, especially for $Z > N$ nuclei from their $N > Z$ mirror nuclei. The systematic study of TES will help theorists correctly calculate the energy spectra of proton-rich nuclei [Oga99].

The magic numbers in the valley of stable isotopes reflect the shell closures of nuclei [Kra88c]. As one moves toward and beyond the dripline, the “standard” magic numbers may disappear and new magic numbers may emerge [Nav00, Oza00, Pet03, Tho03]. A question has been raised about the possible disappearance of shell closure around $Z=8$ for $T_z=-3/2$ nuclides. The focus of this issue is the position of the ground state of ^{15}F .

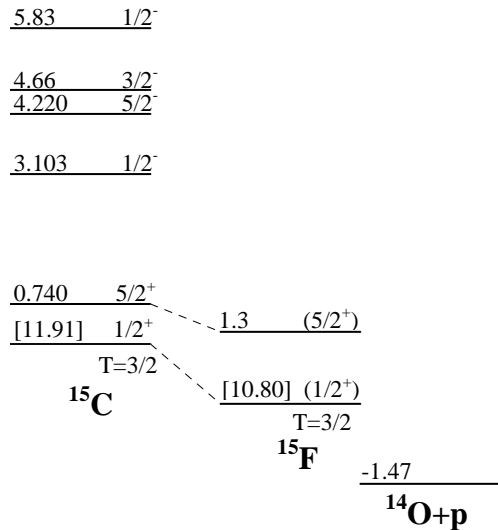


Fig. 6-1: Known energy levels of ^{15}F and ^{15}C [Ajz91].

In the seventies, the energy levels of ^{15}F were investigated by Kekelis *et al.* [Kek78] and by Benenson *et al.* [Ben78] with the low cross-section transfer reaction $^{20}\text{Ne}(^3\text{He}, ^8\text{Li})^{15}\text{F}$. Only two levels have been observed so far, the ground state and the first excited state (see Fig. 6-1). The adopted values for these two levels are 1.47 ± 0.13 and 2.77 ± 0.10 MeV relative to the mass-energy of a proton and ^{14}O [Ajz91]; their widths are reported to be 1.0 ± 0.2 MeV and 0.24 ± 0.03 MeV, respectively. Since the cross section is small, about $1\text{-}4 \mu\text{b}$, the statistics were poor for both states. Recently, these two levels have been re-investigated by several authors [Lep03, Pet03, Gre97, Gol04] using two reactions: the elastic scattering reaction $^{14}\text{O} + \text{p} \rightarrow ^{15}\text{F}$ and the transfer reaction $^{16}\text{O}(^{14}\text{N}, ^{15}\text{C})^{15}\text{F}$. While most of these experiments agree quite well with one another on the position of the first excited state, questions have remained about

the energy and the width of the broad ground state. To clarify this question, a new measurement of low-lying ^{15}F levels using elastic scattering of ^{14}O on a hydrogen target in an inverse kinematics thick target arrangement was completed and analyzed.

6.2 Experiment

The experiment applied the ERSIKTT technology described in Chapter 3 and the ^{14}O beam described in Chapter 4. An 120 MeV ^{14}O beam was directed onto a target consisting of a 17.8 μm Nickel degrader followed by a thick polyethylene foil (200 μm $[\text{CH}_2]_n$, density 0.92 g/cm³). The target combination was chosen to completely stop 120 MeV ^{14}O (and ^{14}N , as a beam used for calibration).

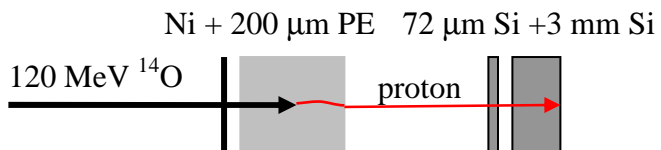


Fig. 6-2: The experimental setup for the $^{14}\text{O} + \text{p}$ thick target elastic resonance scattering experiment.

Scattered protons from the polyethylene (PE) were observed in a ΔE - E silicon detector telescope at 0° in the lab (see Fig. 6-2). The ΔE and E detectors were 72 μm and 3 mm thick, respectively, and were at a distance of 14.6 cm from the target, subtending an angle of about ±5° in the lab frame (correspond-

ing to $\pm 10^\circ$ about 180° in the center of mass). The beam intensity was occasionally measured by removing the thick target and counting the direct beam. It ranged between 1000 and 30000 ^{14}O ions/s. Because of variations in beam intensity, the total beam on target during runs could only be crudely estimated.

The advantage of this thick-target inverse-kinematics technique is simultaneous collection of the entire elastic-scattering excitation function, as the ^{14}O ions lose all their energy in the polyethylene target. The observed proton energies $E_{\text{m,lab}}$ can be directly translated to the excitation energies of the reaction, $E_{\text{c.m.}}$, by Equation 3-3:

$$E_{\text{c.m.}} = \frac{m + M}{4M\cos^2\theta_{\text{lab}}} E_{\text{m,lab}} \quad (6-1)$$

As discussed in Chapter 3, a correction must be made to the observed proton energies due to energy losses in the target. Interactions at lower excitation energies occur deeper in the thick target thus reducing the amount of material remaining to retard the scattered proton. Thus, an energy loss correction factor can be calculated as a function of center-of-mass energy, using knowledge of stopping powers, incoming beam energy, and target thicknesses. Stopping powers for ^{14}O , ^{14}N , and protons were calculated from SRIM [Zie03].

As discussed in section 3.2.5, to relate the observed yield of protons to a relative cross section versus energy, one must correct for the changing energy loss of the bombarding ion as it slows down. The elastic scattering excitation function is calculated from yields multiplied by beam ion energy loss by Equation 3-7:

$$\sigma \propto Y \times dE/dx. \quad (6-2)$$

The detector system was calibrated by using a beam of 120 MeV ^{14}N . Figure 6-3 shows the resulting spectrum of protons, which has been energy-matched to previous experimental determinations of $^{14}\text{N} + \text{p}$ using conventional kinematics. The excitation functions from two such experiments are shown: lower energy measurements at $\theta_{\text{c.m.}} = 168.1^\circ$ from Olness *et al.* [Oln58], and higher energy data at $\theta_{\text{c.m.}} = 159.1^\circ$ from West *et al.* [Wes69]. A small nonlinear correction has been made for the calculated energy loss of the protons exiting the polyethylene target; otherwise the calibration is linear. The yield of protons in the thick-target inverse kinematics experiment has been corrected by the energy loss of ^{14}N in polyethylene in order to produce a relative cross section.

The presence of several peaks and structures can be readily seen in the inverse kinematics data. These structures sit upon a significant background contributed by protons from ^{14}N reactions on the carbon component in the polyethylene target and on the nickel degrader foil. This background was investigated with a pure carbon target in place of the polyethylene target and was found to be smooth in shape.

The experimental resolution can be determined from the width of the narrow resonance just below 3 MeV; it is found to be about 60 keV in the center of mass frame. The major contributions to this resolution are estimated to be 40 keV from the E detector; 27 keV from the ΔE detector; 30 keV due to the $\pm 10^\circ$ angular spread in the center of mass; and 19 keV due to the beam spread and

the straggling of both the incident beam and the scattering proton inside the degrader and target.

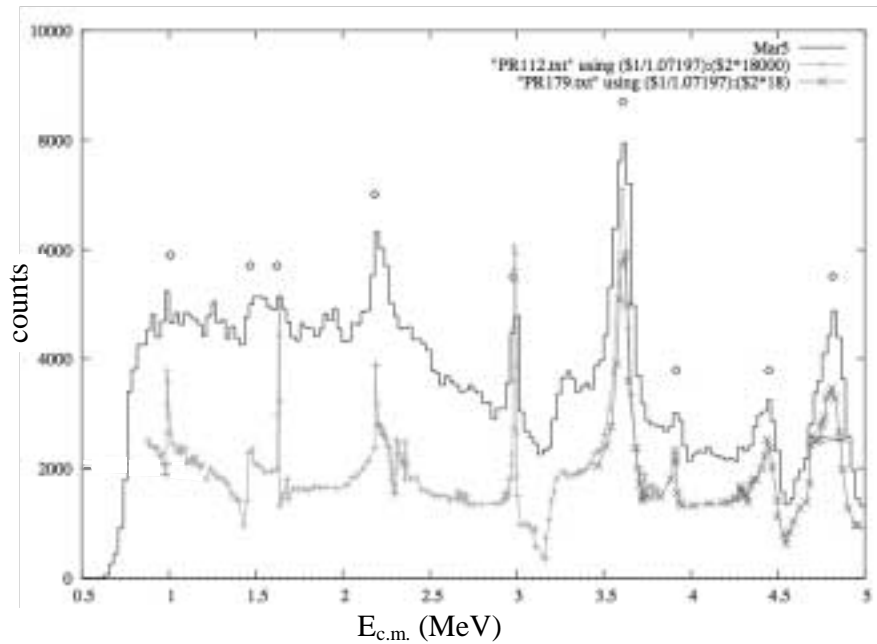


Fig. 6-3: The proton spectrum for the $\text{p}(^{14}\text{N},\text{p})^{14}\text{N}$ reaction. The solid line is from this experiment. The dash lines are from conventional kinematics: the lower energy data are from Olness *et al.* [Oln58], and the higher energy data are from West *et al.* [Wes69]. See text.

The features in the $^{14}\text{N}+\text{p}$ spectrum permitted a good linear calibration of the detector telescope energy. This calibration is accurate to about 15 keV in the center of mass frame over the entire energy range of from 1 to 5 MeV. However, a significant correction is required to use this calibration with $^{14}\text{O}+\text{p}$. The more rapid energy loss of ^{14}O in the degrader foil and target lead to interac-

tions occurring at a shallower depth, relative to the equivalent energy scattering by ^{14}N . Thus protons scattered by ^{14}O lose more energy as they emerge from the back of the target. The calculated energy loss corrections for ^{14}O and ^{14}N beams are displayed in Fig. 6-4.

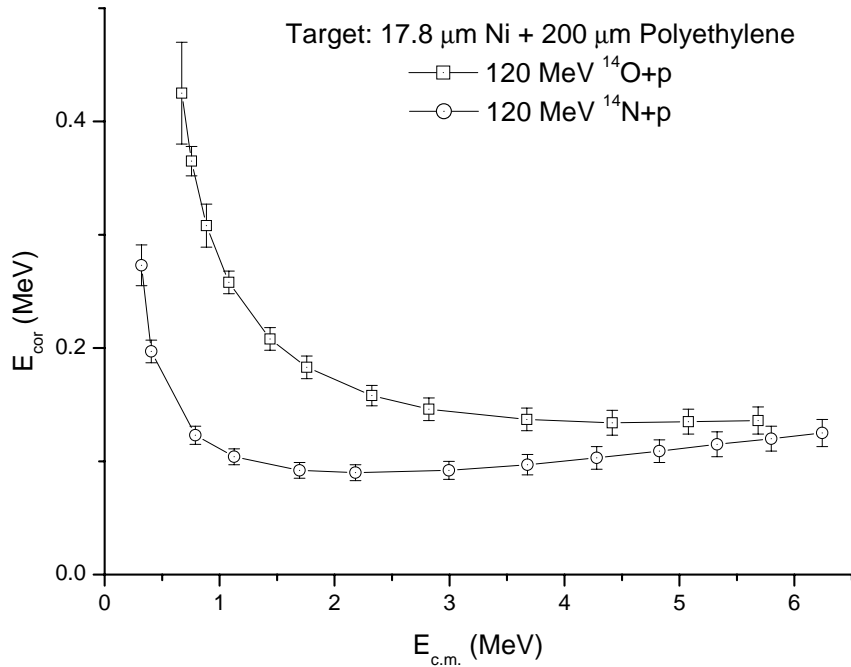


Fig. 6-4: The energy corrections for protons produced by two beams: 120 MeV ^{14}N and ^{14}O .

6.3 Results and Discussion

6.3.1 R-matrix Formalism

The $^{14}\text{O} + \text{p}$ data were fit with an R-matrix formalism [Lan58]. In this approach, the cross section, other than the Rutherford component, is expanded in terms of phase shifts for a spin 1/2 proton interacting with a spin 0 particle, as

described in [Lau51]. The differential elastic scattering cross section can be expressed with the following formula from [Lau51]

$$\frac{d\sigma}{d\Omega} = |A_1(\theta) + A_2(\theta)|^2 + |B(\theta)|^2 \quad (6-3)$$

where $\frac{d\sigma}{d\Omega}$ is the differential cross section, $A_1(\theta)$ is the Coulomb scattering, $A_2(\theta)$ is the nuclear scattering coherent with $A_1(\theta)$, and $B(\theta)$ is the incoherent nuclear scattering. They are expressed with these formulas:

$$A_1(\theta) = \frac{\eta\tilde{\lambda}}{2\sin^2(\theta/2)} e^{(-2i\eta)\ln[\sin(\theta/2)]} \quad (6-4)$$

$$A_2(\theta) = \frac{\tilde{\lambda}}{2i} \sum_{\ell=0}^{\infty} [(\ell+1)(e^{2i\delta_{\ell}^+} - 1) + \ell(e^{2i\delta_{\ell}^-} - 1)] e^{2i\omega_{\ell}} P_{\ell}(\cos \theta) \quad (6-5)$$

$$B(\theta) = \frac{\tilde{\lambda}}{2i} \sum_{\ell=0}^{\infty} (e^{2i\delta_{\ell}^+} - e^{2i\delta_{\ell}^-}) e^{2i\omega_{\ell}} P_{\ell}^1(\cos \theta) \quad (6-6)$$

Here $\eta = \left(\frac{e^2}{4\pi\epsilon_0} \right) \frac{zZ}{\hbar v}$ is the Sommerfeld parameter; $\tilde{\lambda} = \frac{\hbar}{\mu v}$, the reduced wave length; e , the electron charge; ϵ_0 , the permittivity of free space; z , the projectile charge; Z , the target charge; \hbar , the reduced Planck constant; v , the velocity of relative motion; μ , the reduced mass of the system; θ , the scattering angle; ℓ , the orbital angular momentum; δ_{ℓ}^+ and δ_{ℓ}^- , the parallel and antiparallel nuclear phase shifts; $P_{\ell}(\cos \theta)$, the Legendre polynomials; $P_{\ell}^1(\cos \theta)$, the first order associated Legendre polynomials; and ω_{ℓ} , the Coulomb phase shift with the expression:

$$\omega_\ell = \begin{cases} \sum_{m=1}^{\ell} \arctan\left(\frac{\eta}{m}\right) & \ell > 0 \\ 0 & \ell = 0 \end{cases} \quad (6-7)$$

Explicitly the $e^{2i\omega_\ell}$ is expressed in this way,

$$e^{2i\omega_\ell} = \begin{cases} \frac{\ell+i\eta}{\ell-i\eta} \frac{\ell-1+i\eta}{\ell-1-i\eta} \dots \frac{2+i\eta}{2-i\eta} \frac{1+i\eta}{1-i\eta}, & \ell > 0 \\ 1, & \ell = 0 \end{cases} \quad (6-8)$$

The nuclear phase shift for each partial wave is taken to be equal to a hard sphere phase plus a possible resonant term that may contain one or more states:

$$\delta_\ell^\pm = -\phi_\ell + \arctan \frac{P_\ell R_\ell^\pm}{1 - (S_\ell - b_\ell^\pm) R_\ell^\pm} \quad (6-9)$$

$$\phi_\ell = \arctan(F_\ell / G_\ell) \quad (6-10)$$

where ϕ_ℓ refers to the hard sphere phase shift, F_ℓ and G_ℓ are the regular and irregular Coulomb wave functions; δ_ℓ^+ and δ_ℓ^- again refer respectively to the partial waves with proton spin aligned parallel or antiparallel to the orbital angular momentum ℓ ; P_ℓ and S_ℓ are the energy dependent R-matrix penetration and shift factors; R_ℓ^\pm is a sum over resonance terms $\gamma_\lambda^2/(E_\lambda - E)$ representing levels of each partial wave with reduced widths γ_λ^2 ; and b_ℓ^\pm is the boundary constant. For cases where no more than one resonant term is required for each partial wave, the phase shift can be more simply expressed as:

$$\delta_\ell^\pm = -\phi_\ell + \arctan \frac{P_\ell \gamma_\lambda^2}{E_\lambda - E - (S_\ell - b_\ell^\pm) \gamma_\lambda^2} \quad (6-11)$$

The formal R-matrix state parameters, E_λ and γ_λ^2 , depend on the arbitrary boundary constant for that partial wave. Following the standard convention, the boundary constant is set to be equal to the shift function at the state energy, $b_\ell^\pm = S_\ell(E_\lambda)$; with this choice, E_λ is defined as the “observed” resonance energy. To define an “observed” resonance width that is independent of energy, the penetration factor is approximated by its value at the state energy $P_\ell(E_\lambda)$, and the $S_\ell - S_\ell(E_\lambda)$ term is approximated by a series expansion about $E = E_\lambda$, keeping only the first non-zero term, $(E - E_\lambda) dS/dE|_{E=E_\lambda}$, leading to:

$$\delta_\ell^\pm \approx -\phi_\ell + \arctan \frac{\frac{1}{2} \Gamma_\lambda}{E_\lambda - E} \quad (6-12)$$

where the “observed” width is defined as

$$\Gamma_\lambda = \frac{2P_\ell \gamma_\lambda^2}{1 + \gamma_\lambda^2 dS/dE} \Big|_{E=E_\lambda} \quad (6-13)$$

An additional important R-matrix parameter is the channel radius, which defines the “hard sphere” as well as the penetration and shift factors. We normally take this to be a simple estimate for $^{14}\text{O} + \text{p}$: $1.25(A^{1/3} + 1)$ with $A=14$. However, it can also be varied as a free parameter.

6.3.2 Results

The results of two runs of 120 MeV ^{14}O on hydrogen are shown in Fig. 6-5. The yield from each run has been divided by the energy loss of ^{14}O per unit thickness, dE/dx , in order to produce an excitation function. The first run in March 2003 was on a 17.8 μm nickel degrader and a 200 μm polyethylene tar-

get; the calibration of this run used the ^{14}N data of Fig. 6-3, as modified by a calculated correction for the different energy loss (see Fig. 6-4).

The second run, (performed in October 2003), differed by having a thinner 14 μm nickel degrader. Unfortunately, detector and electronics problems prevented the determination of a good calibration spectrum for this run. Instead, the calibration was only determined by matching (with very poor statistics) to the two largest peaks in the $^{14}\text{N} + ^1\text{H}$ spectrum, leading to an energy uncertainty of about 50 keV in the lower energy range. Despite this uncertainty, the shape of the two runs is very similar. The second run also exhibits what appears to be a higher background at higher energies. This may reflect beam contaminants.

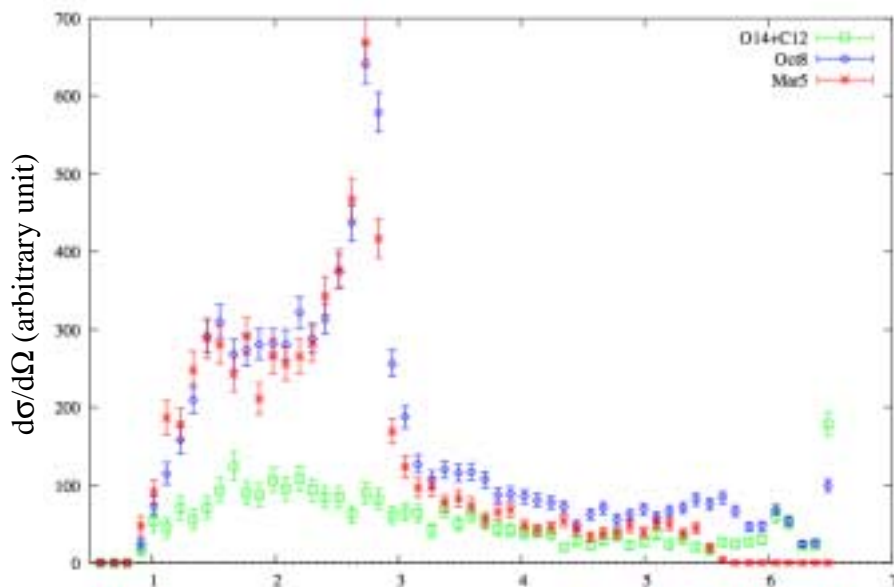


Fig. 6-5: The excitation functions for two p($^{14}\text{O},\text{p}$) ^{14}O runs. Also as protons from $^{12}\text{C} + ^{14}\text{O}$ reaction. The sharp “peak” in around 6.5 MeV is due to ADC overflow.

A background run is also shown in Fig. 6-5, for a 14 μm nickel degrader backed by a 28.0 mg/cm^2 carbon foil. This spectrum has been nominally energy calibrated and analyzed in the same way as the second $^{14}\text{O}+\text{p}$ run. The overall yield has been determinated using estimates of the ^{14}O beam intensity during these runs; this is accurate to only about 50%. The energy calibration should also include a different correction to account for the different target. However, since the background is a smooth featureless function, precise calibration is unnecessary.

The background from $^{14}\text{O}+\text{carbon}$ has been subtracted from the first $^{14}\text{O}+\text{polyethylene}$ run, thus producing an excitation function for elastically scattered protons on ^{14}O . This is displayed in Fig. 6-6, and is preferentially used in the analysis because of its superior energy calibration.

The $^{14}\text{O}+\text{p}$ scattering excitation function was fit with two R-matrix resonances, a $1/2^+$ ground state ($\ell=0$) and a $5/2^+$ first excited state ($\ell=2$). The fit is shown in Fig. 6-6. Because of possible background at higher energies, the fit is made only between 1 MeV and 3.2 MeV. The fit has been convoluted with an estimated experimental resolution of 50 keV, in the center of mass frame, though the exact resolution has little effect on the fit. Also shown are the separate contributions from each state, calculated by setting the other state to zero.

Table 6-1 lists the best overall fit parameters.

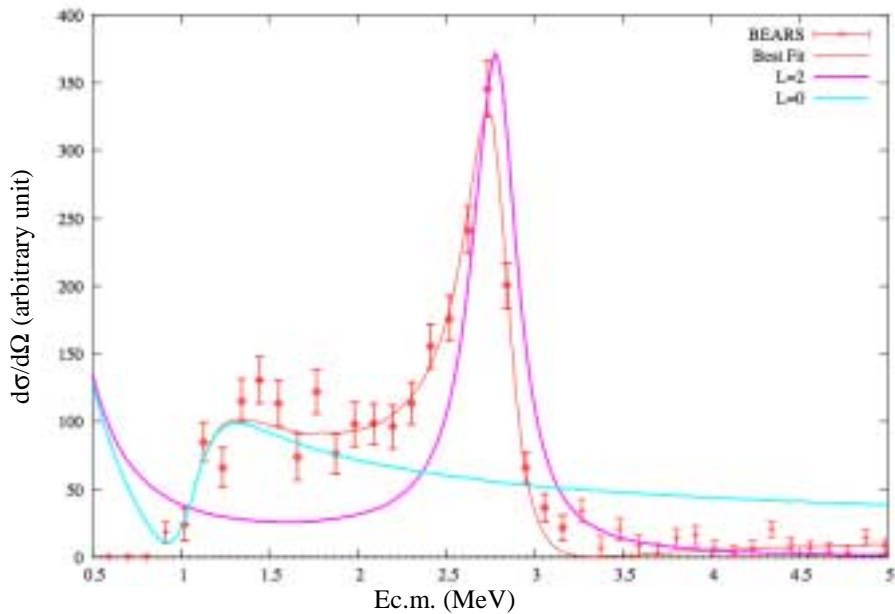


Fig. 6-6: The final excitation function and fitted curves.

Table 6-1: The R-matrix parameters for ^{15}F from $\text{p}(^{14}\text{O}, \text{p})^{14}\text{O}$.

$E_{1/2+}$	1.23 ± 0.05 MeV
$\Gamma_{1/2+}$	0.5-0.84 MeV
$E_{5/2+}$	2.81 ± 0.02 MeV
$\Gamma_{5/2+}$ (observed)	0.30 ± 0.06 MeV
Channel radius	4.26 fm
$\chi^2/\text{degrees of freedom}$	27.9/16

The channel radius, used in defining the R-matrix hard sphere phase shift and penetration factors, was set equal to 4.26 fm, corresponding to $1.25(A^{1/3}+1)$ for $^{14}\text{O}+\text{p}$. If allowed to be a free parameter, it was found to fit at 4.59 fm with a slightly better χ^2 of 26.8, and overall it lay within a range of roughly 3.5-5.5 fm. Variation in this range did not produce changes in the best fit parameters larger than the uncertainties given in Table 6-1. Varying the angle

used in the fitting, from $\theta_{\text{cm}}=180^\circ$ down to 170° , the maximum angular range of the detector, also produced only small changes in the parameters.

Due to the uncertainty in the exact amount of ^{14}O +carbon background to subtract, this correction was varied by plus or minus 50% to investigate its effect on the best fit parameters. This is incorporated into the errors given in table 6-1, as are uncertainties in the energy calibration.

Other spin assignments were investigated. The only one giving a possible, though poorer, fit was assigning the first excited state to be $3/2^+$, the other $\ell=2$ possibility. This fit was notably worse than with the preferred assignment of $5/2^+$, giving a best χ^2 of 39.2 versus 27.9. Good fits could not be obtained with other choices of the angular momentum.

The excitation function was measured up to about 5 MeV, and there is no evidence of further resonances. However, the R-matrix calculations show that scattering from a ^{15}F mirror analogue of the $1/2^-$ second excited state in ^{15}C at 3.103 MeV would have only a relatively small effect, and such a state could easily be hidden in the data. Better understanding and control of the background would be needed to identify or exclude such a state.

A comment should be made on the observed width of the broad $\ell=0$ ground state. As seen from the definition of the observed width in Equation 6-13, for large values of $\gamma_\lambda^2 dS/dE$, the observed width reaches a maximum of $2P_\ell(dS/dE)^{-1}$, independent of the reduced width. This limit is 0.84 MeV for the ground state. Near this limit, the behavior of the partial wave is determined

mainly by the energy dependence of the penetration and shift functions, and by interference with the Rutherford scattering component. The best fit occurs at this limit, but reasonable fits are obtained for observed widths down to about 0.5 MeV.

6.4 Discussion

6.4.1 Comparison

These data can be compared with two other recent measurements of the $^{14}\text{O} + \text{p}$ spectrum. Figure 6-7 displays the final excitation function of a National Superconducting Cyclotron Laboratory (NSCL) at Michigan State University group [Pet03], as well as the fitted result for $\theta_{\text{cm}}=180^\circ$ from a Texas A & M University group [Gol04] (this fit is also based on data at other angles, but it reasonably describes the 180° data in that work). Also plotted is the R-matrix fit from Fig. 6-6.

There is disagreement among the three experiments. Our results agree reasonably well with Ref. [Gol04] as to the shape and position of the excited state, while showing systematic disagreements with the data of Ref. [Pet03]. The current work disagrees with both previous measurements as to the position of the leading edge of the ground state resonance, placing this edge roughly 150 keV lower. This shift is larger than can be accounted for by the estimated energy uncertainties.

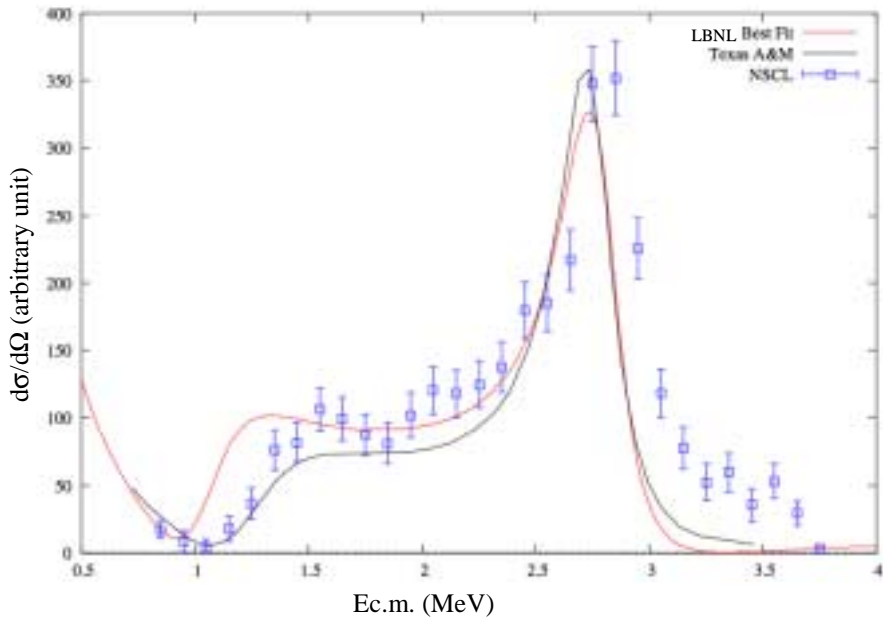


Fig. 6-7: The comparison of results from three different labs using the same $\text{p}(^{14}\text{O}, \text{p})^{14}\text{O}$ reaction.

Comparisons to past results for ^{15}F [Lep03, Pet03, Kek78, Ben78, Gre97, Gol04], which are summarized in Table 6-2, are complicated by the various possible definitions of the excitation energy and width of the broad states. In many cases, the relevant energy comparison is to the point of maximum cross section, which for the current work is 1.33 ± 0.08 and 2.73 ± 0.03 MeV for the ground state and first excited state, respectively. Note the shift from the R-matrix values even for the narrower excited state, due to interference with the ground state. With the appropriate quantities compared, the current measurement is in general agreement with past work.

Table 6-2: Comparison of the results for the energy levels of ^{15}F .

Level	$J^\pi; T$	Ref.	E_x (MeV)	$\Gamma_{\text{c.m.}}$ (MeV)
g.s.	$1/2^+; 3/2$	[Ben78]	1.6 ± 0.2	≥ 0.9
		[Kek78]	1.37 ± 0.18	0.8 ± 0.3
		[Gre97] *	1.2	0.5
		[Lep03]	1.41 ± 0.15	0.8 ± 0.3
		[Pet03]	$\sigma_{\text{max}}(\delta^{90^\circ})$	1.51 ± 0.11 (1.47)
			Ψ_{max}	1.29
		[Gol04]	$\sigma_{\text{max}}(\delta^{90^\circ})$	$1.45^{+0.16}_{-0.10}$
			Ψ_{max}	$1.29^{+0.08}_{-0.06}$
		This	$\sigma_{\text{max}}(\delta^{90^\circ})$	1.33
		work:	$E_{1/2^+}(\text{Obs.})$	1.23 ± 0.05
1^{st} e.s.	$5/2^+; 3/2$	[Ben78]	2.8 ± 0.2	0.24 ± 0.03
		[Kek78]	2.67 ± 0.1	0.5 ± 0.2
		[Gre97] *	2.4	0.2
		[Lep03]	2.54 ± 0.07	0.27 ± 0.07
		[Pet03]	$\sigma_{\text{max}}(\delta^{90^\circ})$	2.853 ± 0.045
			Ψ_{max}	2.85
		[Gol04]	$\sigma_{\text{max}}(\delta^{90^\circ})$	2.795 ± 0.045
			Ψ_{max}	2.795 ± 0.045
		This	$\sigma_{\text{max}}(\delta^{90^\circ})$	2.73 ± 0.03
		work:	$E_{5/2^+}(\text{Obs.})$	2.81 ± 0.02

* Theoretical estimation.

6.4.2 Isobaric Multiplet Mass Equation of $T=3/2$, $A=15$

The quadratic isobaric multiplet mass equation (IMME) predicts the mass M of a multiplet member as:

$$M(A, T, T_z) = a(A, T) + b(A, T)T_z + c(A, T)T_z^2 \quad (6-14)$$

where M is the mass of a multiplet member, A , T , and T_z the mass number, isospin, and the projection of T , and a , b , and c are parameters. The analog masses for the $T=3/2$, $J^\pi=1/2^+$ state in ^{15}F found in ^{15}C and ^{15}N are 9873 ± 0.9 and 11716 ± 4 keV. The $T=3/2$, $J^\pi=1/2^+$ state for ^{15}O has not been experimentally

assigned. There was a tentative assignment of the 11151 ± 7 keV (unknown J^π) level to a $T=3/2$ state in ^{15}O with systematics from the analog $T=3/2$, $J^\pi=1/2^+$, 16770 ± 130 keV ($E_{\text{ex}}=1.47 \pm 0.13$ MeV) state of ^{15}F [Ant88]. Two other states in ^{15}O , at 10938 ± 3 and 11025 ± 3 , were not selected. However, with the new $E_{\text{ex}}=1.23 \pm 0.05$ MeV, for this state, the assignment may be problematic.

Table 6-3: The IMME fitting parameters for $J^\pi=1/2^+$, $T=3/2$ in ^{15}O with different values for the ^{15}F ground state.

E_{ex} of ^{15}F (MeV) $T=3/2$, $J^\pi=1/2^+$	Assumed analog level of ^{15}O (keV)	A (keV)	b (keV)	c (keV)	d (keV)	χ^2/n
1.23 ± 0.05						
This work	10938 ± 3	12721 ± 3	-2089 ± 5	127 ± 4		65.3
		12699 ± 4	-2059 ± 6	223 ± 13	-70 ± 9	
	11025 ± 3	12756 ± 3	-2168 ± 5	164 ± 4		9.51
		12748 ± 4	-2157 ± 6	201 ± 13	-27 ± 9	
	11151 ± 7	12804 ± 4	-2276 ± 7	215 ± 5		15.3
		12819 ± 6	-2299 ± 8	169 ± 13	36 ± 9	
1.47 ± 0.13						
[Ant88]	10938 ± 3	12724 ± 3	-2080 ± 4	119 ± 3		25.9
		12684 ± 6	-2049 ± 7	284 ± 23	-111 ± 16	
	11025 ± 3	12757 ± 3	-2166 ± 5	162 ± 4		9.58
		12733 ± 9	-2147 ± 8	262 ± 33	-68 ± 22	
	11151 ± 7	12805 ± 4	-2290 ± 8	224 ± 5		0.0417
		12803 ± 9	-2289 ± 11	230 ± 33	-5 ± 22	

As shown in Table 6-3, which considers all three ^{15}O states, the χ^2/n for both the 11151 keV level and the 11025 keV level is large; neither of them is consistent with the IMME parameters. When referring back to reference [Ajz91], these two states (11151 keV and 11025 keV) are populated by one of these reactions: $^{12}\text{C}(^6\text{Li},t)^{15}\text{O}$, $^{14}\text{N}(p,\gamma)^{15}\text{O}$, $^{14}\text{N}(p,p)^{14}\text{N}$, and $^{16}\text{O}(^3\text{He},\alpha)^{15}\text{O}$. None of these reac-

tions will populate $T=3/2$ states in ^{15}O . A χ^2 fit to the analog masses of ^{15}C , ^{15}N , and ^{15}F (1.23 MeV) ($T=3/2$, $J^\pi=1/2^+$) gave the following results:

$$a = 12778 \pm 8 \text{ keV}, b = -2218 \pm 17 \text{ keV}, c = 187 \pm 9 \text{ keV}$$

From these coefficients, the calculated analog mass of ^{15}O ($T_z=-1/2$) is 13934 keV, and the deduced analogue level of ^{15}O would be around 11079 keV.

6.4.3 Thomas-Ehrman Shift

Because of the charge independence of the strong nuclear force, the wave functions and energy levels of isobaric multiplets are nearly identical. Hence, these analog states are usually used to estimate the level structures of unknown proton rich exotic nuclei from their mirror partners. However, near the doubly magic nuclide ^{16}O , there is a large discrepancy between the low lying analog states of mirror nuclei. For example, the $1/2^+$ first excited state of ^{13}N is 720 keV lower than its analog state in ^{13}C . This effect is called the Thomas–Ehrman shift (TES).

The TES has been conventionally treated as an effect of the Coulomb interaction between a loosely bound or unbound $s_{1/2}$ proton with the relatively tightly bound core. In light nuclei, frequently the last proton in the proton rich member of a mirror pair is unbound or very loosely bound. In this case, the proton has a larger probability to tunnel through the barrier and give a broad radial distribution. The effect is especially pronounced if the proton is in an s-shell, so there is no centrifugal barrier and the proton wavefunction can stretch far out. This will reduce the Coulomb energy which has a $1/r$ dependence, and the state appears at lower energy than the analog state for a valence neutron [Mar01].

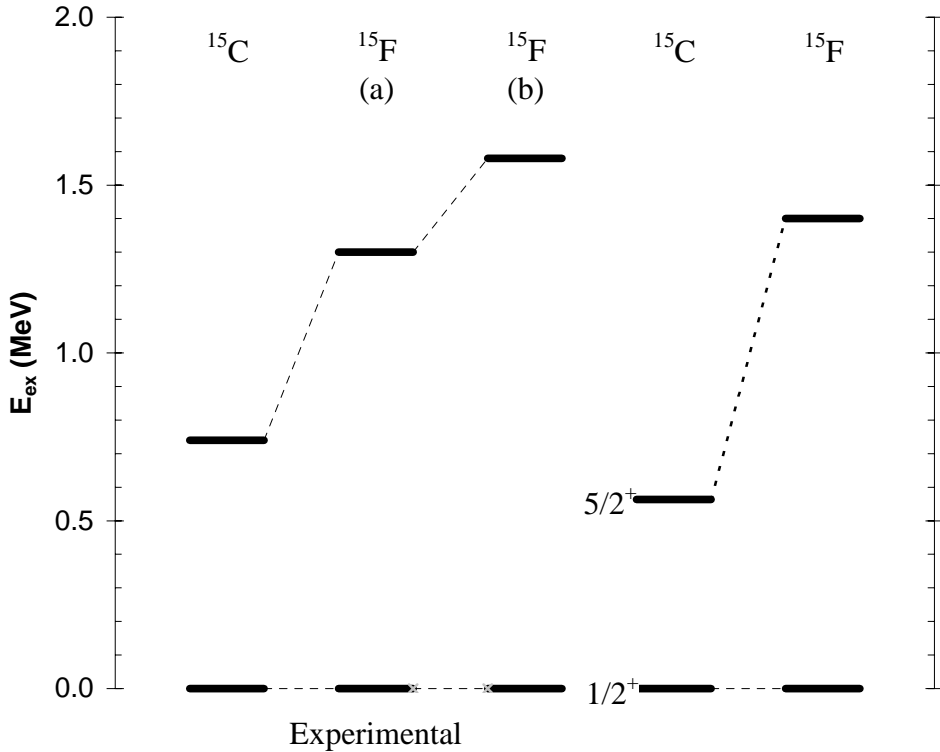


Fig. 6-8: TES: Experimental and calculated energy levels of the $^{15}\text{C} - ^{15}\text{F}$ mirror nuclei [Oga99]. (a) Data from [Ajz91], $E_{\text{ex}} = 1.30$ MeV; (b) Data from this thesis, $E_{\text{ex}}=1.58$ MeV.

Recently, it has been argued whether this mechanism is sufficient to account for the TES in various mirror nuclei [Oga99]. With a phenomenological method focusing on effects of the residual nuclear interaction (RNI) on the TES, the energies of the low-lying $1/2^+$ and $5/2^+$ levels of ^{15}C and ^{15}F ($T_z=\pm 3/2$) have been calculated in the $(0p_{1/2})^{-2} \otimes (0d_{5/2}1s_{1/2})^1$ model space. Figure 6-8 shows the calculated energy levels together with the experimental data from reference [Ajz91] and from this thesis. Experimentally, it has been known that level inversion occurs (when compared to the simple shell model), thus the $1/2^+$ states,

instead of the $5/2^+$ states, lie lowest in both nuclei. This inversion can be reproduced by the shell model Hamiltonian [Oga99], due to the stronger repulsion between $0p_{1/2}^{-1}$ and $0d_{5/2}$ than between $0p_{1/2}^{-1}$ and $1s_{1/2}$.

This RNI shell model yields $E_{\text{ex}}(5/2^+) = 0.563$ MeV for ^{15}C and 1.40 MeV for ^{15}F . The $5/2^+$ level is observed at $E_{\text{ex}} = 0.74$ MeV in ^{15}C , and at 1.30 MeV from the adopted value [Ajz91] or 1.58 MeV from our data in ^{15}F . The TES in the $^{15}\text{C}-^{15}\text{F}$ pair is thus described with reasonable accuracy within the framework of the phenomenological shell model. A large discrepancy is found in $E(1/2^+)$ of ^{15}C , which is overestimated by 0.176 MeV [Oga99]. If we take the $E_{\text{ex}} = 1.58$ MeV for ^{15}F , it seems that the calculated $E(1/2^+)$ of ^{15}F is overestimated by 0.180 MeV.

6.4.4 Disappearance of the Magic Number Effect

The magic number phenomenon in the valley of the stable isotopes reflects the shell closures of nuclei [Kra88c]. When experiments probe nuclei toward and beyond the dripline, the magic numbers may disappear and new magic numbers may emerge [Nav00- Oza00, Pet03, Tho03].

The systematics of neutron and proton separation energies can be powerful tools for studying nuclear structure at and even beyond the driplines. There is evidence showing the disappearance of the $N=8$ shell closure when close to the neutron dripline [Tho01, Tho03, Pet03]. The vanishing of the $N = 8$ shell close to the dripline can be observed in the systematics of single neutron separation energies for nuclei with a given isospin as a function of neutron number (see Fig. 6-9a). At shell closures the neutron separation energy shows

a sharp drop between adjacent nuclei. The absence of this sharp decrease indicates the disappearance of a shell, as is seen in Fig. 6-9a for nuclei with $T_z=3/2$.

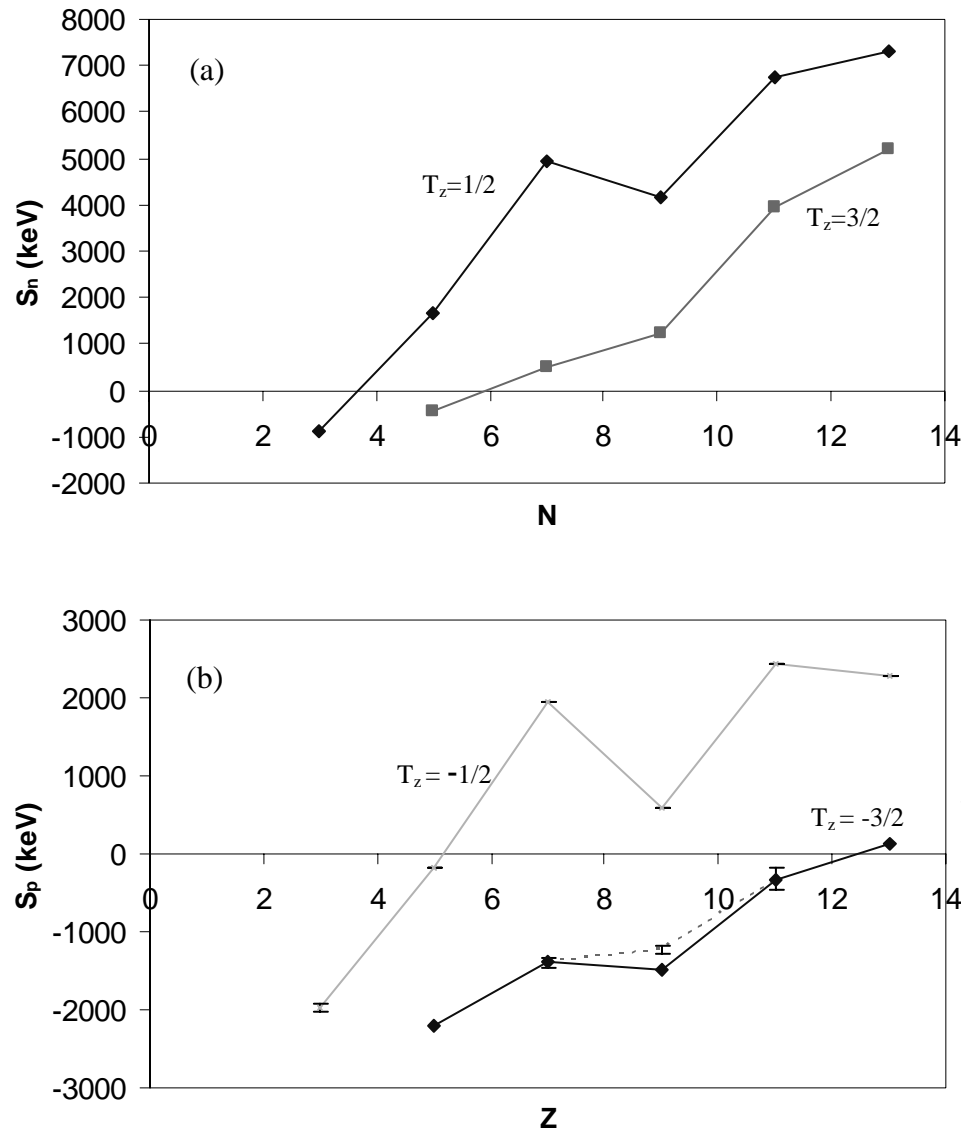


Fig. 6-9: Single-nucleon separation energies. (a) S_n for neutron rich $T_z=1/2$ and $T_z=3/2$ nuclei. The $N=8$ shell closure has clearly disappeared for the $T_z=3/2$ nuclei. (b) S_p for proton-rich $T_z=-1/2$ and $T_z=-3/2$ nuclei. See text.

Similarly, proton separation energies can be used to study proton shell closures. It is arguable whether the disappearance of the $Z=8$ shell closure happens when close to the proton dripline. Figure 6-9b shows the single proton separation energies for odd Z , even N nuclei with isospin $-1/2$, and $-3/2$. The $T_z=-1/2$ shell closure is clearly seen. Two different proton separation energies for ^{15}F are shown in this figure for the $T_z=-3/2$ nuclei: -1.23 MeV (dash line) from this work and -1.48 MeV (solid line) from the most recent compilation [Aud03]. For $T_z = -3/2$ nuclei, it depends on which S_p for ^{15}F is chosen, whether the (small) discontinuity vanishes. Our data would indicate the disappearance of the $Z = 8$ shell for proton-rich nuclei which are beyond the dripline.

6.5 Summary

Since the first successful delivery of ^{14}O as a radioactive ion beam, several $^{14}\text{O}+\text{p}$ runs have been performed. Excellent energy calibration can be obtained using $^{14}\text{N}+\text{p}$ in inverse kinematics and comparing the results to those obtained earlier with normal kinematics. The differences between $^{14}\text{N}+\text{p}$ and $^{14}\text{O}+\text{p}$ in the stopping power function have been evaluated for better energy calibration. After careful calibration, the energy levels of ^{15}F were fitted with an R-matrix calculation. Spins and parities were assigned to the two observed resonances. This new measurement of the ^{15}F ground state supports the disappearance of the $Z = 8$ proton magic number for odd Z , $T_z=-3/2$ nuclei.

C H A P T E R 7

SUMMARY AND FUTURE WORK

7.1 Summary

As discussed in previous chapters, radioactive ion beams have been shown to be a useful tool for studying proton-rich nuclides near and beyond the proton dripline and for evaluating nuclear models. RIBs bring unprecedented opportunities to nuclear physics and astrophysics. The RIBs facilities, either with the projectile fragmentation method or the ISOL method, or a hybridization of both, are providing or are going to provide exciting results for our improved understanding of nuclear matter.

To take full advantage of radioactive ion beams, an experimental method, elastic resonance scattering in inverse kinematics with thick targets, has been intensively discussed and proven to be a reliable tool for investigations of proton unbound nuclei. ERSIKTT offers an economical but still good-quality method to utilize the present, low-intensity, RIBs.

Following several years of effort, BEARS, a radioactive ion beam capability, has been developed at the LBNL 88-Inch Cyclotron. The current BEARS provides two radioactive ion beams: a ^{11}C beam of up to 2×10^8 pps intensity and an ^{14}O beam of up to 3×10^4 pps intensity. While the development of the ^{11}C beam has been relatively easy, a number of challenges had to be overcome to obtain the ^{14}O beam. It is hoped that the planned development of an ^{15}O beam will be easier, since it utilizes the technology developed for the ^{14}O beam.

The excellent ^{11}C beam has been used to investigate a few reactions. The first was the $^{197}\text{Au}(^{11}\text{C},xn)^{208-xn}\text{At}$ reaction, which was used to measure excitation functions for the $4n$ to $8n$ exit channels. The measured cross sections were generally predicted quite well using the fusion-evaporation code HIVAP. Possible errors in the branching ratios of α decays from At isotopes as well as the presence of incomplete fusion reactions are probably contributing to specific overpredictions. To investigate the overpredictions of the yield for even-neutron final nuclei, a more detailed comparison of our data to the code still needs to be performed. Further ^{11}C studies are discussed below.

^{15}F has been investigated by the $p(^{14}\text{O},p)^{14}\text{O}$ reaction with ERSIKTT technology. Several $^{14}\text{O}+p$ runs have been performed. Excellent energy calibration was obtained using resonances from $p(^{14}\text{N},p)^{14}\text{N}$ in inverse kinematics, and comparing the results to those obtained earlier with normal kinematics. The differences between $^{14}\text{N}+p$ and $^{14}\text{O}+p$ in the stopping power function have been evaluated for better energy calibration. After careful calibration, the energy levels of ^{15}F were fitted with an R-matrix calculation. Spins and parities were as-

signed to the two observed resonances. This new measurement of the ^{15}F ground state supports the disappearance of the $Z = 8$ proton magic number for odd Z , $T_z = -3/2$ nuclei.

It is expected that future work on proton-rich nuclides will rely heavily on radioactive ion beams and/or mass separators. At the current time, radioactive ion beam intensities are sufficient for the study of a reasonable number of very proton-rich nuclides.

7.2 Outlook

Research is an ongoing process. Besides the work mentioned above, several additional projects have used or will utilize the ^{11}C and ^{14}O radioactive ion beams. Using the ^{11}C beam, the $^{11}\text{C}(\text{d},\text{n})^{12}\text{N}$ reaction has been investigated to extract its direct interaction cross section, which plays a significant role in the production of ^{12}C nuclei for the CNO cycle of p-p burning: $^7\text{Be}(\alpha,\gamma)^{11}\text{C}$ or $^8\text{B}(\alpha,\text{p})^{11}\text{C}$, and $^{11}\text{C}(\text{p}, \gamma)^{12}\text{N}$. For the ^{14}O beam, a few unique experiments have been proposed, such as using the $^3\text{He}(^{14}\text{O},\text{t})^{14}\text{F}$ reaction to study the unknown exotic nuclide ^{14}F and the $^{14}\text{O}(\alpha,2\text{p})^{16}\text{O}$ reaction to search for two-proton radioactivity.

Two-proton radioactivity, the spontaneous breakup of elements with emission of two protons, was predicted to exist near the proton drip line by Goldansky in the sixties [Gol60]. A two-proton decay may proceed either via ^2He emission or by the simultaneous emission of two protons which are uncor-

related in space (direct three-body decay with no final state interactions). For those nuclei considered to be candidates for 2p radioactivity, one-proton emission is forbidden in terms of energy conservation. A two-proton decay mode has been postulated for ${}^6\text{Be}$ [Gee77, Boc92] and for ${}^{12}\text{O}$ [Kry95]. Although for these light nuclei, the centroid of the intermediate one-proton daughter state may lie higher in energy than the two-proton emitting state, a sequential two proton decay branch is always found to be open, because all the states involved are very broad as a consequence of the small Coulomb barrier for these light nuclei.

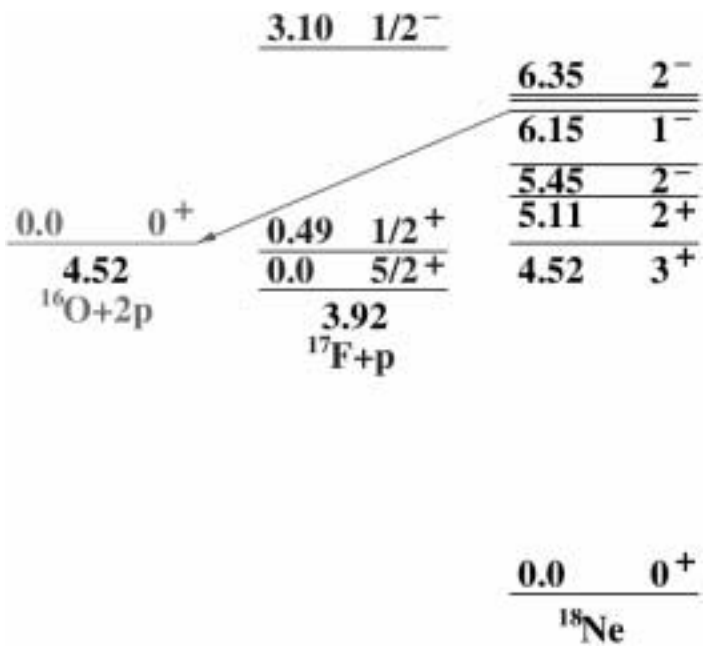


Fig. 7-1: Decay scheme of ${}^{18}\text{Ne}$. Spins and parities taken from Ref. [Góm01].

Recent experimental efforts have focused on the observation of direct two-proton decay. There have been experiments showing indirect evidence for two-proton decay of ${}^{45}\text{Fe}$ [Gio02, Pfü02] and correlated two-proton (${}^2\text{He}$) decay

from a 6.15 MeV $J^\pi = 1^-$ excited state of ^{18}Ne [Góm01]. In the latter case, the 6.15 MeV $J^\pi = 1^-$ excited state of ^{18}Ne was populated by $^{17}\text{F} + \text{p}$. These authors have explored what appears to be a unique example in light nuclei where sequential two-proton emission is not possible. Hence, the only mechanisms for two-proton emission which are possible are ^2He emission or simultaneous uncorrelated emission. The decay scheme is illustrated in Fig. 7-1, which is taken from Gómez del Campo *et al.* [Góm01]. Unfortunately, as they report, their "energy and angular distribution data do not distinguish between the[se] two extreme decay mechanisms."

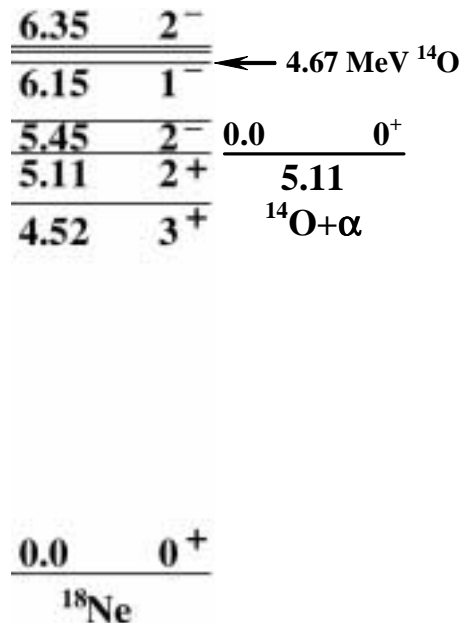


Fig. 7-2: Population of the 6.15 MeV 1^- resonance in ^{18}Ne with 4.67 MeV ^{14}O .

The results in [Góm01] have been criticized by Grigorenko *et al.* [Gri01, Gri02]. The conclusion from [Gri01, Gri02] is that the two-proton decay of the 1^- state is sufficient to explain only a small fraction of the events reported in the reference [Góm01]. It is plausible that the balance of the observed 2p events is connected either with (i) excitation of a 2^- state located a little higher than the 1^- state or with (ii) the breakup of ^{17}F . For example, the breakup of ^{17}F induced by proton in the target could be an important source of two-proton events.

An alternate experiment with a goal to remove these uncertainties is to study the two-proton decay of the ^{18}Ne 6.15 MeV, 1^- , resonance populated by the $^{14}\text{O} + ^4\text{He}$ reaction at 4.67 MeV (see Fig. 7-2). Using the $^{14}\text{O} + ^4\text{He}$ reaction prohibits population of the 2^- state since it is spin-parity forbidden, and it also precludes significant break-up of the projectile due to the greater proton binding energy of ^{14}O (4.6 MeV). Hence it may be possible to observe an unambiguous signature of the two-proton decay mode of the 6.15 MeV, 1^- state in ^{18}Ne , which lies at 1.04 MeV c. m. in the $^{14}\text{O} + ^4\text{He}$ reaction.

L I S T O F

REFERENCES

Aj z91, F. Ajzenberg-Selove, Nucl. Phys. A 523 (1991) 1.

Al o84, J. Alonso and G. Krebs, Lawrence Berkeley Laboratory Report No. LBL-17829 (1984) unpublished.

Al o89, J. R. Alonso, B. Feinberg, and J.G. Kalnins, Lawrence Berkeley Laboratory Report No. LBL-28114 (1989) unpublished.

Ant88, M. S. Antony and J. Britz, Indian. J. Phys. 62A (1988) 411-414.

Art90, K. P. Artemov, O. P. Belyanin, A. L. Vetoshkin, R. Wolskj, M. S. Golovkov, V. Z. Gol'dberg, M. Madeja, V. V. Pankratov, I. N. Serikov, V. A. Timofeev, V. N. Shadrin, and J. Szmider, Soviet Journal of Nuclear Physics 52 (1990) 408-411.

Aud03, G. Audia, A.H. Wapstra, and C. Thibault, Nuclear Physics A 729 (2003) 337–676.

Aus68, P. Ausloos, ed., Fundamental Processes in Radiation Chemistry, John Wiley and Sons, New York (1968).

References

Bab88, S. Baba, K. Hata, S. Ichikawa, T. Sekine, Y. Nagame, A. Yokohama, M. Shoji, T. Saito, N. Takahashi, H. Baba, and I. Fujiwara, *Z. Phys. A* 331 (1988) 53.

Bak92, O. K. Baker, P. Ford, D. Holder, W. Naing, and A. Weisenberger, in *The Vancouver Meeting: Particles and Fields '91*, World Scientific, Singapore, D. Axen *et al.* eds., vol. 2 (1992) 1132-4.

Bar97, D. W. Bardayan and M. S. Smith, *Phys. Rev. C* 56 (1997) 1647.

Ben78, W. Benenson, E. Kashy, A. G. Ledebuhr, R. C. Pardo, R. G. H. Robertson, and L. W. Robinson, *Physical Review C* 17 (1978) 1939-1942.

Ben93, S. J. Bennett, N. M. Clarke, M. Freer, B. R. Fulton, S. J. Hall, O. Karban, J. T. Murgatroyd, G. Tungate, G. J. Gyapong, N. S. Jarvis, D. L. Watson, W. D. M. Rae, A. E. Smith, J. S. Lilley, P. J. Woods, R. D. Page, *Nuclear Instruments & Methods in Physics Research Section A* 332 (1993) 476-482.

Ber93, M. S. Berger, ed., *Stopping Powers and Ranges for Protons and Alpha Particles*, ICRU Report 49, International Commission on Radiation Units and Measurements (1993).

Bi e91, A. Bielansk and J. Haber, *Oxygen in Catalysis*, Marcel Dekker, New York (1991) 114.

Bi m68, R. Bimbot, M. Lefort, and A. Simon, *J. Phys.* 29 (1968) 563.

Bl a82, M. Blann and J. Bisplinghoff, LLNL Report No. UCID-19614 (1982)

(unpublished).

Boc92, O. V. Bochkarev, A. A. Korsheninnikov, E. A. Kuz'min, I. G. Mukha, L. V. Chulkov, and G. B. Yan'kov, Sov. J. Nucl. Phys. 55 (1992) 955-969.

Boh36, N. Bohr, Nature 344 (1936) 137.

Bon67, J. P. Bondorf, in Proceedings of the International Symposium on Nuclides far off the Stability Line, Lysekil, Sweden, August 21–27, 1966, W. Forsling, C. J. Herrlander, and H. Ryde, eds.; Arkiv Fysik 36 (1967) 681

Bri 98, J. Britz, Atomic Data and Nuclear Data Tables 69 (1998) 125-159.

Cab82, M. D. Cable, J. Honkanen, R. F. Parry, H. M. Thierens, J. M. Wouters, Z. Y. Zhou, and J. Cerny, Phys. Rev. C 26 (1982) 1778-1780

Cas00, R. F. Casten, Nuclear Structure from a Simple Perspective, Oxford University Press, New York (2000) 418. Also see the 1997 Columbus “White Paper Report”: *Scientific Opportunities with an Advanced ISOL Facility* which is based on a workshop held at Columbus, Ohio, on the “Science for an Advanced Radioactive Beam Facility of the Two-accelerator ISOL-type.”

Cas95, R. Casten, J. D'Auria, C. Davids, J. Garrett, M. Nitschke, B. Sherrill, D. Vieira, M. Wiescher, and E. Zganjar, Overview of Research Opportunities with Radioactive Nuclear Beams: An update -- 1995 (1995).

References

Cer96, J. Cerny, in Proceedings of the Exotic Nuclei Symposium, Bodega Bay, CA (1996), D. Moltz, ed., Lawrence Berkeley Laboratory Report No. LBNL Report-39750 (1996).

Cer99a, J. Cerny, F. Guo, R. Joosten, R.M. Larimer, C.M. Lyneis, M.A. McMahan, E.B. Norman, J. O'Neil, J. Powell, M. Rowe, H. VanBrocklin, D. Wutte, Z.Q. Xie, X.J. Xu, and P. Haustein, in Proceedings of the 1999 Particle Accelerator Conference (Cat. No.99CH36366), Piscataway, NJ, 1999, IEEE. Part vol.1 (1999) 533-535.

Cer99b, J. Cerny, American Institute of Physics Conference Proceedings 518 (2000) 3-13.

Che70, E. Cheifetz, R. C. Gatti, R. C. Jared, S. G. Thompson, and A. Wittkower, Phys. Rev. Lett. 24 (1970) 148–152.

Cl a83, D. J. Clark, J. G. Kalnus, and C. M. Lyneis, Proceedings of the Particle Accelerator Conference on Accelerator Engineering and Technology, Santa Fe, NM, March 21-23 (1983).

Cl a90, D. J. Clark, Lawrence Berkeley Laboratory Report No. LBL-28319 (1990).

Del 92, Th. Delbar, W. Galster, P. Leleux, E. Liénard, P. Lipnik, C. Michotte, J. Vervier, P. Duhamel, J. Vanhorenbeeck, P. Decrock, M. Huyse, P. Van Duppen, D. Baye, and P. Descouvemont, Nucl. Phys. A 542 (1992) 263-277.

Ehr51, J. B. Ehrman, Phys. Rev. 81 (1951) 412.

El f97, M. Elfman, P. Kristiansson, K. Malmqvist, J. Pallon, A. Sjoeland, R. Utui, and C. Yang, Nuclear Instruments & Methods in Physics Research Section B 130 (1997) 123-6.

Fei 90, B. Feinberg, J. G. Kalnins, and G. F. Krebs, Lawrence Berkeley Laboratory Report No. LBL-29243 (1990).

Fer83, R. A. Ferrieri and A. P. Wolf, Radiochim. Acta 34 (1983) 69.

Fes92, H. Feshbach, Theoretical Nuclear Physics: Nuclear Reactions, John Wiley and Sons, New York (1992).

Fi r96, R. B. Firestone, Table of Isotopes, Wiley-Interscience, New York, vol. II (1996).

Fox03, R. Fox, NSCL Data Acquisition Documentation, <http://docs.nscl.msu.edu>, 2003.

Fox96, R. Fox, A. Vander Molen, IEEE Transactions on Nuclear Science, 43(1) (1996) 55-60.

Gal 00, A. Galindo-Uribarri, J. Gomez del Campo, J. R. Beene, C. J. Gross, J. F. Liang, S. D. Paul, D. Shapira, D. W. Stracener, R. L. Varner, E. Chavez, A. Huerta, M. E. Ortiz, E. Padilla, and S. Pascual, Nucl. Instrum. Methods Phys. Res. B 172 (2000) 647-654.

Gal 01, A. Galindo-Uribarri, J. Gomez del Campo, J. R. Beene, C. J. Gross, M. L. Halbert, J. F. Liang, S. D. Paul, D. Shapira, D. W. Stracena, R. L. Varner, E. Chavez, and M. E. Ortiz, Nuclear Physics A 682

(2001) 363-368.

Gav80, A. Gavron, Phys. Rev. C 21 (1980) 230.

Gee77, D. F. Geesaman, R. L. McGrath, P. M. S. Lesser, P. P. Urone, and B. VerWest, Phys. Rev. C 15 (1977) 1835-1838.

Gi o02, J. Giovinazzo, B. Blank, M. Chartier, S. Czajkowski, A. Fleury, M. J. Lopez Jimenez, M. S. Pravikoff, J.-C. Thomas, F. de Oliveira Santos, M. Lewitowicz, V. Maslov, M. Stanoiu, R. Grzywacz, M. Pfützner, C. Borcea, and B. A. Brown, Phys. Rev. Lett. 89 (2002) 102501.

Gol 04, V. Z. Goldberg, G. G. Chubarian, G. Tabacaru, L. Trache, R. E. Tribble, A. Aprahamian, G. V. Rogachev, B. B. Skorodumov, and X. D. Tang, Phys. Rev. C 69 (2004) 031302.

Gol 60, V. I. Goldansky, Nucl. Phys. 19 (1960) 482.

Góm01, J. Gómez del Campo, A. Galindo-Uribarri, J. R. Beene, C. J. Gross, J. F. Liang, M. L. Halbert, D. W. Stracener, D. Shapira, R. L. Varner, E. Chavez-Lomeli, and M. E. Ortiz, Phys. Rev. Lett. 86 (2001) 43-46.

Gou75, F. S. Goulding and B. G. Harvey, Ann. Rev. Nucl. Sci. 25 (1975) 167.

Gre97, S. Grévy, O. Sorlin, and N. Vinh Mau, Phys. Rev. C 56 (1997) 2885.

Gri 01, L. V. Grigorenko, R. C. Johnson, I. G. Mukha, I. J. Thompson, and M. V. Zhukov, Phys. Rev. C 64 (2001) 054002.

References

Gri 02, L. V. Grigorenko, R. C. Johnson, I. J. Thompson, and M. V. Zhukov, Phys. Rev. C 65 (2002) 044612.

Guo03, F. Guo, D. Lee, D. Leitner, D. Moltz, P. McMahan, J. O'Neil, J. Powell, K. Perajarvi, L. Phair, and J. Cerny, in Nuclear Science Division 2002 Annual Report, H. Matis, ed., Lawrence Berkeley National Laboratory Report LBNL-526437, Berkeley, CA, (2003).

Guo04, F. Q. Guo, J. D. Powell, D. W. Lee, D. Leitner, P. McMahan, D. Moltz, J. O'Neil, K. Peräjärvi, L. Phair, and J. Cerny, in Nuclear Science Division 2003 Annual Report, R. Clark and H. Matis, eds., Lawrence Berkeley National Laboratory Report LBNL-55057, Berkeley, CA, (2004).

Han01, P. G. Hansen, Nuclear Physics News 11(4) (2001) 31-33.

Hec71, H. H. Heckman, D. E. Greiner, P. J. Lindstrom, and F. S. Bieser, Science 174 (1971) 1130-1131.

Hec72, H. H. Heckman, D. E. Greiner, P. J. Lindstrom, and F. S. Bieser, Phys. Rev. Lett. 28 (1972) 926-929.

Hue98, A. Huerta Hernández, C. Solís Rosales, M. E. Ortiz, E. R. Chávez Lomelí, J. Gomez del Campo, and D. Shapira, Nuclear Instruments & Methods in Physics Research Section B 143 (1998) 569-574.

Jon03, B. Jonson, The Physics Case for EURISOL, in The EURISOL Report Appendix A, John Cornell, ed., GANIL, Caen cedex, France (2003).

References

Joo00, R. Joosten, J. Powell, F. Q. Guo, P. E. Haustein, R. M. Larimer, M. A. McMahan, E. B. Norman, J. P. O'Neil, M. W. Rowe, H. F. VanBrocklin, D. Wutte, X. J. Xu, and J. Cerny, *Phys. Rev. Lett.* 84 (2000) 5066-5069.

Kek78, G. J. KeKelis, M. S. Zisman, D. K. Scott, R. Jahn, D. J. Vieira, J. Cerny, and F. Ajzenberg-Selove, *Physical Review C* 17 (1978) 1929-1938.

Kel 62, E. L. Kelley, in *Sector Focused Cyclotrons*, K. Siegbahn, and F. T. Howard, eds., North Holland Publishing Co., Amsterdam, (1962) 63.

Ki t90, Sindano wa Kitwanga, P. Leleux, and P. Lipnik, *Phys. Rev. C* 42 (1990) 748–752.

Kno89, G. F. Knoll, *Radiation Detection and Measurement*, 2nd ed., John Wiley and Sons, New York (1989).

Kob88, T. Kobayashi and O. Yamakawa, *Phys. Rev. Lett.* 60 (1988) 2599-2602.

Kof51a, O. Kofoed-Hansen and P. Kristensen, *Phys. Rev.* 82 (1951) 96.

Kof51b, O. Kofoed-Hansen and K. O. Nielsen, *Phys. Rev.* 82 (1951) 96–97.

Kof51c, O. Kofoed-Hansen and K. O. Nielsen, *Det Kongelige Danske Videnskabernes Selskab Matematisk-fysiske Meddelelser*, 26(7) (1951) 2-16.

Kof76, O. Kofoed Hansen, in *3rd International Conference on Nuclei Far from Stability*, CERN Yellow Report 76-13, Cargèse, France (1976)

65.

Kra88a, K. S. Krane, *Introductory Nuclear Physics*, John Wiley & Sons, New York (1988) 5.

Kra88b, K. S. Krane, *Introductory Nuclear Physics*, John Wiley & Sons, New York (1988) 378-443.

Kra88c, K. S. Krane, *Introductory Nuclear Physics*, John Wiley and Sons, New York (1987) 117.

Kre87, G. F. Krebs, J. R. Alonso, and J. Kalnins, Lawrence Berkeley Laboratory Report No. LBL-22143; C87/03/16 (1987).

Kre91, G. F. Krebs, J. R. Alonso, and B. Feinberg, Lawrence Berkeley Laboratory Report No. LBL-31417 (1991).

Kro00, K. A. Krohn, J. M. Link and W. G. Weitkamp, *Radiochim. Acta* 88 (2000) 193-199.

Kry95, R. A. Kryger, A. Azhari, M. Hellström, J. H. Kelley, T. Kubo, R. Pfaff, E. Ramakrishnan, B. M. Sherrill, M. Thoennesen, S. Yokoyama, R. J. Charity, J. Dempsey, A. Kirov, N. Robertson, D. G. Sarantites, L. G. Sobotka, and J. A. Winger, *Phys. Rev. Lett.* 74 (1995) 860-863.

Lan58, A. M. Lane and R. G. Thomas, *Rev. Mod. Phys.* 30 (1958) 257.

Lau51a, R. A. Laubenstein, M. J. W. Laubenstein, L. J. Koester, and R. C. Mobley, *Physical Review* 84 (1951) 12-18.

Lau51b, R. A. Laubenstein and M. J. W. Laubenstein, *Phys Rev* 84 (1951) 18.

Lei 03, D. Leitner, S. R. Abbott, R. D. Dwinell, M. Leitner, C. Taylor, C. M. Lyneis, in *Proceedings of the 2003 Particle Accelerator Conference*,

References

Piscataway, NJ, 2003, IEEE (Cat. No.03CH37423). IEEE. Part Vol.1, (2003) 86-88.

Lep03, A. Lépine-Szily, J. M. Oliveira, D. Galante, G. Amadio, V. Vanin, R. Lichtenthäler, V. Guimarães, G. F. Lima, H. G. Bohlen, A. N. Ostrowski, A. Di Pietro, A. M. Laird, L. Maunoury, F. de Oliveira Santos, P. Roussel-Chomaz, H. Savajols, W. Trinder, A. C. C. Villarid, and A. de Vismes, Nucl. Phys. A 722 (2003) 512-517.

Lun99, M. Lunardon, C. Merigliano, G. Viesti, D. Fabris, G. Nebbia, M. Cinausero, G. de Angelis, E. Farnea, E. Fioretto, G. Prete, A. Brondi, G. La Rana, R. Moro, A. Principe, E. Vardaci, N. Gelli, F. Lucarelli, P. Pavan, D. R. Napoli, and G. Vedovato, Nucl. Phys. A652 (1999) 3-16.

Lyn95, C. M. Lyneis et al., Proceedings of the 14th Conference on Cyclotrons and their Applications, Cape Town, South Africa, October 8–13, 1995, pp.173–176

Lyn98, C. M. Lyneis, in Nuclear Science Division 1997 Annual Report, R. B. Firestone, ed., Lawrence Berkeley National Laboratory Report LBNL 39764/UC-413, Berkeley, CA, 1998, p. 43.

Mah03, K. Mahata, S. Kailas, A. Shrivastava, A. Chatterjee, A. Navin, P. Singh, S. Santra, and B. S. Tomar, Nuclear Physics A 720 (2003) 209–221.

Mar00, K. Markenroth, L. Axelsson, S. Baxter, M. J. G. Borge, C. Donzaud,

References

S. Fayans, H. O. U. Fynbo, V. Z. Goldberg, S. Grévy, D. Guillemaud-Mueller, B. Jonson, K.-M. Källman, S. Leenhardt, M. Lewitowicz, T. Lönnroth, P. Manngård, I. Martel, A. C. Mueller, I. Mukha, T. Nilsson, G. Nyman, N. A. Orr, K. Riisager, G. V. Rogachev, M.-G. Saint-Laurent, I. N. Serikov, N. B. Shul'gina, O. Sorlin, M. Steiner, O. Tengblad, M. Thoennessen, E. Tryggestad, W. H. Trzaska, F. Wenander, J. S. Winfield, and R. Wolski, Phys. Rev. C 62 (2000) 034308.

Mar01, K. Markenroth, Ph.D. Thesis, Chalmers University of Technology and Göteborg University, Göteborg, Sweden, 2001.

Mar68, J. B. Marion and F. C. Young, Nuclear reaction analysis (graphs and tables), North-Holland Publishing Company, Amsterdam (1968).

Mol 97, D. M. Moltz, P. E. Haustein, R. Joosten, R.-M. Larimer, C. Lyneis, E. B. Norman, J. O'Neil, J. Powell, M. W. Rowe, H. VanBrocklin, D. Xie and J. Cerny, in Nuclear Science Division 1997 Annual Report, R. B. Firestone, ed., Lawrence Berkeley National Laboratory Report LBNL 39764/UC-413, Berkeley, CA, 1998.

Mor04, S. Moretto, D. Fabris, M. Lunardon, S. Pesente, V. Rizzi, G. Viesti, M. Barbui, M. Cinausero, E. Fioretto, G. Prete, A. Brondi, E. Vardaci, F. Lucarelli, A. Azhari, X. D. Tang, K. Hagel, Y. Ma, A. Makeev, M. Murray, J. B. Natowitz, L. Qin, P. Smith, L. Trache, R. E. Tribble, R. Wada, and J. Wang, Physical Review C 69 (2004)

044604.

Mye90, W. D. Myers, M. Nitschke, and E. B. Norman, eds., Proceedings of the First International Conference on Radioactive Nuclear Beams, Berkeley, California, 1989, World Scientific, Singapore (1990).

Nav00, A. Navin, D. W. Anthony, T. Aumann, T. Baumann, D. Bazin, Y. Blumenfeld, B. A. Brown, T. Glasmacher, P. G. Hansen, R. W. Ibbotson, P. A. Lofy, V. Maddalena, K. Miller, T. Nakamura, B. V. Pitychenko, B. M. Sherrill, E. Spears, M. Steiner, J. A. Tostevin, J. Yurkon, and A. Wagner, Phys. Rev. Lett. 85 (2000) 266–269.

Nel 85, R. O. Nelson and E. G. Bilpuch, Nuclear Instruments and Methods in Physics Research A 236 (1985) 128-141.

Ni t84, J. M. Nitschke, Proceedings of The Workshop on Prospects for Research with Radioactive Beams from Heavy Ion Accelerators, Washington, D.C., 1984, Lawrence Berkeley Laboratory Report No. LBL-18187; CONF-8404154 (1984).

Ni t88, J. M. Nitschke, Lawrence Berkeley Laboratory Report No. LBL-24982 (1988).

Ni t89, J. M. Nitschke, Lawrence Berkeley Laboratory Report No. LBL-28470 (1989).

Ni t90a, J. M. Nitschke, Lawrence Berkeley Laboratory Report No. LBL-28924 (1990).

Ni t90b, J. M. Nitschke, Lawrence Berkeley Laboratory Report No. LBL-

29256 (1990).

Ni t92, J. M. Nitschke, Accelerated radioactive nuclear beams: existing and planned facilities, Lawrence Berkeley Laboratory Report No. LBL-33072 (1992).

Ni t93, J. M. Nitschke, Future prospects for radioactive nuclear beams in North America, Lawrence Berkeley Laboratory Report No. LBL-34239 (1993).

Ni t94, J. M. Nitschke, Radiation problems encountered in the design of a radioactive nuclear beam facility, Lawrence Berkeley Laboratory Report No. LBL-35459 (1994).

Nol 02, J. A. Nolen, The European Physical Journal A- Hadrons and Nuclei 13 (2002) 255-261.

Oga99, K. Ogawa, H. Nakada, S. Hino, and R. Motegi, Phys. Lett. B 464 (1999) 157-163.

Ol n58, J. W. Olness, J. Vorona, and H. W. Lewis, Phys. Rev. 112 (1958) 475-480.

Oza00, A. Ozawa, T. Kobayashi, T. Suzuki, K. Yoshida, and I. Tanihata, Phys. Rev. Lett. 84 (2000) 5493–5495.

Par91, D. J. Parker, P. Vergani, E. Gadioli, J. J. Hogan, F. Vettore, E. Gadioli–Erba, E. Fabrici, and M. Galmarini, Phys. Rev. C 44 (1991) 1528-1540.

Pea00, G. F. Peaslee, P. A. DeYoung, D. P. Valente, T. S. Fan, R. Joosten,

References

M. A. McMahan, L. Phair, J. Powell, M. Rowe, G. J. Wozniak, D. Wutte, and J. Cerny, Excitation Functions of Fission Cross Sections for $^{11}\text{C} + ^{197}\text{Au}$, ^{194}Pt , ^{196}Pt , and ^{198}Pt , 1999 Annual Report, Nuclear Science Division, Lawrence Berkeley National Laboratory Report No. LBNL-45341, 2000

Pet03, W. A. Peters, T. Baumann, D. Bazin, B. A. Brown, R. R. C. Clement, N. Frank, P. Heckman, B. A. Luther, F. Nunes, J. Seitz, A. Stolz, M. Thoennessen, and E. Tryggestad, Phys. Rev. C 68 (2003) 034607.

Pfö02, M. Pfützner, E. Badura, C. Bingham, B. Blank, M. Chartier, H. Geissel, J. Giovinazzo, L.V. Grigorenko, R. Grzywacz, M. Hellström, Z. Janas, J. Kurcewicz, A.S. Lalleman, C. Mazzocchi, I. Mukha, G. Münzenberg, C. Plettner, E. Roeckl, K.P. Rykaczewski, K. Schmidt A7, R.S. Simon, M. Stanoiu, and J.-C. Thomas, Eur. Phys. J. 4 (2002) 279-285.

Pi e91, R. B. Piercey, Transactions of the American Nuclear Society 64 (1991) 218-219.

Pow00, J. Powell, R. Joosten, C. A. Donahue, R. F. Fairchild, J. Fujisawa, F. Q. Guo, P. E. Haustein, R.-M. Larimer, C. M. Lyneis, M. A. McMahan, D. M. Moltz, E. B. Norman, J. P. O'Neil, M. A. Ostas, M. W. Rowe, H. F. VanBrocklin, D. Wutte, Z. Q. Xie, X. J. Xu, J. Cerny, Nucl. Instrum. Methods Phys. Res. A 455 (2000) 452-459.

Pow03, J. Powell, J. P. O'Neil, J. Cerny, Nucl. Instrum. Methods Phys. Res.

B 204 (2003) 440–443.

Pow98, J. Powell, F. Q. Guo, P. E. Haustein, R. Joosten, R.-M. Larimer, C. Lyneis, D. M. Moltz, E. B. Norman, J. P. O'Neil, M. W. Rowe, H. F. VanBrocklin, Z. Q. Xie, X. J. Xu, and J. Cerny, in *Exotic Nuclei and Atomic Masses (ENAM 98)*, B. M. Sherrill, D. J. Morrissey, and C. N. Davids, eds, AIP Press, New York (1998); AIP Conference Proceedings 455(1)(1998) 999-1002.

Rat91, W. Rathbun, Lawrence Berkeley National Laboratory Report No. LBL-29734/UC-405, 1991 (unpublished).

Rei 81, W. Reisdorf, *Z. Phys. A* 300 (1981) 227-238.

Rol 88, C. E. Rolfs and W. S. Rodney, *Cauldrons in the Cosmos*, University of Chicago Press, Chicago (1988) 289-310.

Row97, M. W. Rowe, D. M. Moltz, J. C. Batchelder, T. J. Ognibene, R. J. Tighe and J. Cerny, *Nucl. Instrum. Methods Phys. Res. A* 397 (1997) 292.

Row98, Mike Rowe, Ph.D. Thesis, University of California, Berkeley (1998).

Sat83, G. R. Satchler, *Direct Nuclear Reactions*, Oxford University Press, New York (1983).

Saw91, J. A. Sawicki, K. E. Gregorich, L. Buchmann, G. J. Mathews, L. Orozco, G. D. Sprouse, M. Hass, and J. M. Wouters, *The Isospin Laboratory: Research Opportunities with Radioactive Nuclear Beams*, Los Alamos National Laboratory Report No: LALP 91-51

(1991).

Sch87a, M. R. Schmorak, Nucl. Data Sheets 50 (1987) 712.

Sch87b, M. R. Schmorak, Nucl. Data Sheets 51 (1987) 723.

Smo61, H. Smotrich, K. W. Jones, L. C. McDermott, and R. E. Benenson, Physical Review 122 (1961) 232-241.

Spa04, Sparrow Corporation, <http://www.sparrowcorp.com/kmax.html>, (2004).

Sti 74, J. D. Stickler and K. J. Hofstetter, Phys. Rev. C 9 (1974) 1064.

Tan85a, I. Tanihata, H. Hamagaki, O. Hashimoto, S. Nagamiya, Y. Shida, N. Yoshikawa, O. Yamakawa, K. Sugimoto, T. Kobayashi, D. E. Greiner, N. Takahashi, and Y. Nojiri, Physics Letters B 160 (1985) 380-384.

Tan85b, I. Tanihata, H. Hamagaki, O. Hashimoto, Y. Shida, and N. Yoshikawa, Phys. Rev. Lett. 55 (1985) 2676–2679.

Tan88, I. Tanihata, T. Kobayashi, O. Yamakawa, S. Shimoura, K. Ekuni, K. Sugimoto, N. Takahashi, T. Shimoda, and H. Sato, Physics Letters B 206 (1988) 592-596.

Tho01, M. Thoennessen, RIKEN Review No. 39 (2001) 68-70.

Tho03, M. Thoennessen, Particle Unstable Light Nuclei, AIP Conf. Proc. 680 (2003) 293.

Tho52, R. G. Thomas, Phys. Rev. 88 (1952) 1109.

References

Tho62, T. D. Thomas, G. E. Gordon, R. M. Latimer, and G. T. Seaborg, Phys. Rev. 126 (1962) 1805.

Tso95, N. Tsoulfanidis, Measurement and Detection of Radiation, 2nd ed., Taylor and Francis Publishing, Washington, D. C. (1995).

Van00, S. C. Van Der Linde, W. P. A. Jansen, J. J. M. De Goeij, L. J. Van IJzendoorn, and F. Kapteijn, Applied Radiation and Isotopes 52(1) (2000) 77-85.

Van97, H. F. VanBrocklin and J. P. O'Neil, in Applications of Accelerators in Research and Industry, J. Duggan and I. L. Morgan, eds., AIP Press, New York (1997) 1329–1332.

Ver03, J. Vervier, A feasibility study for a European isotope-separation-on-line radioactive ion beam facility, in The EURISOL Report, J. Cornell, ed., GANIL, Caen cedex, France (2003).

Ver93, P. Vergani, E. Gadioli, E. Vaciago, E. Fabrici, E. Gadioli Erba, M. Galmarini, G. Ciavola, and C. Marchetta, Phys. Rev. C 48 (1993) 1815.

Wes69, M. L. West, C. M. Jones, J. K. Bair, and H. B. Willard, Phys. Rev. 179 (1969) 1047-1059.

Xi e00, Z. Q. Xie, D. Wutte, and C. M. Lyneis, Nuclear Instruments & Methods in Physics Research Section B 168(1) (2000) 117-124.

Xi e91, Z. Xie, C. M. Lyneis, R. S. Lam, and S. A. Lundgren, Rev. Sci. Instrum. 62 (1991) 775.

References

Xi e97, Z. Q. Xie and C. M. Lyneis, in Proceedings of the 13th International Workshop on ECR Ion Sources, College Station, Texas, D. P. May and J. E. Ramirez, eds. (1997)16.

Xi e98, Z. Q. Xie., Rev. Sci. Instr. 69 (1998) 625.

Xi e99, Z. Q. Xie, J. Cerny, F. Q. Guo, R. Joosten, R. M. Larimer, C. M. Lyneis, P. McMahan, E. B. Norman, J. P. O'Neil, J. Powell, M. W. Rowe, H. F. VanBrocklin, D. Wutte, X. J. Xu, and P. Haustein, in Heavy Ion Accelerator Technology, K. W. Shepard, ed., AIP Press, New York, 1999; AIP Conference Proceedings 473(1) (1999) 312-320.

Zi e03a, J. F. Ziegler, The Stopping and Range of Ions in Matter (SRIM-2003), <http://www.srim.org>, (2003).

Zi e03b, J. F. Ziegler, J. P. Biersack, and U. Littmark, The Stopping and Range of Ions in Solids, Pergamon Press, New York, (2003).